

Incorporation of Guest-Molecules into Zeolite Mordenite

Inauguraldissertation
der Philosophisch-naturwissenschaftlichen Fakultät
der Universität Bern

vorgelegt von

Petra Simoncic

von Luzern

Leiter der Arbeit

Prof. Dr. Thomas Armbruster

Laboratorium für chemische und mineralogische Kristallographie

Incorporation of Guest-Molecules into Zeolite Mordenite

Inauguraldissertation
der Philosophisch-naturwissenschaftlichen Fakultät
der Universität Bern

vorgelegt von

Petra Simoncic

von Luzern

Leiter der Arbeit
Prof. Dr. Thomas Armbruster
Laboratorium für chemische und mineralogische Kristallographie

Von der Philosophisch-naturwissenschaftlichen Fakultät angenommen.

Bern, 11. November 2004

Der Dekan
Prof. Dr. P. Messerli

Contents

Abstract	9
Zusammenfassung	11
1 Introduction	13
1.1 Motivation	13
1.2 Structures of zeolites	14
1.2.1 Principles	14
1.2.2 Zeolite mordenite	17
1.3 Zeolite-based guest-host systems	19
1.3.1 Intrazeolitic semiconductors	21
1.3.2 Artificial antenna systems	21
1.4 Outline	24
Bibliography	27
2 Synthesis of 'large' mordenite crystals	29
2.1 Principles of zeolite synthesis	29
2.2 Synthetic mordenite	30
2.3 Synthesis experiments	32
Bibliography	39
3 Defect Structure of the Zeolite Mordenite	41
3.1 Introduction	42
3.1.1 Structure of zeolite mordenite	42
3.1.2 Pseudosymmetry	45

3.1.3	Framework defects and diffuse scattering	45
3.2	Experimental	47
3.2.1	Studied samples	47
3.2.2	X-ray data collection	48
3.2.3	Structure refinement	49
3.2.4	Diffuse scattering	50
3.3	Results	52
3.3.1	Diffuse scattering	52
3.3.2	Bragg reflections	54
3.4	Discussion	54
3.4.1	Si, Al arrangement	54
3.4.2	Extraframework cations	57
3.4.3	Limitations of Bragg model	58
3.4.4	Defects and crystallographic faulting	59
3.4.5	Structural model for the interface of the defect layer	61
3.4.6	Diffuse scattering	61
3.4.7	Open questions	64
3.5	Crystallographic data	65
	Bibliography	73
4	Se Incorporated into Zeolite Mordenite-Na	77
4.1	Introduction	78
4.2	Experimental	81
4.2.1	Sample	81
4.2.2	Selenium incorporation	82
4.2.3	X-ray data collection	83
4.3	Results	85
4.3.1	Structure refinement	85
4.3.2	Se incorporation	86
4.3.3	Se atoms	87
4.4	Discussion	90
4.4.1	H ₂ O in Se-loaded mordenite-Na	90
4.4.2	The mordenite framework	90

4.4.3	Arrangement of Se atoms in mordenite	92
4.5	Crystallographic data	97
	Bibliography	109
5	Thionin Blue in Zeolite Mordenite	113
5.1	Introduction	114
5.2	Experimental	118
5.2.1	Crystal synthesis	118
5.2.2	Dye incorporation	118
5.2.3	X-ray data collection	119
5.3	Results	121
5.3.1	Structure of thionin-mordenite-Na	121
5.3.2	Optical microscopy	124
5.4	Discussion	126
5.4.1	The mordenite framework	126
5.4.2	Extraframework atoms	127
5.4.3	Arrangement of thionin blue in the mordenite channels	128
5.5	Crystallographic data	133
	Bibliography	141
6	Methylene Blue in Zeolite Mordenite-Na	145
6.1	Introduction	146
6.2	Experimental	148
6.3	Results and Discussion	151
6.4	Crystallographic data	158
	Bibliography	165
	Publications	169
	Acknowledgements	171
	Lebenslauf	173

Abstract

Microporous materials such as zeolites are more and more applied for the design of advanced materials. With their channels and cavities of several angstroms in size, they allow a spatial arrangement and stabilization of individual atoms, clusters or molecules. One aspect of modern technology and new materials are one-dimensional systems and miniaturized electronic devices. Examples are luminescent dye molecules inserted in zeolite channels, building artificial antenna systems or semiconductor materials organized as quantum dots or chains in the zeolite cavities. These host-guest systems are usually well investigated in respect to short-range order of incorporated material or physio-chemical properties such as energy transfer mechanisms. But little is known about the exact positions, geometrical arrangement and disorder phenomena of encapsulated guest-compounds.

Zeolite mordenite was chosen for incorporation of luminescent dye molecules, and elemental selenium respectively. The large ellipsoidal 12-membered ring channels along [001] are tailor-made for the encapsulation of these materials because the anisotropic shape of the channel cross-section limits disorder of the enclosed guest-molecules. Self-synthesized large mordenite single-crystals of good quality and suitable morphology were used for incorporation of guest-species and diffraction experiments. Single-crystal X-ray diffraction experiments were performed with an conventional in-house X-ray source as well as using synchrotron radiation at the Swiss Norwegian Beamline at ESRF, France.

Even though the mordenite structure is considered as known, a new kind of defect-domain structure in the mordenite framework was found. Two single crystal X-ray diffraction experiments with synthetic mordenite-Na and a natural K-rich mordenite indicated that a part of the mordenite framework is repeated but shifted by a half-length of the c -translation ($c/2$). Detailed analysis of structural data and diffuse scattering showed that the mordenite structure consists of a defect structure of a domain A (97 %) and a $c/2$ shifted domain B (3 %), which seems to be a general feature independent of the Si/Al content.

Elemental selenium was encapsulated in mordenite-Na by gas phase. Structural refinement of Se-modified mordenite showed that several, low-populated, disordered Se chains with a length up to 10 Å and 7 Se atoms were located in the large 12-membered

ring channels. Because of electrostatic interaction with the framework and influence of extraframework occupants such as Na^+ and H_2O molecules, the chains show a highly variable geometrical arrangement. Se chains in mordenite differ clearly from the regular chain geometry as occurring in elemental, trigonal selenium.

Dye-loaded mordenite single-crystals were prepared using two different cationic, luminescent dyes. Thionin blue ($\text{C}_{12}\text{H}_{10}\text{N}_3\text{S}^+$) and methylene blue ($\text{C}_{16}\text{H}_{18}\text{N}_3\text{S}^+$) were incorporated into mordenite by ion-exchange in aqueous dye solution. Because the localization of the molecules within the mordenite channels by X-ray diffraction methods is complex, complementary methods such as polarization and fluorescence microscopy were applied analyzing the orientation of the molecule's transition dipole-moment. Results of microscopy studies and structure refinements illustrated that the dye molecules show distinct occupational disorder along the channel axis. The molecules prefer an inclined arrangement within the channel cross-section resulting in short $\text{CH}\dots\text{O}$ and $\text{NH}\dots\text{O}$ contacts to the framework. Due to geometrical reasons, the thionin blue molecule shows more rotational disorder than the larger methylene blue molecule.

Zusammenfassung

Mikroporöse Zeolithe finden immer häufiger Anwendung beim Design von neuartigen, hochentwickelten Materialien. Ihre typischen Kanäle und Käfige mit einem Durchmesser bis zu 13 Å erlauben eine räumliche Anordnung und Stabilisierung von einzelnen Atomen, Clustern oder Molekülen. Solche Wirt-Gast Systeme haben potentielle Anwendungen als elektronische Nanomaterialien: (1) Farbstoffe eingebaut in Zeolith-Kanäle bilden sogenannte optische Antennen-Systeme, (2) Halbleiter-Materialien angeordnet in den Zeolith-Käfigen haben die Funktion von Quantenpunkten oder -ketten. Die physikalisch-chemischen Eigenschaften und die Nahordnung der eingebauten Moleküle in diesen Wirt-Gast Systemen sind in der Regel gut untersucht. Jedoch ist wenig bekannt über die Lokalisierung und genaue geometrische Anordnung der Moleküle innerhalb der Zeolith-Kanäle.

Der Zeolith Mordenit wurde als Wirt für den Einbau von Farbstoff-Molekülen und elementarem Selen ausgewählt. Die 12'er-Ring Kanäle entlang der c -Achse eignen sich ausgezeichnet für den Einbau dieser Materialien: Die orthorhombische Gerüst-Symmetrie und die elliptische Form der Kanäle zwingt die Gast-Moleküle zu einer geordneteren Anordnung als in Zeolith-Gerüsten mit hexagonaler oder kubischer Symmetrie. Die für den Einbau der Gast-Moleküle und für die Röntgenstrukturanalyse der Wirt-Gast Systeme benötigten Einkristalle wurden hydrothermal hergestellt. Die Einkristall-Röntgendiffraktion wurde sowohl mit einer herkömmlichen Röntgenquelle als auch mit Synchrotron-Strahlung (Swiss Norwegian Beamline, ESRF, France) durchgeführt.

Obwohl die Struktur von Mordenit als bekannt gilt, wurde in dieser Arbeit eine neue Art von Domänen-Struktur im Mordenit-Gerüst entdeckt. Die Daten der Einkristall-Röntgendiffraktion eines synthetischen Mordenit-Kristall und eines natürlichen kaliumreichen Mordenits deuteten auf eine Wiederholung eines Teils des Gerüsts hin, der um eine halbe c -Translation ($c/2$) verschoben ist. Eine genauere Analyse der Strukturdaten und der diffusen Streuung ergab, dass sich das Mordenit-Gerüst aus 2 Domänen zusammensetzt: einer Domäne A (ca. 97 %) und einer um $c/2$ verschobenen Domäne B (ca. 3 %). Dieser Domänen-Anteil ist konstant und scheint unabhängig vom Aluminium-Gehalt im Mordenit-Gerüst zu sein.

Elementares Selen wurde als Gas-Phase in die Kanäle des Mordenit-Gerüsts einge-

baut. Die Strukturdaten von Se-modifiziertem Mordenit zeigten, dass sich mehrere niedrig besetzte und ungeordnete Ketten (max. Länge 10 Å, max 7 Se-Atome) in den grossen 12'er-Ring Kanälen befinden. Wegen einer elektrostatischen Wechselwirkung zwischen den Selen-Ketten und dem Zeolith-Gerüst, als auch wegen der Anwesenheit von anderen Kanalbesetzern, wie Na⁺-Kationen und H₂O Molekülen, zeigen die einzelnen Ketten eine sehr unterschiedliche räumliche Anordnung. Selen-Ketten in Mordenit-Kanälen unterscheiden sich deutlich von der regelmässigen Geometrie der Ketten im elementaren, trigonalen Selen.

Die lumineszierenden, kationischen Farbstoffmoleküle Thioninblau (C₁₂H₁₀N₃S⁺) und Methylenblau (C₁₆H₁₈N₃S⁺) wurden mittels Ionentausch in wässriger Lösung in Mordenit eingebaut. Zur Beschreibung der Farbstoffmoleküle in den Mordenite-Kanälen wurden zusätzlich zur Röntgenstrukturanalyse auch mikroskopische Methoden wie Polarisationsmikroskopie und Fluoreszenzmikroskopie angewandt. Die Ergebnisse der Mikroskopstudien und der Strukturdaten erforderten, dass die Moleküle geneigt in den 12'er-Ring Kanälen angeordnet sind und relativ kurze Abstände zu den Gerüstatomen bevorzugen. Die Positionen der Farbstoffmoleküle sind entlang der Kanalachse statistisch besetzt. Auf Grund der geringeren Grösse zeigt Thioninblau mehr einen höheren rotatorischen Freiheitsgrad als das grössere Methylenblau.

1 Introduction

1.1 Motivation

Zeolites with their open framework structures represent a fascinating mineral group for scientific purposes, as in geology, mineralogy, chemistry or material sciences, as well as in industrial and economical concerns. Zeolites show an impressive structural variability; over 170 different structure types are reported in the "Atlas of zeolite framework types" [1] (Fig. 1.1). In addition to around 70 known natural zeolites (see e.g. [2]), new types of synthetic zeolites are continuously designed for industrial use. Applications of zeolites are based on the ability of the open framework structures to selectively incorporate and exchange both charged and neutral species within the void spaces and interconnecting channels. Both natural and synthetic zeolites have a wide range of applications such as chemical sieves, catalysts, ion-exchanger, water-softener or fertilizer. Furthermore, they play an important role in the environmental protection, where zeolite-bearing rocks were selected for nuclear waste deposits (Yucca Mountains, Nevada, USA) [3]. Other applications are in the field of in waste water treatment

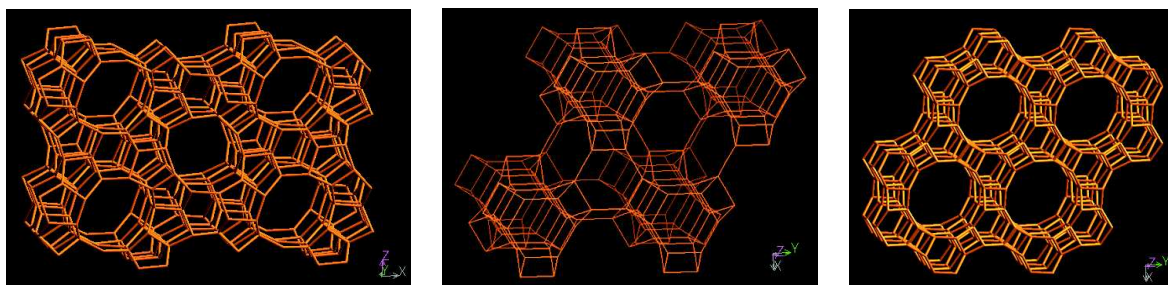


Figure 1.1: Framework structures of zeolite "ZSM-5" (left), "Erionite" (middle), and "AlPO-5" (right)

(removal of NH_4^+ and toxic metal cations) [2].

Besides these traditional applications, new uses of zeolites as advanced materials have arisen during the last two decades. The zeolite framework with its channels and cavities has a well defined internal structure, which provides the stabilization and organization of incorporated, more complex guest species such as organic molecules, metal clusters or semiconductor material [4]. The development of zeolite based guest-host systems enables a range of new and sophisticated applications, e.g. nano-scaled electronic devices, microlasers, molecular wires, or artificial antenna systems. Most studies in this field deal with the design of these guest-host systems and the investigation of their physio-chemical properties. On the other hand, the properties of such systems are directly linked to the structure of zeolites and their incorporated guests. A fundamental structural knowledge of the geometrical arrangement and ordering of the guest species within the zeolite channels, as well as the characterization of guest-framework interactions is of great importance for an improved understanding of zeolite-based guest-host systems. The natural occurring zeolite mordenite was chosen for the detailed structural study of a guest-host system by single-crystal X-ray diffraction. Mordenite possesses large, elliptic 12-membered ring channels, which are tailor-made for the incorporation of guest species such as semiconductor quantum chains or luminescent organic dye molecules.

1.2 Structures of zeolites

1.2.1 Principles

The structure of zeolites consists of three major characteristics:

1. a three-dimensional network of TO_4 tetrahedra, commonly SiO_4 and AlO_4 , but also PO_4 , BO_4 , GaO_4 etc.
2. an open structure with a low framework density
3. extraframework occupants such as cations and H_2O molecules

The zeolite framework is formed by linkage of corner-shared TO_4 tetrahedra, resulting in the characteristic channels and cavities up to 13 Å in diameter [5] (Fig. 1.2).

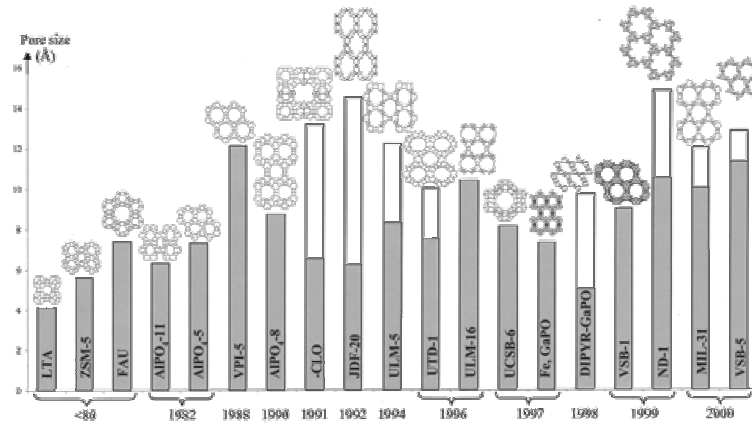
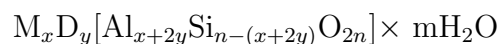


Figure 1.2: Scale of the dimensions of the pores of molecular sieves as a function of time. On the stick, the gray part corresponds to the useful size

As in other framework structures (feldspars, quartz), the ratio of tetrahedral cations to oxygens in the zeolite framework is 1:2. This means, that every TO_4 tetrahedron shares every oxygen with a neighbouring tetrahedron (Fig. 1.3). The substitution of Si^{4+} at the T position by a trivalent cation such as Al^{3+} results in a charge imbalance, causing a negatively charged framework. Since the charge of zeolite structure as a whole must be neutral, the charge of the framework is compensated by introducing extraframework metal cations such as Na^+ , K^+ , Ca^{2+} , which are situated in the zeolite channels and cavities. A general formula of zeolite can be written as



where M are monovalent cations and D are divalent cations. The part within the squared brackets represents the Si,Al framework, the part outside the squared brackets stand for the extraframework occupants. Depending on their charge, the extraframework cations are coordinated by H_2O molecules orienting their negative dipoles towards the cation. E.g. the divalent cations as Ca^{2+} have larger H_2O coordinaten spheres than monovalent cations of similar size (e.g Na^+). The extraframework occupants (cations, H_2O molecules) can be exchanged and expelled without destroying the framework, which is crucial for the applications of zeolites. The maximum possible Al content in the framework is defined by the Löwenstein rule [6]. According to the Löwenstein's rule, the Si:Al ratio must be ≥ 1 , which means that only Si-O-Si and Si-O-Al but no

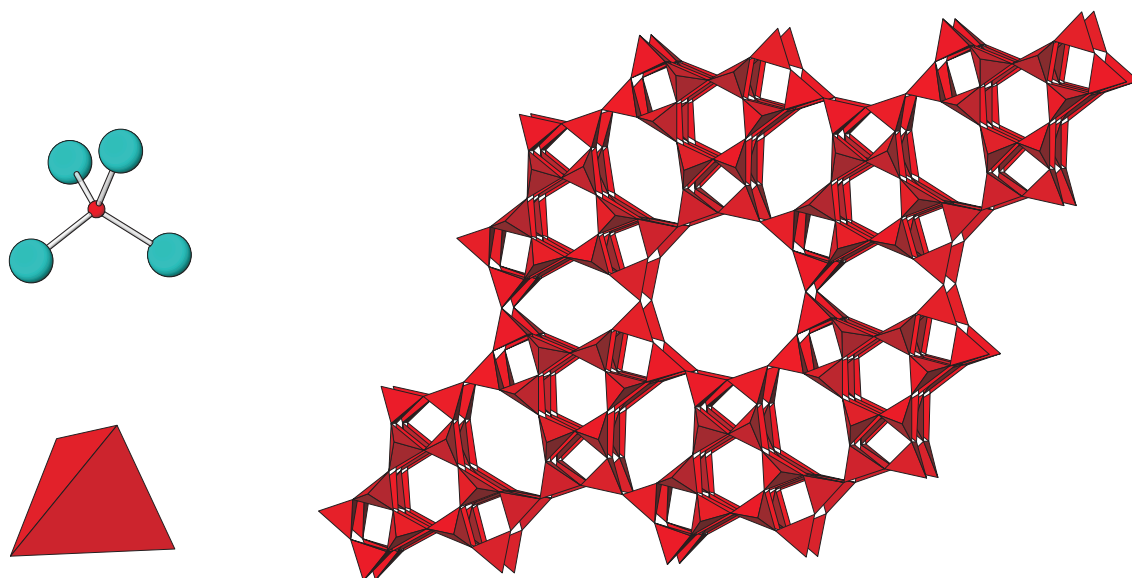


Figure 1.3: Top left: T-atom with four-coordinated oxygen atoms representing a tetrahedron. Bottom left: Polyhedral illustration of a tetrahedron. Right: Connected tetrahedra forming a zeolite framework (Linde type L)

Al-O-Al bridges are allowed. A Si:Al ratio of 1 results in a ordered Si/Al distribution, whereas Si:Al ratio of ≥ 1 may lead to an disordered Si/Al distribution.

There are three different systems for the classification of zeolites, which are all based on structural aspects as well as on similar properties and morphology.

The first classification is based on the framework topology allocating three letter codes to the different framework types, e.g. AFI, MOR, LTL, which are the abbreviations of the name of a "reference" structure [1]. The topology describes the tetrahedral connectivity of the framework in the highest possible symmetry. Framework and extraframework compositions and the observed symmetry are not considered, therefore different zeolites can be classified under one designation. E.g. heulandite $((\text{Na},\text{K})\text{Ca}_4[\text{Al}_9\text{Si}_{27}\text{O}_{72}]\times 24\text{H}_2\text{O})$ and clinoptilolite $((\text{Na},\text{K})_6[\text{Al}_6\text{Si}_{30}\text{O}_{72}]\times 24\text{H}_2\text{O})$ possess the same framework and have thus the same code HEU. The structure code is accompanied by the framework density that is the number of T atoms per 1000 \AA^3 . Zeolites have framework density lower than 21 T per 1000 \AA^3 [1].

Another classification method for zeolite is based on so-called "secondary building units" (SBU). The primary building unit of the zeolite framework is the tetrahedron,

Mordenite MOR

Crystal chemical data	$(\text{Na}_2, \text{K}_2, \text{Ca})_4 [\text{Al}_8 \text{Si}_{40} \text{O}_{96}] \times 28 \text{H}_2\text{O}$		
Framework topology	<i>Cmcm</i>	C-centered,	orthorhombic
Cell parameters	a: 18.11 Å α : 90° V: 2827 Å ³	b: 20.52 Å β : 90°	c: 7.52 Å γ : 90°
Framework density	17T/1000 Å ³		
Secondary building unit	5-1		
Channel system	12 - ring c	7.0 × 6.5 Å	
	8 - ring c	5.7 × 2.6 Å	
	8 - ring b	3.4 × 4.8 Å	

Table 1.1: Structural details of the mordenite framework [1]

the secondary building unit describes the geometrical arrangement of these tetrahedra, e.g. 4-, 5-, 6-, 8-membered rings, or 4-, 6-, 8-membered double-rings. These secondary building units, which contain up to 16 T-atoms, are derived from the assumption that the entire framework is made up of one type of SBU only [7].

The third classification, defined by Gottardi et Galli [8], is combination of the SBU system and morphological and historical aspects such as names and discovery of the mineral.

1.2.2 Zeolite mordenite

Based on the introduced principle structural features of zeolites, the structure of zeolite mordenite can be summarized in a "data sheet" (Table 1.1) [1].

A common feature of the mordenite framework is the 5-membered ring (secondary building unit: 5-1). In the MOR topology, units of four 5-rings are joined to one another via common edges to form chains. Mirror images of these chains are connected via

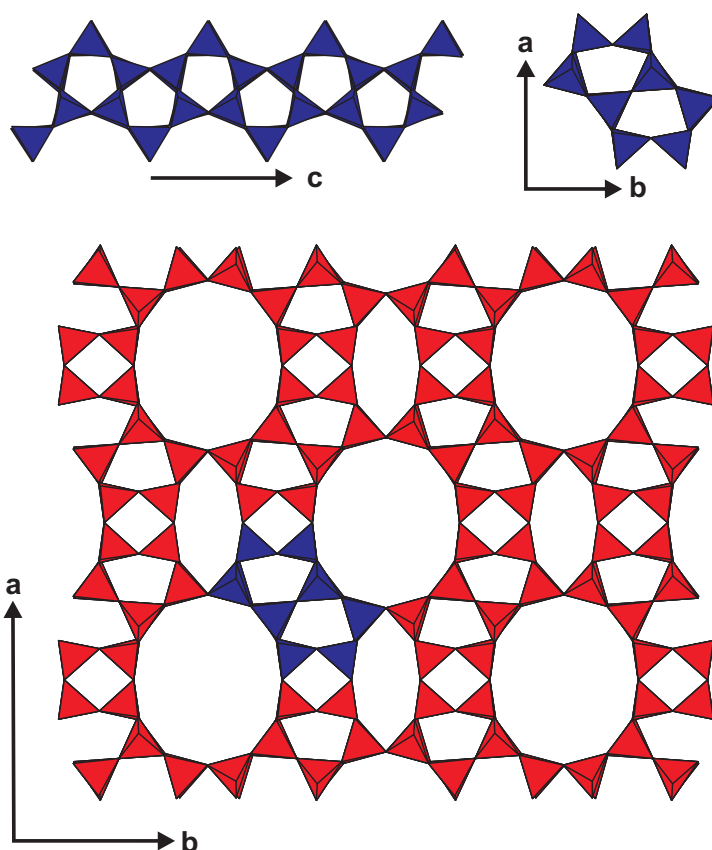


Figure 1.4: Top left: Chain of 5-membered tetrahedral rings along the c -axis. Top right: Chain of 5-membered T-rings viewed down the c -axis. Bottom: Mordenite framework constructed of chains of 5-membered rings forming the channel system. Large 12-membered ring channels down the c -axis, compressed 8-membered ring channels down the c -axis. Connection 8-membered ring channels down the b -axis (compare Fig. 3.2).

oxygen bridges to form puckered sheets. These sheets displaced by half a translation are connected to form oval 12-membered ring channels and 8-membered ring channels along the c -axis. These channels are interlinked by another set of 8-membered ring channels parallel to b , but these channels are displaced with respect to one another (compare Fig. 3.2). Therefore the mordenite channel system is essentially one-dimensional. Another, more comprehensible description of the mordenite framework is presented in Chapter 3.

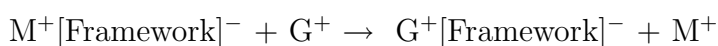
1.3 Zeolite-based guest-host systems

In the last few decades, zeolite-based solid state host-guest systems began to play an important role in the development of advanced materials, e.g. for a range of electronic applications [4]. Zeolites modified with chromophoric organic dye molecules found applications in photochemistry, as these dye-zeolite systems mimic the photosynthesis process in plants. From this basis, a continuous interaction between zeolite science and supramolecular chemistry has arisen.

The size of zeolite channels and cavities is often close to the dimensions of small organic molecules. As already mentioned above, exchange of extraframework metal cations and H₂O molecules is a common application of zeolites. But the well-defined internal structures of zeolites can also act as a host for the incorporation of more complex guest species as semiconductor materials, metal clusters or organic molecules. The incorporated guest-materials are spatially isolated within the channels, which prevents the formation of aggregates.

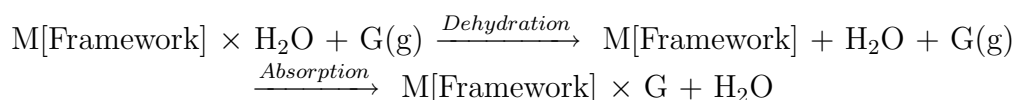
In general the incorporation is limited by the opening of the zeolite channels and the size and shape of the guest species. Different methods were established for the incorporation of charged (cationic) as well as neutral guest-species, for a review see [9].

1. Ion-exchange: The ion-exchange capability of zeolites can be used for the incorporation of cationic guest-species.



Both single- and double charged cationic molecules can be incorporated.

2. Adsorption in gas phase: Neutral guests can be encapsulated in gas phase, which requires the preceding dehydration (removal of H₂O molecules) of the zeolite:



Examples for ion-exchange and gas phase incorporation are given in Chapters 4, 5, and 6, respectively.

3. Crystallization inclusion: Guest compounds can be added to a zeolite synthesis batch. Depending on charge, solubility and stability (temperature, pH conditions), small amounts of the guest compound may be entrapped in the final synthesis product.
4. In situ synthesis of the guest within the host: The 4th possibility of guest-incorporation is the "ship-in-the-bottle" method, which means the synthesis of a guest compound within the zeolite channel. One example is the formation of an aromatic phthalocyanine ring from four molecules of dicyanobenzene within the 12-membered ring pores of zeolite Y. These ring molecules are too large to be removed from the zeolite and are entrapped in the zeolite Y supercage.

Zeolite-based guest-host systems find various applications, the following overview focusses on intrazeolitic semiconductors and artificial antenna systems.

- **Non-linear optical (NLO) materials:** Non-linear optical effects appear when the electric field of the electromagnetic radiation interacting with matter is very strong. These effects are observed in acentric zeolites modified with molecules such as p-nitroaniline or 2-methyl-p-nitroaniline. NLO materials are used for frequency multiplication in laser technology.
- **Chemical sensors:** Sensors are small devices, which convert any microchanges of temperature, pressure, concentration or other properties into detectable signals. Due to the size and shape selectivity of zeolites, different applications for chemical sensors such as moisture sensing, oxygen monitoring, carbon monoxide detection, or ethylene, ethane and propylene detection are reported.
- **Zeolite-polymer composites:** Polymers such as polythiazyl, polypyrrole or polyaniline encapsulated in unidimensional channels of zeolites represent so called molecular wires, isolated conduction or semiconducting chain structures. The adsorption of monomers such as acetylene into zeolite channels leads easily to polymerization. Such systems are anticipated to allow miniaturization of electronic devices.

1.3.1 Intrazeolitic semiconductors

A major focus in the design of advanced materials is the synthesis of extremely small semiconductor particles. The electronic properties of a bulk solid-state compound differ explicitly from the properties of molecules and clusters (~ 10 atoms) of the same material. So called quantum-size effects (e.g. widening of the band gap) occur, when the geometric dimensions of a particle are similar to the free wavelength of the electrons in the material. Semiconductor material incorporated into the cavities of zeolites can work as quasi-2D, 1D or 0D semiconductors. An example for a 2D semiconductor are artificially layered structures, so called semiconductor superlattices. The formation of modulated chemical composition layers allows the realization of band gap engineering, heterojunctions, or high electron mobility transistors.

Further reduction to 1D and 0D systems enhance quantum size effects: improved electron mobilities and resonant tunneling have been observed in quantum wires and dots arranged in zeolite channels. Although 1D and 0D quantum systems were also realized using liquid suspensions, glasses, or micelles, zeolites showed an advantage to the other matrices listed because they permit the ordered inclusion of particles with very small dimensions and a uniform size distribution. Quantum sized CdS, CdSe and PbS were encapsulated into zeolites such as zeolite A, X, or Y forming semiconductor quantum dot systems.

When elemental selenium is incorporated into zeolite channels, significant differences in the band gap and optical absorption spectra are observed. Interchain interactions are minimized and the Se chains within the one-dimensional channels of AIPO-5 and mordenite act as isolated chains. The band gaps for Se in AIPO-5 and mordenite are considerably larger than for bulk trigonal Se.

1.3.2 Artificial antenna systems

The photosynthesis process in plants represents a well-known natural antenna system. The best known form of photosynthesis is the one carried out by higher plants and algae, as well as by cyanobacteria and their relatives, which are responsible for a major part of photosynthesis in oceans. All these organisms convert CO_2 to organic material by reducing this gas to carbohydrates in a rather complex set of reactions. The photosynthetic reactions are traditionally divided into two stages - the "light reactions,"

which consist of electron and proton transfer reactions and the "dark reactions," which consist of the biosynthesis of carbohydrates from CO_2 .

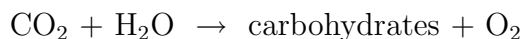
The light reactions convert energy into several forms. The first step is the conversion of a photon to an excited electronic state of an antenna pigment molecule located in the antenna system. The antenna system consists of hundreds of pigment molecules (mainly chlorophyll or bacteriochlorophyll and carotenoids) that are anchored to proteins within the photosynthetic membrane and serve a specialized protein complex known as a reaction center.

Light reaction:

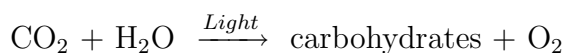
Light absorbed by chlorophyll molecules \rightarrow photons \rightarrow NADPH + ATP

In the reaction center, the enzymes NADPH and ATP are formed by the light reactions. These enzymes provide the energy for the dark reactions of photosynthesis, known as the Calvin cycle or the photosynthetic carbon reduction cycle, where CO_2 is converted to carbohydrates.

Dark reaction:



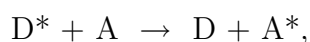
Total reaction:



Luminescent organic dyes intercalated in zeolite channels have the potential to mimic the process of natural photosynthesis. Various dye molecules have similar dimensions as the zeolite's channel opening and can be inserted by ion-exchange and gas-diffusion.

The research group of Calzaferri et al. [10–13] developed an artificial antenna system of a bi-directional type. They apply zeolite L as a host material and different dye molecules, mainly cationic oxonin, pyronin and neutral fluorenone, which are incorporated into the one-dimensional channel system of zeolite L. By the incorporation of the dye molecules into the zeolite channels, the chemical and photochemical stability is highly improved.

Analogue to chlorophyll in plants, the dye molecules are excited by incident light to a higher electronic state and transport the excitation energy through the zeolite channels. The energy transport is based on the Förster energy transfer mechanism [14]. The Förster mechanism describes the weak interaction between a donor and an acceptor molecule. The distance between a donor and acceptor molecule where the energy transfer occurs at a probability of 0.5 is defined as the Förster energy transfer radius R_0 . In a pyronin-oxonin system the radius R_0 is 60 Å.



where D is the donor molecule and A acceptor molecule, * marks the excited state. The best-established zeolitic antenna system designed by Calzaferri et al. consists of cationic pyronin working as a donor and placed in the middle part of the zeolite. Cationic oxonin works as an acceptor and is placed at the end of the channels. To improve the functionality, the zeolitic antenna systems were extended with closure and stopcock molecules.

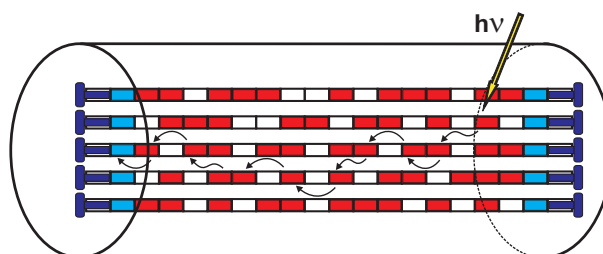


Figure 1.5: Dye-zeolite guest-host system (after Calzaferri et al. [10–13]) Rows represent the zeolite channel, each square is a unit cell. Red filled are dye molecules acting as a donor, light blue are acceptor dye molecules. Stopcock molecules placed at the end of the channels are dark blue.

In general, the inserted dye molecules can leave the zeolite channel the same way as they entered. To reach a better stability regarding wettability and chemical reactivity, it is desirable to block their way out. A Closure molecule has the function to seal the dye-filled channels (Fig. 1.5). Stopcock molecules are required for trapping the energy from the excited dye molecules in the channels and work as a connection to the "outside world". A stopcock molecule consists of a head, a spacer and a label.

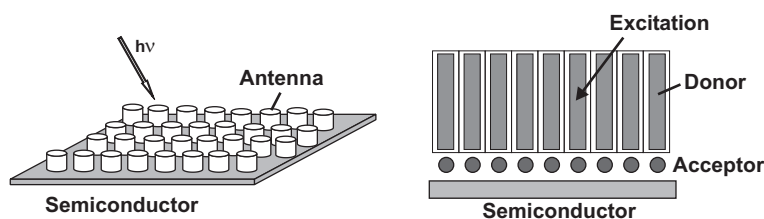


Figure 1.6: Sensitized solar cell based on dye-loaded zeolite systems (after Calzaferri et al. [10–13]). The antenna systems (cylinders) absorb light and transport their energy to the semiconductor surface.

Besides these antenna functionalities, dye-modified zeolites show strong fluorescence light emission, when the dye molecules are excited by a certain wavelength. The light emission can be used for demonstrating the migration and distribution of the dye molecules inside the zeolites.

The described dye-zeolite systems find potential applications as solar cells, nano-scaled lasers or LEDs. The use as a new type of solar cell is discussed in more detail later on. The dye-loaded, nanosized ($1\ \mu\text{m}$) zeolite crystals are arranged as a monolayer on a semiconductor, conducting glass or metal. In a dye-sensitized solar cell, the incoming light is absorbed within the volume of the zeolitic nanocrystals containing luminescent molecules for light harvesting. The excitation energy is transported via energy migration to the contact surface with the semiconductor. By energy transfer from an excited dye to the semiconductor, it creates an electron hole pair in the semiconductor (Fig. 1.6. For a detailed review of photochemistry and zeolites see [15, 16].

1.4 Outline

Chapter 2 presents the successful synthesis of large mordenite single crystals, which are subsequently chemically modified with guest-molecules. Large, high-quality zeolite single crystals are difficult to synthesis but required for single-crystal X-ray diffraction. A crystal size of at least $30\ \mu\text{m}$ on an edge are needed for successful X-ray data collection with synchrotron radiation.

Chapter 3 discusses the defect structure of the mordenite framework. Framework defects in mordenite were widely discussed in literature, but a detailed structural

characterization is lacking. Two single crystal X-ray experiments with the synthetic Na-mordenite (synchrotron radiation) and a natural K-rich mordenite (common X-ray source) showed that a part of the mordenite structure is repeated and shifted by $c/2$.

Chapter 4, 5 and 6 show the successful incorporation of guest-molecules such as elemental selenium, cationic dye molecules thionin and methylene blue into the channels of mordenite. These studies focus on the localization, order-disorder phenomena and guest-framework interactions in these guest-host systems combining single-crystal X-ray diffraction, microscopy methods and Raman spectroscopy.

Bibliography

- [1] C. Bärlocher, W.M. Meier, and D.H. Olson, *Atlas of Zeolite Framework Types*, Structure Commission of the International Zeolite Association, 2001.
- [2] D.L. Bish and D.W. Ming, *Natural zeolites: Occurrence, Properties, Applications*, Vol. 45 of *Reviews in Mineralogy and Geochemistry*, Mineralogical Society of America, 2001.
- [3] D.L. Bish, D.T. Vaniman, R.S. Rundberg, K. Wolfsberg, W.R. Daniels, and D.E. Broxton, “Natural sorptive barriers in Yucca Mountain, Nevada, for long-term isolation for high-level waste”, in *Radioact. Waste Manage., Proc. Int. Conf., Meeting Date 1983*. 1984, Vol. 3, p. 415–432, IAEA.
- [4] G.A. Ozin, A. Kupermann, and A. Stein, “Advanced zeolite material science”, *Adv. Mater*, Vol. 101, No. 3, p. 373–390, 1989.
- [5] G. Férey, “Microporous solids: From organically templated inorganic skeletons to hybrid frameworks...ecumenism in chemistry”, *Chem. Mater*, Vol. 13, No. 10, p. 3084–3098, 2001.
- [6] W. Loewenstein, “The distribution of aluminium in the tetrahedra of silicates and aluminates”, *Am. Mineral*, Vol. 39, p. 92–96, 1954.
- [7] D.W. Breck, *Zeolite Molecular Sieves*, p. 771, John Wiley and Sons, 1974.
- [8] A. Gottardi and E. Galli, *Natural Zeolites*, p. 223, Springer, Berlin, 1985.
- [9] D.E. De Vos and P.A. Jacobs, *Introduction to Zeolite Science and Practice*, Vol. 137 of *Studies in Surface Science and Catalysis*, Chapter Zeolite-based Supramolecular Assemblies, p. 957–985, Elsevier, 2001.

- [10] G. Calzaferri, D. Brühwiler, D. Megelski, M. Pfenniger, M. Pauchard, B. Hennessy, H. Maas, A. Devaux, and U. Graf, “Playing with dye molecules at the inner and outer surface of zeolite L”, *Solid State Sci.*, Vol. 2, p. 421–447, 2000.
- [11] G. Calzaferri, “Organic-inorganic composites as photonic antenna”, *Chimia*, Vol. 55, p. 1009–1013, 2001.
- [12] G. Calzaferri, M. Pauchard, H. Maas, S. Huber, A. Khatyr, and T. Schaafsma, “Photonic antenna system for light harvesting, transport and trapping”, *J. Mater. Chem.*, Vol. 12, p. 1–13, 2002.
- [13] G. Calzaferri, S. Huber, H. Maas, and C. Minkowski, “Photon-harvesting host-guest antenna materials”, *Angew. Chem. Int. Ed.*, Vol. 42(32), p. 3732–3758, 2003.
- [14] Th. Förster, “Zwischenmolekulare Energiewanderung und Fluoreszenz”, *Ann. Phys.*, Vol. 6, No. 2, p. 55–75, 1948.
- [15] V. Ramamurthy and M.A. Garcia-Garibay, *Solid State Supramolecular Chemistry: Two- and Three-Dimensional Inorganic Networks*, Vol. 7 of *Comprehensive Supramolecular Chemistry*, Chapter Zeolites as Supramolecular Host for Photochemical Transformations, p. 693–719, Pergamon, 1998.
- [16] S. Hashimoto, “Zeolite photochemistry: impact of zeolites on photochemistry and feedback from photochemistry to zeolite science”, *J. Photochem. Photobiol C: Photochem Rev.*, Vol. 4, p. 19–49, 2003.

2 Synthesis of 'large' mordenite crystals

2.1 Principles of zeolite synthesis

Although zeolites are synthesized in large amounts for industrial use, zeolitic material is often only available as polycrystalline material (powder). In contrast, synthesis methods for 'large' zeolite single-crystal (at least $> 50 - 100 \mu\text{m}$ on a edge) are still rare, but these are necessary for single-crystal X-ray diffraction. The access to high-intensity synchrotron radiation enables the X-ray data collection also on smaller crystals ($> 20 \mu\text{m}$), but large high-quality zeolite single-crystals are still desirable.

Natural zeolites generally form by reaction of a mineralizing aqueous solution with solid aluminosilicates. The main formation parameters can be summarized as

1. The composition of the host rock and the aqueous solution; $\text{pH} \sim 10$
2. Time; Thousands of years
3. Temperature; $< 300 \text{ }^\circ\text{C}$

These principles from nature can be used as a guide for the hydrothermal synthesis of zeolites. First successful zeolite synthesis was reported by Barrer [1] and Breck and Milton [2] in the late 1940's. Since then more than 150 different zeolite products without natural counterparts have been synthesized. Most synthesis methods of zeolites are based on the reactive crystallization or precipitation from an aqueous mixture of reagents at $6 < \text{pH} < 14$ and temperatures between $100 - 200 \text{ }^\circ\text{C}$. Verified synthesis procedures of 71 different zeolites are summarized in [3].

Synthesis parameter can be divided in two groups: (1) chemical sources, and (2) physical parameters as temperature, heating time, pressure, agitation, and the reaction

vessel. In general, following chemical sources are needed for the zeolite synthesis:

Sources	Function
SiO ₂	Primary building units of the framework
AlO ₂ ⁻	Origin of framework charge
OH ⁻	Mineralizer
Alkali cation, template	Counterion of AlO ₂ ⁻ , guest molecule
Water	Solvent, guest molecule

Hydrothermal zeolite crystallization from solution occurs mainly in two steps: (1) the nucleation of one or several phases, and (2) the growth of the nuclei to larger sizes by incorporation of material from the solution.

The critical parameter for obtaining 'large' zeolite crystals is the reduction or suppression of the nucleation. The successful control of the size of large zeolite crystals using this approach requires the ability to control the formation of zeolite nuclei. Successful reduction and control of nucleation was achieved by low supersaturation, by adding an organic complexing-agent, or by the use and preparation of different SiO₂ sources, as discussed below for the example of 'large' mordenite single-crystals. It is worth mentioning that large zeolite crystals were also synthesized in low-gravity conditions [4].

2.2 Synthetic mordenite

Mordenite, which was chosen for this structural study on guest-host systems, is a natural occurring zeolite and forms crystals that have sufficient quality and size for single-crystal X-ray diffraction experiments.

Natural mordenite forms either from hydrothermal alteration, or from lower temperature transformation of volcanic glasses, and shows a distinct needle-shaped, fibrous habit (Fig. 2.1). Actually, natural mordenite is regarded as an asbestiformous material causing lung diseases [5, 6]. Because of its fibrous morphology, natural mordenite single-crystals are not suitable for the incorporation of guest molecules. The large 12-membered ring channels designated for the incorporation of guest species run along the long crystal axis (compare Fig. 2.1). The (001) face, where the entries to the 12-

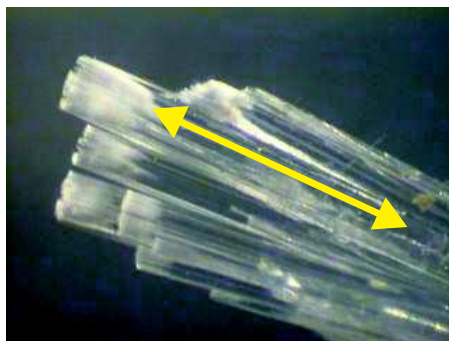


Figure 2.1: Natural mordenite single crystals with fibrous habit. The arrow indicates the direction of the 12-membered ring channels and the crystal's c -axis.

membered ring channels are situated, is very small and gives only access to a limited amount of channel openings. Furthermore, the fibrous habit makes the pathway for entering guests very long, which is kinetically unfavorable and would result in slow diffusion rates.

Therefore, it was the aim to synthesize large mordenite single-crystals with suitable quality for single-crystal X-ray diffraction and suitable morphology for the incorporation of guest-molecules. In particular, it is desirable to obtain a more dominant (001) face and thus easier access to the large 12-membered ring channels. Several methods for the hydrothermal synthesis of 'large' mordenite single-crystal are reported. These methods focused all on the control of nucleation and produced crystal sizes from 50 to 180 μm . In general, few nuclei in the synthesis mixture lead to larger crystals.

Mordenites are divided into two groups: (1) large port mordenites, which can absorb molecules $> 4.5 \text{ \AA}$, and (2) small port mordenites, which can absorb only molecules $< 4.5 \text{ \AA}$. It has been reported that large-port mordenites form between 75 and 260 $^{\circ}\text{C}$, whereas small-port mordenites are usually obtained under hydrothermal synthesis conditions between 275 and 300 $^{\circ}\text{C}$ [7]. For the incorporation it is essential that the mordenite crystals are present in their large-port form, which means synthesis conditions at moderate temperature. The phenomena of large- and small-port mordenite is in more detail discussed in "Chapter 3" of this study.

Sun et al. [8] proposed the synthesis of 'large' mordenite single-crystal in a clear homogenous solution by using two silica sources in the starting mixture, the addition of an appropriate amount of salt, and high alkalinity. They postulated that the use

of two silica sources, aerosil (fumed silica) and sodium silicate solution, lead to larger mordenite single crystals. Furthermore, a higher alkalinity and the addition of NaCl influences the nucleation time and crystallization rate. Largest crystals with dimensions of $185 \times 125 \mu\text{m}$ were obtained with a starting batch of $1 \text{ Al}_2\text{O}_3 : (60(\text{aerosil}) + 15(\text{sodium silicate solution})) \text{ SiO}_2 : 19 \text{ Na}_2\text{O} : 575 \text{ H}_2\text{O} : 4 (\text{NaCl})_2$ at $150 \text{ }^\circ\text{C}$ during 15 days.

Sano et al. [9] demonstrated the synthesis of 'large' mordenite single-crystals by adding aliphatic alcohol to the starting mixture. According to the authors, the addition of aliphatic alcohol causes a buffering effect: Additional 1-BuOH causes a slower release of silicon and aluminium species into the reaction medium, which is essential for a reduced nucleation and the synthesis of larger crystals. The synthesis batch of $7 \text{ SiO}_2 : 0.1 \text{ Al}_2\text{O}_3 : 4.9 \text{ NaOH} : 280 \text{ H}_2\text{O} : 10.5(1\text{BuOH})$ at $160 \text{ }^\circ\text{C}$ during 72 hours led to slightly needle-shaped crystals up to $40 \times 12 \mu\text{m}$.

Warzywoda et al. [10] synthesized 'large' mordenite single crystals up to $180 \mu\text{m}$. They used as a silica source different kind of porous silica gel, which was either untreated, heated or mechanically modified. Best synthesis results were obtained with porous silica gel pre-heated up to $900 \text{ }^\circ\text{C}$. The heating causes a reduction of the surface area of the silica gel, and as a result this reduces the reactivity within the synthesis batch and leads to a more controlled nucleation. Largest crystals up to $175 \mu\text{m}$ were synthesized using a silica gel with pore openings of 150 \AA preheated at $850 \text{ }^\circ\text{C}$ for 24 hours under air. The synthesis was carried out with a molar composition of $4.32 \text{ Na}_2\text{O} : \text{Al}_2\text{O}_3 : 19 \text{ SiO}_2 : 293.6 \text{ H}_2\text{O}$ during 4 days at $175 \text{ }^\circ\text{C}$. The crystals showed a rather uniform or slightly elongated morphology.

2.3 Synthesis experiments

Because of crystal size and suitable morphology, the method of Warzywoda et al. [10] was chosen for the synthesis of 'large' mordenite single-crystals used in this study. The synthesis procedure regarding the synthesis batch-composition, described by Warzywoda et al. was taken as a starting point for the synthesis experiments in the home lab. The synthesis method was modified by changing pH, temperature, synthesis duration, and the composition of the synthesis batch (additional compounds).

Synthesis experiments were carried out in two different vessels (Fig. 2.2):

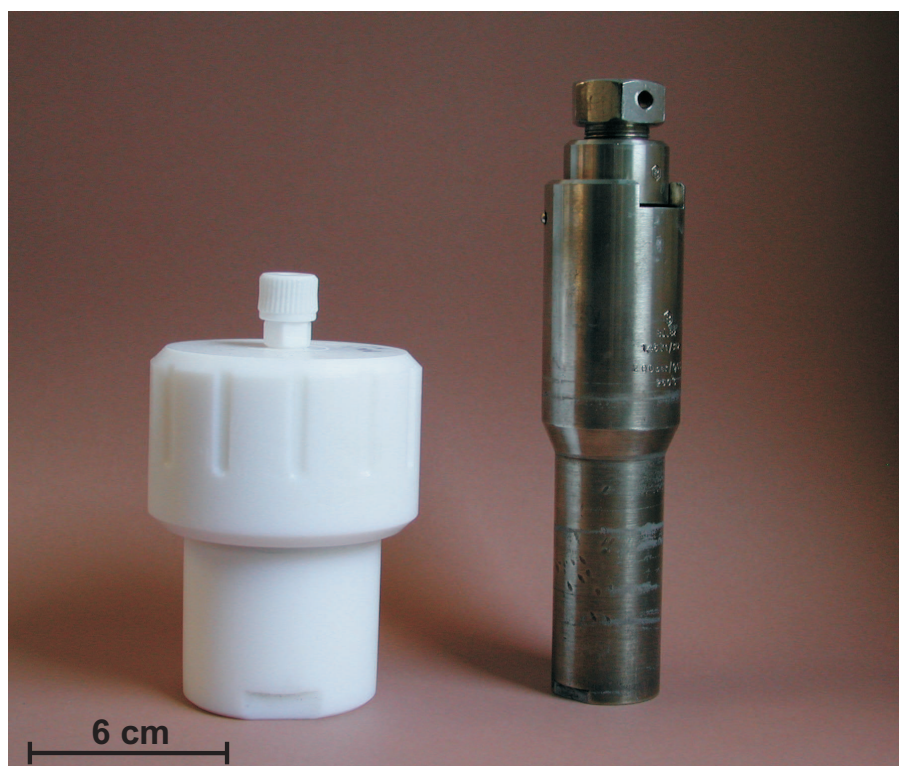


Figure 2.2: Left: Vessel A. Right: Vessel B

1. a teflon vessel with a diameter of 3 cm and a length 7.5 cm. This vessel was sealed by two plastic inlets; (A)
2. a teflon vessel with diameter of 2.2 cm and a length of 11 cm placed in a steel mantle, which was closed by a screwed sealing plug; (B)

Following materials were used for starting materials in all synthesis runs:

- Silica source: Silica gel; Grade 62, pore size 150 Å (Aldrich)
- Aluminium source: Na-Aluminate; NaAlO_2 , anhydrous, technical (Riedel-de Haen)
- NaOH (Hänseler)

In general, the required amount of water defined by the synthesis batch-composition was separated in two halves. NaOH was dissolved in one half, NaAlO_2 was dissolved

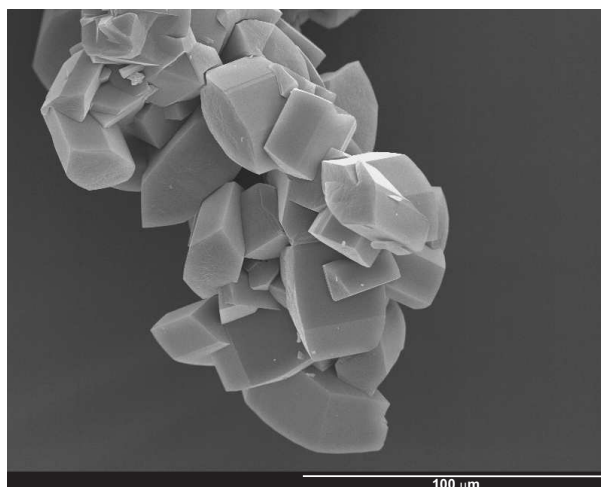


Figure 2.3: The original recipe resulted in small crystals, but of well defined morphology.

in the other half. The NaOH- and NaAlO₂ solutions were mixed together with the silica gel and stirred for 20 min. This procedure was identical for all synthesis runs. Different synthesis runs and their products will be presented. The synthesis procedure was modified according (1) the synthesis duration, (2) the changing of the original synthesis batch composition, (3) the addition of other chemical species to the synthesis batch.

1. **Original procedure:** The original synthesis procedure as reported by Warzywoda et al. led to mordenite single crystals up to 30 μm. The synthesis products were 100 % mordenite crystals. The pH of the original synthesis batch was determined to 13. The crystals were too small for successful X-ray diffraction and structure determination, but they showed an appropriate morphology and good crystal quality under the scanning electron microscope (SEM) (Fig. 2.3). Thus in the subsequent synthesis runs, the synthesis procedure was changed to reach larger crystals.
2. **Synthesis duration:** The change of the synthesis duration had different effects: the reduction of the synthesis duration resulted in small, twinned crystals and undissolved silica gel, which means that the synthesis reaction has not been yet completed (Fig. 2.4). On the other hand, the prolongation of the synthesis time

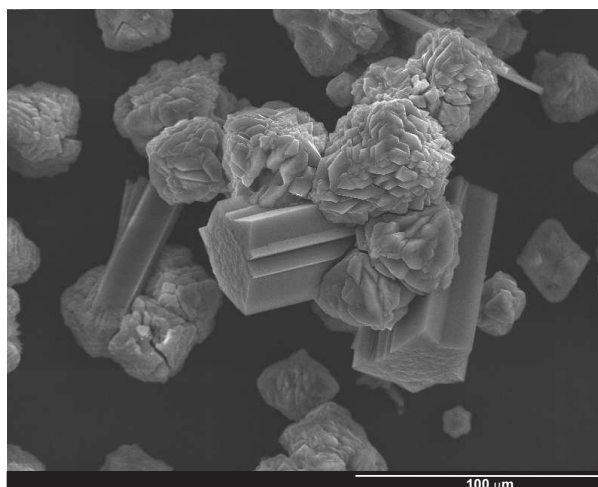


Figure 2.4: A reduction of the synthesis time led to unfinished synthesis products. The silica gel was not completely dissolved.

had no significant effect on the crystal size. Longer duration did not result in larger crystals.

- 3. Change of the synthesis batch:** The synthesis products using double amount of water, thus reducing the concentration of the other species, showed large crystals of more than $100 \mu\text{m}$ in maximum dimension. However, investigation of the crystals with the scanning electron microscope showed that the crystals were strongly twinned and not suitable for single-crystal X-ray diffraction (Fig. 2.5). The pH of this starting batch was only slightly lower (12.8) than in the original synthesis batch-composition.

The use of both ethanol and butanol in the synthesis batch led to long, needle-shaped and twinned crystals (Fig. 2.6). This corresponds to the needle-shaped mordenite single crystals synthesized by Sano et al. [9]. The addition of salts such as NaCl and CsCl inhibited crystal growth completely.

- 4. Final procedure:** The addition of a small amount of ethanol in combination with the original procedure and a longer synthesis duration (120 h than 96 h) resulted in mordenite crystals with sufficient size and suitable morphology for the incorporation of guest-molecules and the subsequent single-crystal X-ray diffraction. The crystals have a dominant (001) face providing access to a large number

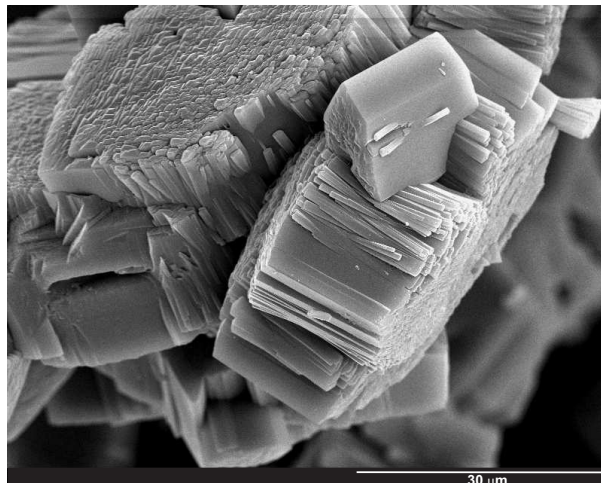


Figure 2.5: The use of the double amount of water (and therefore a slight reduction of the pH) showed macroscopic large crystals. Closer investigation with SEM showed that the crystals are strongly twinned and unusable for X-ray diffraction.

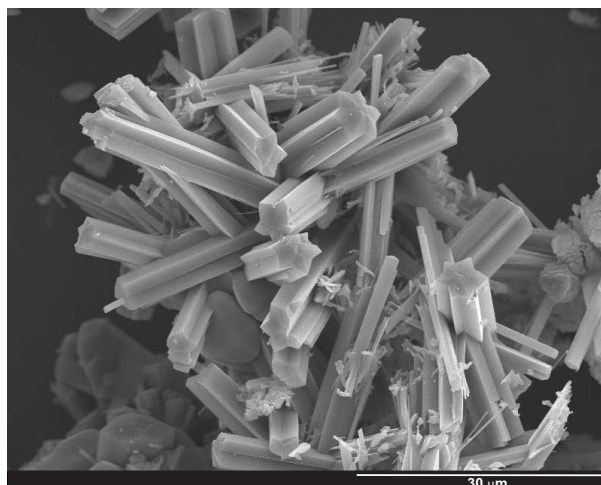


Figure 2.6: The addition of butanol and ethanol led to long strongly twinned crystals, which are not suitable for single-crystal X-ray diffraction

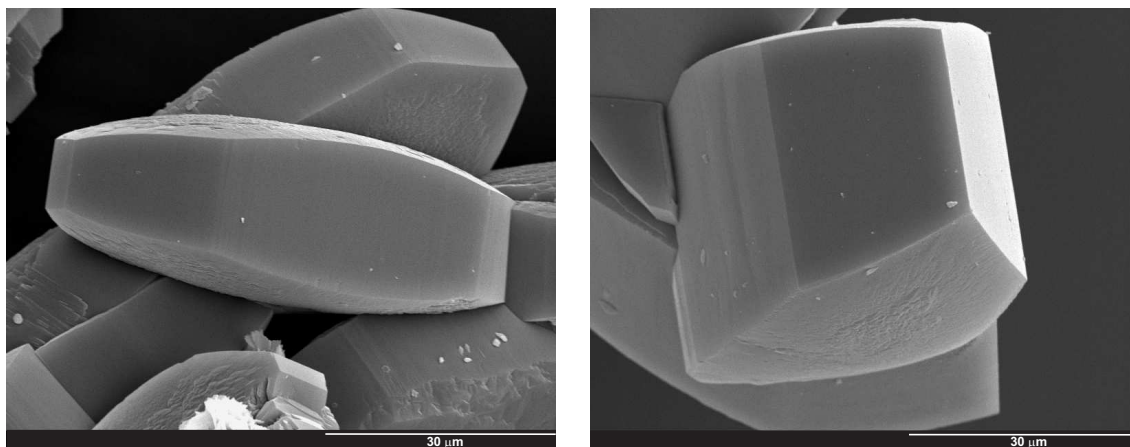


Figure 2.7: Large mordenite single crystal of an average size of $60\mu \times 50\mu \times 50\mu$. These crystals were used for subsequent guest-incorporation and X-ray diffraction.

of channels along the c-axis. Because the synthesis was performed at $175\text{ }^\circ\text{C}$, one can assume that the crystals are present as large-pore mordenites. Subsequent characterization showed no twinning but slightly curved faces (Fig. 2.7). The detailed synthesis procedure is summarized in Table 3.1 As mentioned above, the addition of an aliphatic alcohol may have a structure directing effect or causes a buffering for slower release of silicon and aluminium into the synthesis mixture.

Synthesis experiments performed in vessel A (larger cross-section) led in general to larger crystals of better quality. It can be assumed that the shape of the vessel also influences the synthesis results, and a larger vessel cross-section favors crystal growth.

The mordenite crystals synthesized in this study did not reach the dimensions reported by Warzywoda et al. [10]. This can have different reasons: (1) different chemical sources. Although chemicals with identical purity as reported by Warzywoda et al. [10] were used, chemicals from different suppliers still can have slightly different compositions or physical properties (pore size of silica). (2) different shape of the synthesis vessel. As it was already observed in our synthesis experiments, the shape and size of the synthesis vessel influences the synthesis products. (3) Aging of the source materials and different conditions of the pre-treatment of silica gel. Because silica is moisture-sensitive, the aging time and humidity after pretreatment may also influence the synthesis results.

Batch Composition 4.32Na₂O, 19SiO₂, 1Al₂O₃, 293.6H₂O

Source Materials

distilled water
sodium hydroxide (Hänseler)
sodium aluminate (Riedel-de Haen, anhydrous, technical)
silica gel (Aldrich, grade 62, 60-200 mesh, 150 Å; preheated 24 h at 850 °C under air)
ethanol

Batch preparation

- (1) [0.1858 g sodium hydroxide + 1.8277 g distilled water], stir until dissolved
- (2) [0.1147 g sodium aluminate and 1.8277g distilled water], stir until dissolved
- (3) [(1) + (2) + 0.7989 g preheated silica gel + 2 ml ethanol], mix and stir for 30 min.

Crystallization

Teflon autoclave, 50 ml
Temperature: 175 °C
Time: 120 h

Product recovery

- (1) Filter and wash
- (2) Dry at 100 °C

References

Warzywoda et al. (1995, 1996)

Table 2.1: Synthesis conditions for mordenite single-crystals.

Bibliography

- [1] R.M. Barrer. Sorptive and molecular-sieve properties of a new zeolitic mineral. *J. Chem. Soc*, 2:133–143, 1948.
- [2] D.W.Breck, W.G. Eversole, R.M. Milton, T.B. Reed, and T.L. Thomas. Crystalline zeolites. I. the properties of a new synthetic zeolite, Type A. *J. Am. Chem. Soc*, 1956.
- [3] H. Robson and K.P. Lillerud. *Verified Syntheses of Zeolitic Materials*. Structure Commission of the International Zeolite Association, 2001.
- [4] J. Warzywoda, M. Valcheva-Traykova G.A. Rossetti, N. Bac, R. Joesten, S. Suib, and A. Jr. Sacco. Characterization of zeolites a and x grown in low earth orbit. *J. Cryst. Growth*, 220:150–160, 2000.
- [5] R. Lilis. Fibrous zeolites and endemic mesothelioma in Cappadocia, Turkey. *J. Occupat. Medic.*, 23:548–550, 1981.
- [6] D.J. Stephenson, C.I. Fairchild, R.M. Buchan, and M.E. Dakins. A fiber characterization of natural zeolite mordenite: A potential inhalation health-hazard. *Aerosol Sci. Tech.*, 30:467–476, 1999.
- [7] L.B. Sand. Synthesis of large-pore and small-pore mordenites. In *Molecular Sieves*, Papers of Conference, Meeting Date 1967, pages 71–77, 1968.
- [8] Y. Sun, T. Song, S. Qiu, W. Pang, J. Shen, D. Jiang, and Y. Yue. Synthesis of mordenite single-crystals using two silica sources. *Zeolites*, 15:745–753, 1995.

- [9] T. Sano, S. Wakabayashi, Y. Oumi, and T. Uozumi. Synthesis of large mordenite crystals in the presence of aliphatic alcohol. *Microporous Mesoporous Materials*, 46:67–74, 2001.
- [10] J. Warzywoda, A.G. Dixon, R.W. Thompson, and A.Jr. Sacco. Synthesis and control of the size of large mordenite crystals using porous silica substrates. *J. Mater. Chem.*, 5(7):1019–1025, 1995.

3 Peculiarity and Defect Structure of the Natural and Synthetic Zeolite Mordenite: A Single-Crystal X-ray Study ¹

Petra Simoncic and Thomas Armbruster

Abstract

Single crystal X-ray data were collected on a natural fibrous mordenite of composition $K_{2.99}Ca_{1.85}Na_{1.06}Al_{7.89}Si_{40.15}O_{96} \times 28H_2O$ and on a platy, self-grown synthetic mordenite of composition $Na_6Al_{6.02}Si_{42.02}O_{96} \times 19H_2O$. Diffraction data were measured with a point detector using a sealed X-ray tube and an image plate using synchrotron radiation, respectively. Both structures exhibit the same defect features visible in difference-Fourier maps. Domains of the entire *Cmcm* framework structure are reproduced by a non-crystallographic (001) mirror plane at $z = 0$ and $z = 1/2$. An identical description is a shift of framework domains $1/2$ along the *c*-axis. The concentration of this defect domain is 2.7(2)% and 3.1(1)% for the natural and synthetic mordenite, respectively. Reproductions of reciprocal layers from synchrotron image-plate data reveal diffuse scattering for *hkl* layers with $l = 2n + 1$. The diffuseness of these layers is not homogeneous but concentrates in form of halos around selected reflections allowed for *C*-centering. Diffuse features in electron diffraction patterns of natural and synthetic mordenite have been described before and were interpreted either as evidence of *c/2* faults or intergrowth with different mordenite-related structure-types. We have modeled a (100) defect interface-layer that is modified from the mordenite characteristic puckered sheet of six-membered rings and allows coherent intergrowth of identical structural subunits shifted by *c/2*. The defect domains do not influence or obstruct the 12-membered ring-channels characteristic of this zeolite. The major difference in the Si, Al distribution between the two studied mordenite is that the natural crystal has Al strongly enriched in T3 that is part of the 4-membered rings. It is suggested that a synergetic effect between extraframework cations and Si, Al ordering during crystal growth is responsible for Al enrichment in natural mordenite with ca. 2 Ca pfu close to T3.

¹Lab. für chem. and mineral. Kristallographie. "American Mineralogist, Vol.89, p. 421-431, 2004

3.1 Introduction

3.1.1 Structure of zeolite mordenite

Mordenite is one of the most siliceous natural zeolites. It has an orthorhombic unit cell of topological space-group symmetry $Cmcm$ ($a = 18.13$, $b = 20.5$, $c = 7.52$ Å) with idealized chemical composition $\text{Na}_8\text{Al}_8\text{Si}_{40}\text{O}_{96} \times 24\text{H}_2\text{O}$. The structure of mordenite can be described as built by edge-sharing 5-membered rings of tetrahedra (secondary building unit 5-1) forming chains along c [1]. However, the mordenite framework can also be more comprehensibly envisioned as formed by puckered sheets parallel to (100), assembled of six-membered rings of tetrahedra [2, 3]. These sheets are interlinked by four-membered rings (Fig. 3.1) in a way that large, ellipsoidal 12-membered (12MRc: aperture 7×6.5 Å) and strongly compressed 8-membered rings (8MRc: aperture 5.7×2.6 Å) define channels parallel to c . six-membered rings of tetrahedra [2]. These sheets are connected along b by 4-membered ring pillars (dark gray shading) in a way that 12-membered ring channels (12MRc) and compressed 8-membered ring channels are formed, both extending along

Another set of compressed 8-membered rings (8MRb: aperture 3.4×4.8 Å) connects the wide channels with the strongly compressed channels parallel to b . At least for large extraframework ions and molecules mordenite has only a one-dimensional channel system for diffusion [4]. The eight-membered ring channels, running along b , which emerge from the wide tubes are staggered at the intersection with the strongly compressed channels (aperture 5.7×2.6 Å) before they end again in the wide tubes (Fig. 3.2)

Extraframework cations in mordenite mainly occupy three sites. Two of these sites are close to the 4-membered rings and are located in the connecting channels parallel to the b -axis. Another cation position is located in the center of the main 12-membered ring channel (e.g. [3]).

Natural mordenite occurs in rather large quantities in some altered vitreous tuffs. It has a characteristic fibrous habit and if fine crystalline it may be accounted to the group of asbestiform minerals causing lung diseases [5, 6]. Mordenite is also synthesized in large quantities, mainly for industrial application as catalyst. From a technical point of view two different varieties of mordenite are distinguished [7]. Large port

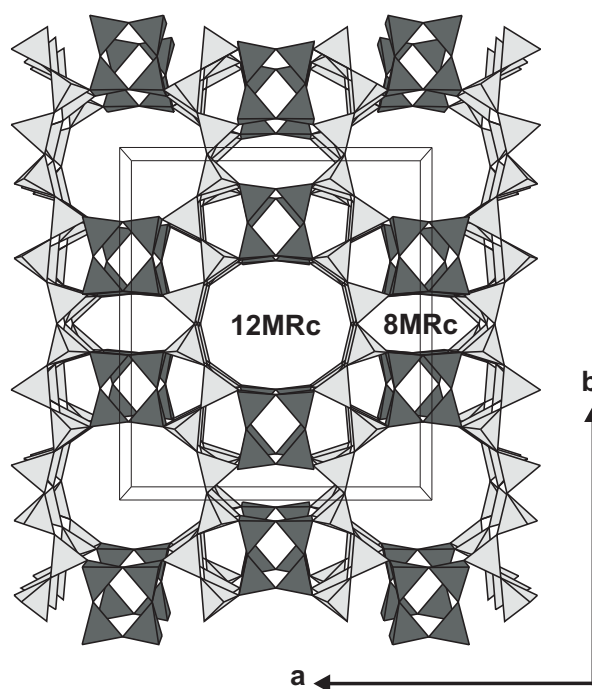


Figure 3.1: Tetrahedral framework structure of mordenite with unit cell outlines. The structure can be envisioned as built by pucker sheets (light gray shading) parallel to (100) formed by six-membered rings of tetrahedra [2, 3]. These sheets are connected along a by 4-membered ring pillars (dark gray shading) in a way that 12-membered ring channels (12MRc) and compressed 8-membered ring channels are formed, both extending along c .

mordenite exhibits the properties predicted for a zeolite with accessible 12-membered ring channels: (1) molecules with a diameter $> 4.5 \text{ \AA}$ can be introduced into the large channels; (2) the NH_4^+ and H-exchanged forms are able to crack significant amounts of hexane at $450 \text{ }^\circ\text{C}$. Large port mordenite is hydrothermally synthesized in the Na-form between $75 \text{ }^\circ\text{C}$ and $260 \text{ }^\circ\text{C}$. Small port mordenite accepts only molecules with a diameter $< 4.2 \text{ \AA}$ and is thus less favorable for industrial applications. Small port mordenites are usually obtained under hydrothermal synthesis conditions between $275 \text{ }^\circ\text{C}$ and $300 \text{ }^\circ\text{C}$ [7]. In addition, most natural mordenites have the properties characteristic of small port mordenite.

There are chemical recipes for transforming a small port mordenite into the large port variety and vice versa [7, 8]. The reasons responsible for small and large port behavior are controversially discussed. Following hypotheses have been put forward:

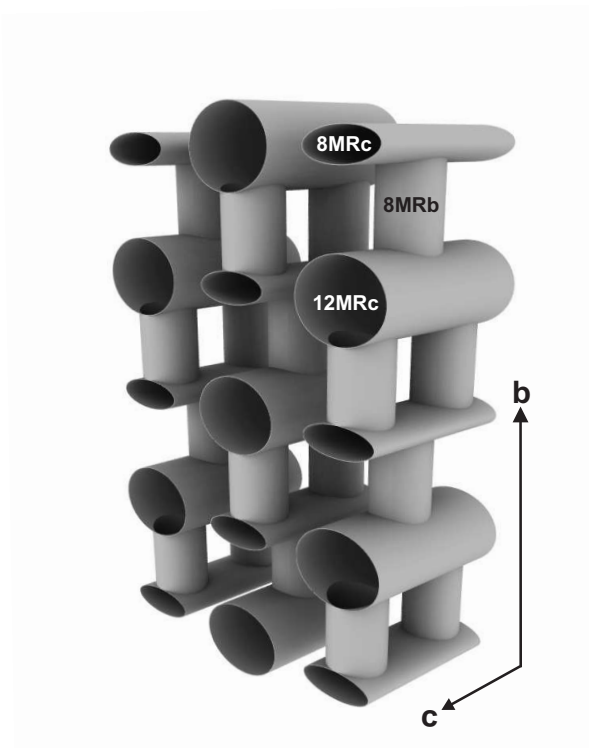


Figure 3.2: Plumbing system in mordenite accessible for extraframework cation and molecule diffusion. Notice that there is no straight connection between adjacent 12MRc tubes. The linking 8MRb tubes are staggered at the join with the strongly compressed 8MRc tubes. Thus for diffusion of large ions or molecules the structure of mordenite offers only one-dimensional passageways.

(1) location of extraframework cations, (2) the presence of amorphous material plugging the structural windows, (3) stacking faults disrupting the continuity of the large channels. In particular the latter argument has widely been accepted for the varying properties of mordenite [8]. There is a striking difference in morphology of the natural (fibrous) and most synthetic mordenite (platy). Hamidi et al. [9] suggest, based on a series of hydrothermal growth experiments, that the alkalinity of the system is the main factor influencing the crystal morphology. At low alkalinity platy crystals are formed whereas at higher alkalinity the crystals become more prismatic. On the other hand, Sano et al. [10] were able to change the morphology of mordenite grown under corresponding conditions by addition of different aliphatic alcohols (methanol - 1-decanol), which were not incorporated into the zeolite channel system. The mor-

phological aspects are important for technical applications. The dominant (001) faces of platy mordenite enable easy access to the large 12-membered ring channels. Long prismatic or fibrous (along c) crystals have lesser openings of the large channels and diffusion will be more sluggish. It seems that morphology is an additional parameter influencing small port and large port behavior.

Even though the crystal structure of mordenite was solved in the early sixties [1] and much work has been done in this field since then, there are still open questions, which are not yet convincingly solved. Problems such as pseudo-centrosymmetry, Si, Al order, extraframework cation-distribution, framework defects, faulting, and diffuse scattering have been addressed by several authors.

3.1.2 Pseudosymmetry

First structural refinements were carried out on a Na-exchanged, natural mordenite in space group $Cmcm$ [1], but lower, acentric symmetry was already supposed due to Si, Al ordering and a suspicious T-O-T angle of 180° . Structure models of different symmetry, coherently intergrown with each other, were suggested yielding two different Si, Al conformations of the 4-membered rings [11]. Although the Si, Al framework showed strong pseudo-centrosymmetry, the extraframework cation-distribution pointed to an acentric arrangement [12]. Symmetry lowering from $Cmcm$ to $Cmc2_1$ prevented the energetically unfavorable 180° T-O-T angle that appeared in the $Cmcm$ refinement, and led to a better description of the extraframework cation-distribution. Although the characterization of the mordenite structure was highly improved by the acentric space group $Cmc2_1$, refinement in the centric space group $Cmcm$ is still applied in many crystallographic studies involving the mordenite structure [13, 14].

3.1.3 Framework defects and diffuse scattering

Crystallographic faulting in mordenite has been discussed by several authors either on a theoretical basis or by applying electron and X-ray diffraction methods. The reasoning of most studies of this type is to understand the enigmatic small- and large-port behavior of mordenite.

Kerr [15] suggested a hypothetical structure of space-group symmetry $Immm$, closely related to mordenite, but of distinct topological symmetry due to different heights of

the 4-membered rings of tetrahedra along c . The field of hypothetical structures related to mordenite was elaborated by Sherman and Bennett [16] predicting additional structures of $Cmmm$ and $Imcm$ symmetry where the 4-membered rings are attached at different levels along c . In all these hypothetical structures the 12- and strongly compressed 8-membered ring channels run along c at the same position as in $Cmcm$ mordenite. The same authors interpret X-ray powder patterns of synthetic and natural mordenites to show the dominant effect of the normal $Cmcm$ structure of mordenite with subordinate intermingled $Cmmm$, $Immm$, and $Imcm$ structures. Electron diffraction patterns of mordenite from Challis Valley, Idaho, showed streaks in $h0l$ section where the streaks were occasionally decorated with diffuse maxima interpreted as intergrowth of $Cmcm$, $Cmmm$, $Immm$, and $Imcm$ structures [16]. Crystals of the hypothetical $Cmmm$, $Immm$, and $Imcm$ structures have never been found neither in synthetic products nor in nature.

Meier [2] argued that the above hypothetical structures lack the puckered (100) sheet formed by six-membered rings of tetrahedra. These sheets are characteristic of mordenite group zeolites comprising also dachiardite, epistilbite, ferrierite, and bikitaite (e.g. [3]). Electron diffraction experiments on natural and synthetic mordenite [17] showed that there are layers of diffuse scattering perpendicular to \mathbf{c}^* restricted to planes with Bragg indices $l = 2n + 1$ where the scattering is concentrated around reciprocal hkl lattice points allowed for C -centering (e.g. 111, 311, 511). The intersection of the Ewald sphere with the diffuse layers produces the continuous streaks in the $h0l$ section discussed by Sherman and Bennett [16]. The electron diffraction results [17] were interpreted to be caused by linear faults parallel to the c -axis which is the direction of the major channels. However, there was no indication of stacking faults normal to [001] blocking the main channels as originally suggested by Meier [1]. The diffuse streaks restricted to $l = 2n + 1$ together with anomalies reported in powder diffractograms were interpreted either due to c -axis faulting, intergrowth of different crystal varieties [14] or as a $c/2$ displacement of linear chains parallel to the main [001] channels [18]. Song [19] investigated defects in a commercial mordenite by high-resolution electron microscopy (HREM) and found in addition to dislocations with a displacement vector of $1/2$ [110] also two- and three-dimensional defects. The most frequent planar faults are displaced by $1/4$ [010] resembling dachiardite thus the pore size along c at the intergrowth boundary is reduced. Furthermore, blocks of dachiardite could be identified intergrown

with the mordenite matrix.

This study presents (1) successful synthesis of mordenite single crystals with sufficient quality for single crystal diffraction and (2) single crystal diffraction data of both synthetic and natural mordenite to investigate the defect structure.

3.2 Experimental

3.2.1 Studied samples

For structural analysis a fibrous natural and a platy synthetic zeolite were used. The natural, K-rich mordenite single-crystal from Jarbridge, Nevada (Museum of Natural History Bern, NMBE-A9472), originating from jasper covered vesicles of a strongly altered volcanic rock, was chemically analyzed by electron microprobe yielding the composition $\text{K}_{2.99}\text{Ca}_{1.85}\text{Na}_{1.06}\text{Al}_{7.89}\text{Si}_{40.15}\text{O}_{96} \times 28\text{H}_2\text{O}$. Pure mordenite-Na crystals were synthesized hydrothermally in the home lab after a modified method by Warzywoda et al. [20].

As discussed by Warzywoda et al. [20, 21] the mordenite crystal-size strongly depends on the surface area and porosity of the amorphous silica gel applied as SiO_2 source in the hydrothermal runs. The properties of silica gel are altered by subsequent heat treatment at elevated temperature [20, 21]. After a series of test runs under various conditions we decided to add a small amount of ethanol (e.g. [10]) leading to an increase of the crystal size. The exact synthesis conditions are summarized in Table 3.1.

The crystallization products were 100% mordenite with platy and uniform morphology. The run products were studied with a polarizing microscope and the single crystals were examined with a scanning electron-microscope and showed well-defined, but slightly curved faces and no apparent twinning. Average size of the mordenite crystals was about $0.06 \times 0.04 \times 0.05$ mm (Fig. 3.3).

The chemical composition of the synthetic mordenite determined by electron microprobe was $\text{Na}_6\text{Al}_{6.02}\text{Si}_{42.02}\text{O}_{96} \times n\text{H}_2\text{O}$. The Si/Al ratio of 7/1 is in exact agreement with the analytical data given by Warzywoda et al. [20] for their synthesis products obtained under corresponding conditions. According to Sand [7] the applied synthesis conditions (175 °C and excess of sodium silicate) should lead to large port morden-

Batch Composition	4.32Na ₂ O, 19SiO ₂ , 1Al ₂ O ₃ , 293.6H ₂ O
Source Materials	distilled water sodium hydroxide (Hänseler) sodium aluminate (Riedel-de Haen, anhydrous, technical) silica gel (Aldrich, grade 62, 60-200 mesh, 150 Å; preheated 24 h at 850 °C under air) ethanol
Batch preparation	(1) [0.1858 g sodium hydroxide + 1.8277 g distilled water], stir until dissolved (2) [0.1147 g sodium aluminate and 1.8277g distilled water], stir until dissolved (3) [(1) + (2) + 0.7989 g preheated silica gel + 2 ml ethanol], mix and stir for 30 min.
Crystallization	Teflon autoclave, 50 ml Temperature: 175 °C Time: 120 h
Product recovery	(1) Filter and wash (2) Dry at 100 °C
References	Warzywoda et al. (1995, 1996)

Table 3.1: Synthesis conditions for mordenite single-crystals.

ite. This property was tested by ion-exchange with diluted solutions of bulky, organic dye molecules [22] such as thionine blue (C₁₂H₁₀N₃S⁺), methylene blue (C₁₆H₁₈N₃S⁺), DAMS⁺ (C₁₆H₁₉N₂⁺), and benzothiazole dye (C₁₁H₁₄NS⁺). Successful incorporation of dye ions could be monitored by polarized light microscopy showing characteristic colors and pleochroism of the individual crystals [23].

3.2.2 X-ray data collection

X-ray data collection of the fibrous natural mordenite (0.05 × 0.05 × 0.30 mm, elongated parallel to *c*) was performed at room temperature with an Enraf Nonuis CAD4 single-crystal diffractometer using graphite monochromated MoK α radiation. Additional experimental details are summarized in Table 3.2. Data reduction, including

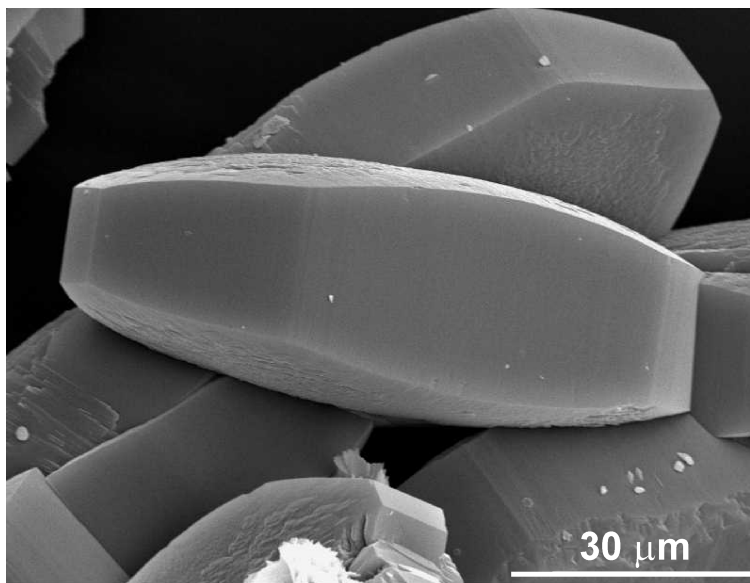


Figure 3.3: Scanning electron microscopic image of synthetic, platy mordenite of $\text{Na}_6\text{Al}_6.02\text{Si}_{42.02}\text{O}_{96} \times 19 \text{H}_2\text{O}$ composition. Notice that the (001) face is rough and slightly curved. The large channels (Figs. 3.1 and 3.2) run perpendicular to this face.

Lorentz and polarization correction was performed with the SDP program package [24]. X-ray data collection of the synthetic mordenite was performed at room temperature with synchrotron radiation (wavelength $\lambda = 0.70192 \text{ \AA}$) on the single-crystal diffraction line at SNBL (ESRF, Grenoble) where diffracted intensities were registered with a MAR image plate. Data reduction was performed with the program package CrysAlis [25]. In the single-crystal diffraction pattern of the synthetic mordenite, measured by synchrotron radiation, 76 reflections were observed which should be systematically absent, all with hkl values of $h + k = 2n$ and $l = 2n + 1$. Observation of these forbidden reflections is an artifact related to the frame-integration procedure and coincides with the diffuse scattering described below. Additional experimental details are in Table 3.2.

3.2.3 Structure refinement

Structure refinement for both samples was carried out with the program SHELXL97 [26], using neutral-atom scattering factors (Si for all tetrahedral sites - labeled T sites).

Refinements were performed with anisotropic displacement parameters for all framework sites and highly populated extraframework positions. We have chosen a model of $Cmc2_1$ space-group symmetry. However, to reduce correlation effects due to pseudo-symmetry, we have constrained all framework atomic coordinates and displacement parameters to the counterpart related by an inversion operation (constrained sites are labeled with an additional prime symbol). Thus the tetrahedral framework is actually refined for $Cmcm$ symmetry. $Cmc2_1$ symmetry accounts only for the extraframework part of the structure. The atom O8 linking the tetrahedra T2 and T2' with a T-O-T angle of 180° showed strong smearing perpendicular to the T-O bond. This O8 site was split in 4 closely spaced (ca. 0.5 \AA) isotropic positions for which site-occupancy refinement yielded 25% occupancy each.

3.2.4 Diffuse scattering

After determining the common Si, Al framework and the extraframework cations and molecules, peaks remained in the difference Fourier map (Fig. 3.4 and 3.5) of both the natural and synthetic sample. These peaks could not be assigned to extraframework occupants because distances to framework oxygen were too short. In addition, the coordinates of these peaks correspond almost exactly to the x , y -coordinates of the framework atoms but differ in the z -coordinate. Most obvious are the difference-Fourier peaks originating (Fig. 3.4) from the 4-membered rings of tetrahedra shifted $1/2$ along c also reported by Mortier et al. [27] for a dehydrated hydrogenated mordenite.

If the residual peaks in the difference-Fourier map are analyzed in detail counterparts of all framework positions can be found shifted $1/2$ along c . Consequently the entire Si, Al framework is repeated but shifted by $c/2$. This unidirectional translation of the framework, referred to as 'domain B', may also be described by a (001) mirror plane at $z = 0$ and $z = 1/2$. Notice that in $Cmcm$ symmetry the (001) mirror plane is at $z = 1/4$ and $z = 3/4$. Fig. 3.4 shows the (010) difference Fourier map section at $y = 0.38$ (which is close to the y -coordinate of the T3 and O9 framework atoms). The contoured peaks in the center of the rings correspond to the T3 and O9 atoms of the domain B. The z -coordinate of T3 and O9 is $1/4$ whereas z for T3B and O9B is $3/4$. Correspondingly, T4 and O10 of the B domain can be found at a (010) section with $y = 0.23$. To demonstrate that not only the 4-membered ring pillars but the entire

Sample	Natural Mordenite	Synthetic Mordenite
Crystal size (mm)	0.05 × 0.05 × 0.30	0.06 × 0.04 × 0.05
Diffractometer	Enraf Nonius CAD4	Mar image plate
X-ray radiation	MoKα	Synchrotron (0.70192 Å)
Temperature	293 K	293 K
Space Group	<i>Cmc2₁</i>	<i>Cmc2₁</i>
Cell dimensions (Å)	18.096(4), 20.473(4), 7.515(2)	18.131(2), 20.507(2), 7.5221(5)
Absorption corr.	Empirical ψ -scans	none
Maximum 2θ	55.95	64.59
Measured reflections	3692	25625
Index range	-10 ≤ h ≤ 23, -2 ≤ k ≤ 26, -1 ≤ l ≤ 9	-27 ≤ h ≤ 27, -30 ≤ k ≤ 30, -11 ≤ l ≤ 11
Unique reflections	2099	5023
Reflections > 4 σ (F_o)	1283	4930
R_{int}	0.0205	0.0483
R_σ	0.0398	0.0236
Number of l.s. parameters	178	163
Goof	0.975	1.206
R1, $F_o > 4\sigma$ (F_o)	0.0335	0.0524
R1, all data	0.0855	0.0536
wR2 (on F_o^2)	0.0991	0.1360

Table 3.2: Experimental parameters for X-ray data collection and refinement of natural and synthetic mordenite.

framework is reproduced by $c/2$ shifts, Fig. 3.5 shows the (010) section of the difference Fourier map at $y = 0.07$, where the contoured peaks correspond to the T1B, T1B', O1B and O1B' atoms. T2B, T2B', O2B and O2B' can correspondingly be found at a (010) section with $y = 0.31$. In subsequent refinement cycles, the atomic coordinates of the $c/2$ -shifted domain (B domain) were constrained to have identical x, y -coordinates as the major part of the structure and z of the so called B domain atoms was fixed at $z + 1/2$. The only exception is O8 (split into O8a, O8b, O8c, and O8d), which is common to both structural parts.

Finally, a common population factor for all framework atoms of the A and B domain, respectively, was refined constraining $A + B = 1$. This refinement approach is consistent with the 'fault plane model' used by Rudolf and Garces [14] in Rietveld refinements of synthetic mordenites. Introduction of the B domain in the refinement model of the natural mordenite lowers R1 by ca. 0.5% and wR2 by ca. 1%.

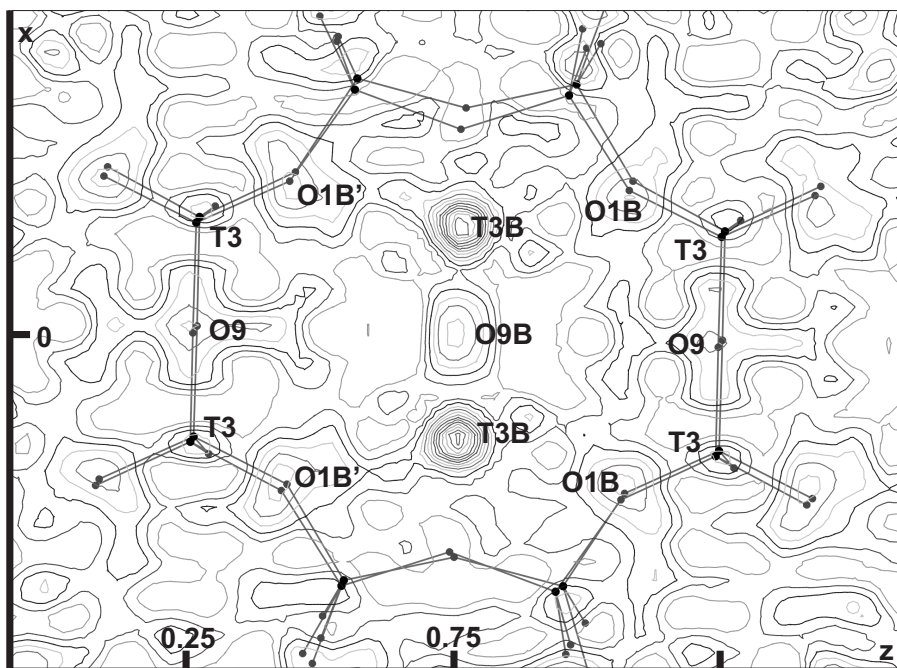


Figure 3.4: Difference-Fourier map of natural mordenite after introducing framework and extraframework positions. The (010) section at $y = 0.38$ shows a cross-section of the 8MRb channels. In addition, residual peaks (contours at 0.05 electrons intervals) in the center of the 8-membered ring indicate a replication of the T3-O9-T3 unit (edge-wise view of the 4-membered ring) but shifted $1/2$ along c .

3.3 Results

3.3.1 Diffuse scattering

The X-ray single-crystal diffraction pattern from the synchrotron data show sharp Bragg reflections, but there are also diffuse intensities modulating the background of selected sharp peaks. To visualize the diffuse scattering, reciprocal space reconstructions of $hk0$, $hk1$, $hk3$, $h0l$, $h1l$, $h2l$, $0kl$, $1kl$, $2kl$ layers were calculated using CrysAlis software package [25]. Generally speaking, diffuse scattering is absent in all reciprocal layers with $l = 2n$, e.g. in $hk0$ and $hk2$. Diffuse scattering is also absent in the $h2l$ layer. Layers of the type hkl with $l = 2n + 1$ are diffuse where the diffuseness is not homogeneous but particularly concentrated around selected hkl reflections with $h + k = 2n$ (allowed by C -centering) as exemplified in the layers $hk1$ and $hk3$ (Figs. 3.6,

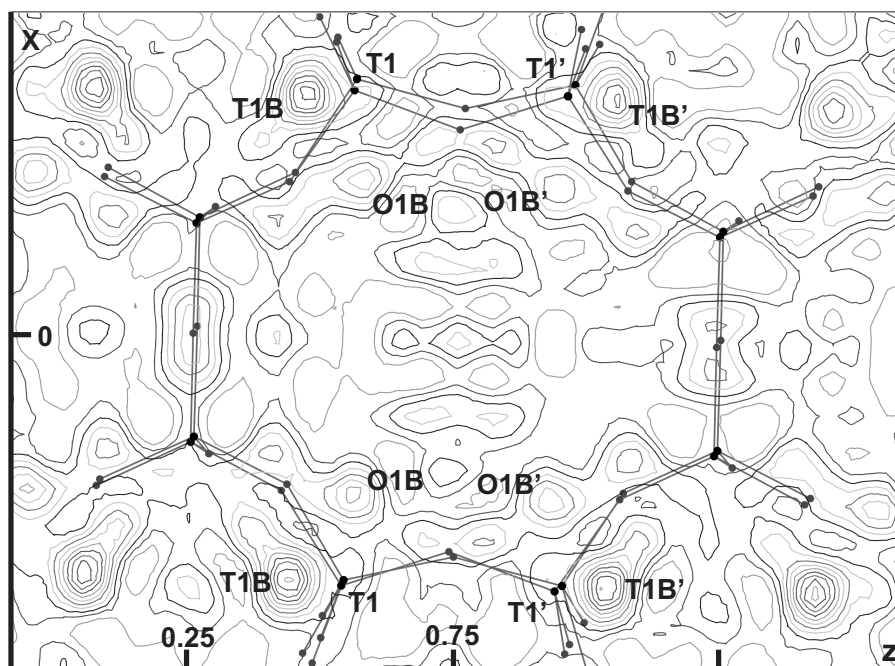


Figure 3.5: Difference-Fourier map of natural mordenite after introducing framework and extraframework positions. The (010) section at $y = 0.07$ shows a cross-section of the 8MRb channel. In addition, residuals peaks (contours at 0.05 electrons interval) indicate a replication of the T1 site but shifted $1/2$ along c . In addition, residual electron density of replicated O1B and O1B' (center at $y = 0.09$) can be seen. T1 and O1 are part of the puckered sheet of tetrahedra. This section shows that not only the 4-membered ring pillars are shifted by $c/2$ (Fig. 3.4) but also the adjacent tetrahedral (100) sheets.

3.7). Scattering (reflection smearing) is most accentuated around the reflections 511, 0.12.1 in $hk1$, and 713, 11.13, 443, 843, 10.43, 593, 2.12.3 in $hk3$.

If the diffuse sheets with $l = 2n + 1$ are viewed in $0kl$, $1kl$, $2kl$ reciprocal layers (Fig. 3.8) the diffuse sheets appear as diffuse streaks parallel to \mathbf{b}^* decorated by sharp Bragg reflections. If the diffuse sheets with $l = 2n + 1$ are viewed e.g. in $h0l$ reciprocal layers (Fig. 3.9) the diffuse sheets appear as diffuse maxima smeared along \mathbf{a}^* at $h = 2n + 1$, $l = 2n + 1$. Notice that no reflections should occur in $h0l$ layers at $l = 2n + 1$ because of the c -glide in (010) for space group $Cmcm$ or $Cmc2_1$. The observed smeared maxima are diffuse residuals of the halos around the reflections in adjacent $h1l$ layers (e.g. reflections 511, 713). In other words, diffuse streaks or maxima in $0kl$ or $h0l$ layers are just traces of the diffuse hkl layers with $l = 2n + 1$.

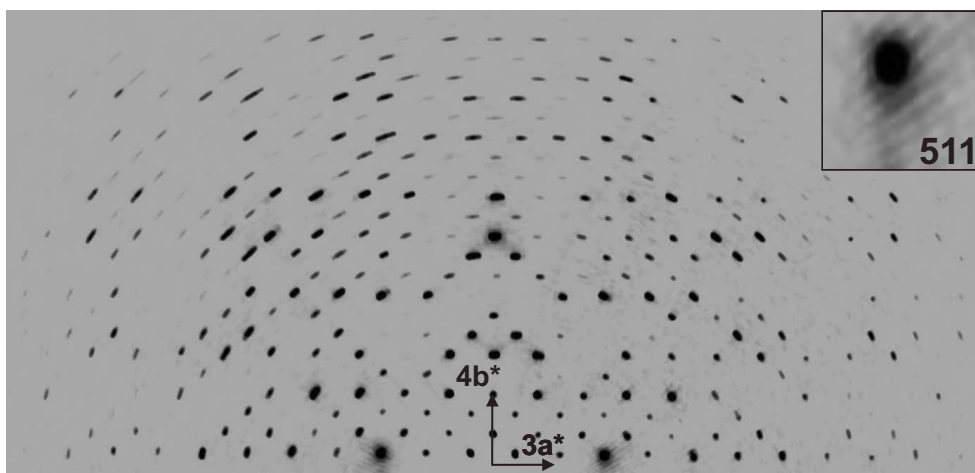


Figure 3.6: Reconstruction of the reciprocal $hk1$ layer from area detector measurements (synchrotron radiation) of a synthetic mordenite. Notice the diffuse halos particularly around the 511 and 0.12.1 reflection. The rod at $k = 0$ is extinct due to the c -glide in (010). However, the diffuse halos around 511 are smeared towards this empty rod. The slight radial streaking of the diffuse intensity is an artifact due to the reconstruction of the layer.

3.3.2 Bragg reflections

The results of the structure refinement, comprising atomic coordinates, populations, and isotropic displacement parameters are given in Tables 3.3 - 3.4 and 3.5 - 3.6 and for the natural and synthetic mordenite, respectively. Tables 3.7 and 3.8 summarize T-O distances and T-O-T angles of the tetrahedral framework. Anisotropic displacement parameters are in Tables 3.9 and 3.10. All tables are deposited in the "Crystallographic data" part of this chapter.

3.4 Discussion

3.4.1 Si, Al arrangement

Distortions within the tetrahedral framework structure are very similar for synthetic and natural mordenite as estimated from T-O-T angles (Tables 3.7 and 3.8). Major differences in T-O-T angles occur only for angles within the 4-membered rings. These angles are in the synthetic mordenite ca. 2° larger than in the natural one. Removing

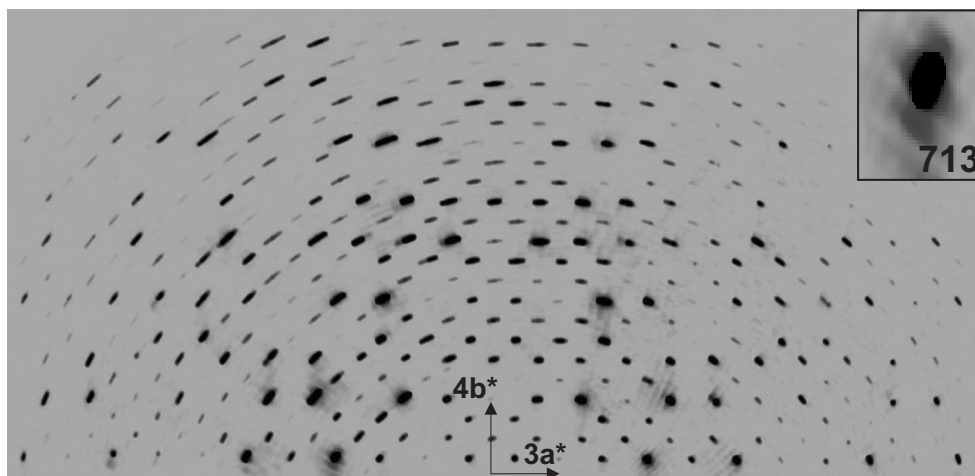


Figure 3.7: Reconstruction of the reciprocal $hk3$ layer from area detector measurements (synchrotron radiation) of a synthetic mordenite. Notice the diffuse halos particularly around following reflections: 713, 11.13, 443, 843, 10.43, 593, 2.12.3. As in Fig. 3.6, the rod at $k = 0$ is systematically extinct. However, the diffuse halos of the reflections 713 and 11.13 are smeared towards this empty rod. The slight radial streaking of the diffuse intensity is an artifact due to the reconstruction of the layer.

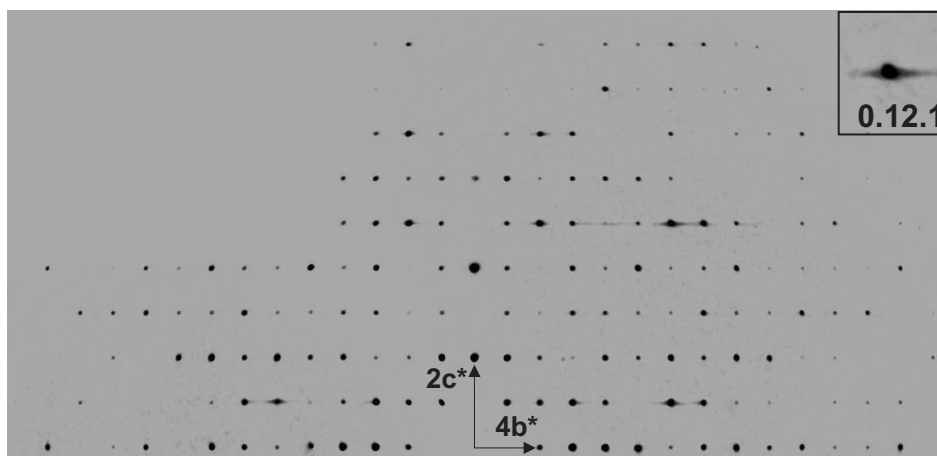


Figure 3.8: Reconstruction of the reciprocal $0kl$ layer from area detector measurements (synchrotron radiation) of a synthetic mordenite. Notice the streaking along b^* of the rods with $l = 2n + 1$.

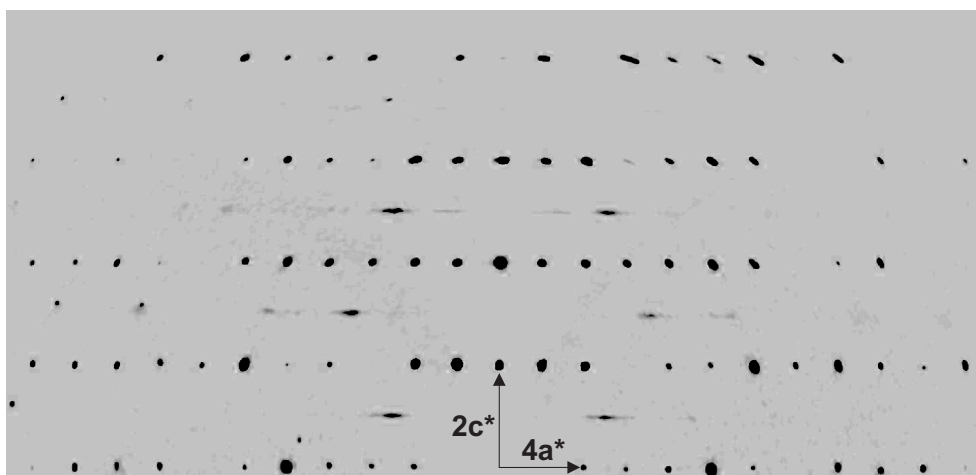


Figure 3.9: Reconstruction of the reciprocal $h0l$ layer from area detector measurements (synchrotron radiation) of a synthetic mordenite. Notice the streaked intensities at 501, 703, 11.03, 505 etc. Corresponding intensities have been observed before in electron-diffraction studies and were interpreted as evidence for domains of I -centered symmetry (e.g. [16]). These fake reflections are artifacts caused by the diffuse smearing of reflections in \mathbf{b}^* adjacent layers as shown in Figs. 3.6 and 3.7.

O8 from the inversion center and splitting it up into four 25% occupied sites reduced the T2-O8-T2' angle from 180° to 155 - 167° . Judging from the average $\langle\text{T-O}\rangle$ bond length there is also a significant difference in Si, Al order between the natural and the synthetic mordenite. The $\langle\text{T1-O}\rangle$ and $\langle\text{T2-O}\rangle$ bond lengths of the synthetic crystal are slightly larger than for the natural one. On the other hand $\langle\text{T3-O}\rangle$ and $\langle\text{T4-O}\rangle$ bond length of the natural crystal are larger than for the synthetic one. T1 and T2 tetrahedra assemble the puckered (100) sheets whereas T3 and T4 tetrahedra belong to the 4-membered rings connecting the sheets to a framework.

It has been shown before [12, 28] that the Jones relationship [29] ($\text{Al} = 6.4116 \langle\text{T-O}\rangle - 10.282$) fails to predict reliable Al concentrations for mordenite. Actually, the Jones relationship [29] yields 4.36 Al pfu (measured 7.89 Al pfu) for the natural crystal and 4.82 Al pfu (measured 6.02 Al pfu) for the synthetic one. We have also applied a riding correction [30] for T-O bond length (due to rigid librational disorder of TO_4 moieties). However, the T-O riding correction is very similar for both structures and can not explain the drastic Al underestimation for the natural crystal. If we normalize, as a rough estimate, the Al distribution from the Jones relationship [29] to the analyzed Al

concentration we obtain following Al distribution pattern T1 (nat: 0.14, syn: 0.13), T2 (nat: 0.03, syn: 0.08), T3 (nat: 0.41, syn: 0.20), T4 (nat: 0.24, syn: 0.13). The values for the natural crystal are actually very similar to the normalized average calculated by Alberti [31] for literature data of natural or ion-exchanged natural mordenites.

Unfortunately the series of Rietveld powder refinements [13, 14] on synthetic mordenites with Al between 3.55 and 7.87 pfu does not, due to insufficient quality of T-O bond lengths, allow drawing any conclusion on Si, Al order. All natural mordenites [32] have approximately 2 Ca pfu as extraframework occupants. Ca occupies the center of the 8MRc ring (this study and [12, 33]) and bonds to O1, O1', and O9 which are additionally bonded to T3 that is strongly Al enriched in natural samples. Thus we suggest a synergetic effect between extraframework occupants and Si, Al order during crystal growth. In synthetic mordenite, grown in a pure Na alkaline environment, there is less extraframework charge close to T3 and correspondingly less Al on T3 for local charge balance. Analogous interplay between extraframework cations and Si, Al order has been analyzed for heulandite [34] and was considered responsible for different selectivity of alkali and alkaline earth cations in exchange experiments [35].

3.4.2 Extraframework cations

The analytically determined extraframework cation content of the natural mordenite was $K_{2.99}Ca_{1.85}Na_{1.06}$ whereas the composition $K_{2.77}Ca_{1.86}Na_{1.90}$ was obtained from structure refinement. The excess of refined Na may be explained by some Na/H₂O disorder. Ca (population 0.47) is situated in the center of the strongly compressed eight-membered channel and has short distances to the framework oxygen O1, O1', O9 (2×2.87 , 2×2.87 , 2×2.69 Å) and bonds twice to H₂O molecule W1 (2.29, 2.35 Å) with an 180° angle. If we further assume that the site assignment of Ca is correct [12, 33] then ca. 4.8 positive charges pfu remain in 12MRc and are easily accessible for cation exchange. K1 (1.36 pfu) is split into K1a (population: 0.24) and K1b (population: 0.10), separated by 0.8 Å along *c*. These sites are not bonded to the tetrahedral framework but are surrounded by strongly disordered H₂O in 12MRc whereas K3 occupy pockets, which are defined as the transit from 12MRc to 8MRb. Na2a (population: 0.47) and K2b (population: 0.11) are separated by 1.2 Å along the *c*-axis. Therefore, K2b appears to be a satellite position indicating translational

disorder along the c -axis. Na2a has no bonds to the tetrahedral framework whereas K2b bonds $2 \times$ to O2 (2.71 Å) and $1 \times$ O10 (2.65 Å). The K3 site was identified by their long distances to the framework with two bonds to O5 (3.09 Å) and one bond to O2' (3.12 Å).

The synthetic mordenite has 6 Na in the channel system where 5.5 Na pfu were located by the structure refinement. With 2.3 Na1 pfu (population: 0.29) located in the strongly compressed 8MRc, ca. 3.7 positive charges are in 12MRc. In contrast to the Ca site in the natural mordenite the corresponding Na1 site in the synthetic mordenite is shifted from the special position and has four short bonds to the tetrahedral framework (Na1-O1: 2.64, Na1-O9: 2.69 and 2.80, Na1-O1': 2.80 Å). Na2 and Na3 (2.2 pfu) are not bonded to the tetrahedral framework but are surrounded by strongly disordered H₂O in 12MRc and only Na4a,b (1 pfu) occupy the pocket at the transition to 8MRb but without short bonds to the framework.

3.4.3 Limitations of Bragg model

Even after introducing the domain B, there are various weak peaks ($< 0.5 \text{ e}/\text{Å}^3$) in the difference Fourier map from the synchrotron data of the synthetic crystal which could be interpreted as indicator of a slightly different conformation within the puckered (100) sheet formed by six-membered rings. These peaks have either suspicious distances of 1.6 Å to existing T sites or they are approximately 1.6 Å from located oxygen sites. Considering the high quality synchrotron data and the significant but very low contribution from diffuse scattering there are some nonsatisfying parameters in Table 2. The value R_{int} , estimating the agreement of symmetry equivalent reflections, is twice as high as R_σ from counting statistics. Even the R_1 and wR_2 values (agreement between structure model and observed structure factors) determined in the course of the structure refinement are rather high.

We offer three explanations for the above insufficiencies: (1) The diffraction data contain also information on the defect (100) layer (discussed below) which becomes necessary to link two identical structural blocks shifted by $c/2$. (2) Contributions from Bragg diffraction and diffuse scattering were not discriminated in the peak integration procedure. Thus the integrated intensity of Bragg reflections is significantly influenced by the diffuse-scattering contribution. This is especially important for weak or even

symmetry forbidden reflections, which are influenced by the diffuse halos of adjacent reflections. And (3) The assumed *Cmcm* pseudosymmetry of the tetrahedral framework is only a fair approximation. This latter argument is supported by the microtwin model [11, 36].

3.4.4 Defects and crystallographic faulting

First investigations of possible faults were discussed by Sherman and Bennett [16] suggesting *Cmmm*, *Immm* and *Imcm* intergrowth with *Cmcm* symmetry in the mordenite structure. Based on our diffuse scattering results and the electron diffraction pattern discussed by Sanders [17] this intergrowth model must be viewed with skepticism because it is mainly based on space group violating reflections in $h0l$ reciprocal layers. As discussed above such diffuse reflections are artifacts and result from diffuse halos of adjacent layers. The probable misinterpretation of structural intergrowth [16] is related to the lack of electron diffraction patterns along [001] which were difficult to access at this time due to the fibrous character and the pronounced (100) cleavage of mordenite. Thus a correct interpretation of diffuse diffraction maxima in $h0l$ layers was hampered. There are highly confusing evidences in the literature concerning the importance of $c/2$ faults in synthetic mordenite. Better understanding of this subject becomes best evident in a short historic review.

Mortier et al. [27] studied a natural but modified mordenite from Challis Valley, Idaho. After refining the tetrahedral framework structure Mortier et al. [27] noticed in difference Fourier maps a repetition of 4-ring pillar domains, ca. 2% (composed of T3B, T4B, O4B, O9B, O10B) shifted by $c/2$ relative to the 4-ring pillars of the major *Cmcm* structure. The same type of defects (ca. 4%) was also observed for dehydrated and rehydrated K-exchanged mordenite from the same locality [37]. A series of very fine crystalline synthetic mordenites with varying Si/Al ratios between 5.1 and 9.5 was produced by Itabashi et al. [38]. X-ray powder diffractograms of these mordenites exhibited intensity ratios of the reflections 111/130 and 241/002 which increased linearly with Si/Al ratio. Thus these intensity ratios were considered characteristic of the Si/Al ratio in mordenite. In a subsequent Rietveld refinement by Shiokawa et al. [13] of essentially the same samples, it was stated that there is no substantial change in the framework with Si/Al ratio and that the observed variation in powder intensity

ratios can be explained by shifts and occupancies of the extraframework atoms. Rudolf and Garcés [14] analyzed the theoretical influence of the $c/2$ shifted 4-ring pillars on the X-ray powder pattern and restudied samples from the same source as Shiokawa et al. [13] by Rietveld methods suggesting that $c/2$ faults not only relate to the 4-ring pillars but to complete structural domains of the $Cmcm$ structure. They subsequently refined the large value of 21% of $c/2$ shifted domains from powder data of synthetic sodium mordenite with $\text{Si}/\text{Al} = 5.25$.

The striking dependence of the 111/130 reflection-intensity ratio in X-ray powder patterns with the Si/Al ratio in the mordenite framework was revived by Campbell and Cheetham [18] analyzing the theoretical influence of $c/2$ shifts on this intensity ratios. Campbell and Cheetham [18] determined that the odd- l reflection intensities are rapidly extinguished as the $c/2$ defect concentrations increase, while the even- l intensities are relatively unaffected. As conclusion they offer a semi-quantitative diagram for defect concentration versus Al content in the framework. For our compositions (nat. = 16 % Al, syn. = 12.5% Al) ca. 0.25 and ca. 0.15 defect portions would be predicted. This is almost one order of magnitude higher than the $c/2$ defect concentrations determined in this study (0.027 and 0.031, respectively). The physical argument [18] for the increase of defect concentration with Al content is: 'During crystal formation, the longer Al-O bonds may cause a new pillar to bond more favorably at the $c/2$ shifted position. Once initiated, such a defect could propagate along [001] during subsequent crystal growth in order to avoid the disruptive pillar spacings associated with its termination.

A general relationship between Al-content and defect concentration as might be derived from the arguments by Campbell and Cheetham [18] and Rudolf and Garcés [14] cannot be confirmed by our data. Well-crystallized synthetic mordenites do not follow this trend. In contrast, they show similar defect concentrations as found for well-crystallized natural mordenites. It seems that crystal growth conditions are more decisive than just the Al concentration in the framework. Furthermore, the fact that in structure refinements of natural mordenites (with ca. 15 -20% Al) either only very weak indications of B type domains were detected or these domains could not be resolved suggests that in none of these studies B type domains exceeded concentration levels above ca. 5%. This is an additional argument against a general relationship between Al concentration and amount of B type domains.

3.4.5 Structural model for the interface of the defect layer

The occurrence of two domains, which exist side by side in the mordenite structure, makes it necessary to find a structural conformation for a coherent connection of such domains. As already stated by Meier [2] 4-ring pillars cannot be shifted along c without reconstruction of the puckered (100) sheets. A possible linkage is presented which is consistent with the model of Campbell and Cheetham [18]. This model is strictly empirical and not derived from 'ghost' peaks in difference-Fourier maps or from diffuse scattering contributions.

The puckered (100) sheets of faultless mordenite consist of 6-membered rings where half of the tetrahedral apices point upwards and half point downwards. This tetrahedral conformation allows the construction of a three-dimensional zeolite framework by bonding the 4-membered rings to the (100) sheets (Fig. 3.10). Domain B is now introduced by shifting the overlying 4-membered rings by $c/2$. However, to enable strain-free linkage of the shifted pillars, the puckered (100) sheet has to be reconstructed. The relevant tetrahedra are tilted so that the upwards-pointing apices form a new connection and two new apices are free for bonding to the 4-member rings of domain B (Fig. 3.11). The new defect layer linking domain A and B consists of three edge-sharing four-member rings flanked by a strongly compressed 12-membered ring forming rows along b (Fig. 3.12). The defect interface does not affect the large 12MRc tubes. This is of great importance because these channels provide the catalytic properties of mordenite.

3.4.6 Diffuse scattering

Our observations of diffuse scattering correspond very well with the electron diffraction results from Sherman and Bennett [16] and Sanders [17]. Even if we were not able to measure (point detector) the diffuse scattering for the natural crystal, it is clear that this is a common feature also for the natural mordenite investigated. The scattering in the synthetic mordenite is concentrated around points with $h + k = 2n$ and appears only if $l = 2n + 1$. Instead of continuous streaks in the $h0l$ section or odd and even maxima, we only observed streaks with distinct maxima at odd h values. These intensities may not be interpreted as $Cmcm$ space group violating reflections but are traces of the diffuse halos around specific reflections in adjacent layers (Figs. 3.6 - 3.9). All observations of diffuse scattering described in the literature and in this

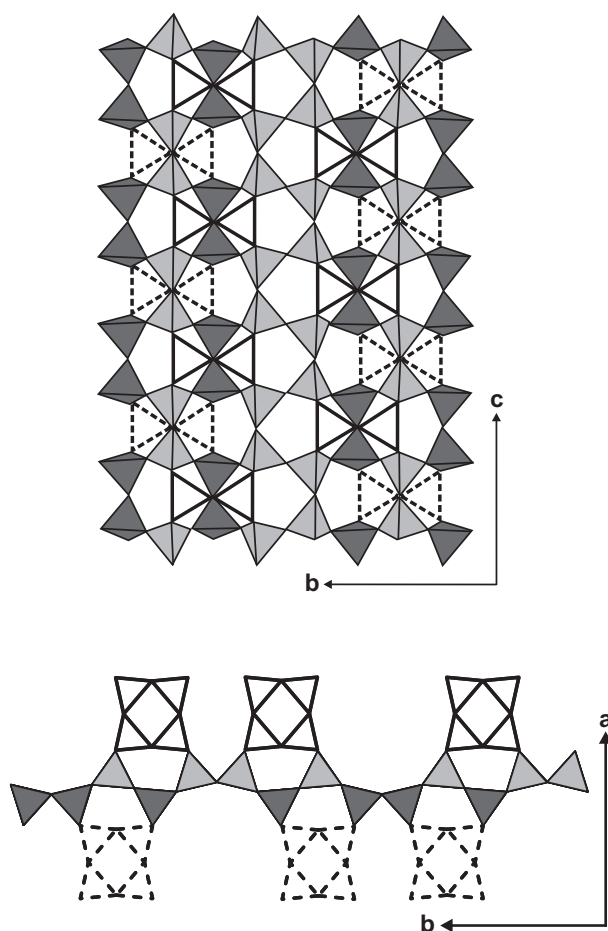


Figure 3.10: A) The pucker (100) sheet formed by 6-membered rings of tetrahedra in faultless mordenite is viewed down a . Light gray tetrahedra point upwards, dark gray tetrahedra point downwards. Triangles with full lines represent overlying 4-membered rings (seen edge-wise), dotted lines the underlying ones. B). The same (100) sheet with adjacent 4-membered rings projected down c . Downwards pointing tetrahedra bond to underlying rings (at $z = 0$), upwards pointing tetrahedra bond to overlying rings (at $z = 1/2$).

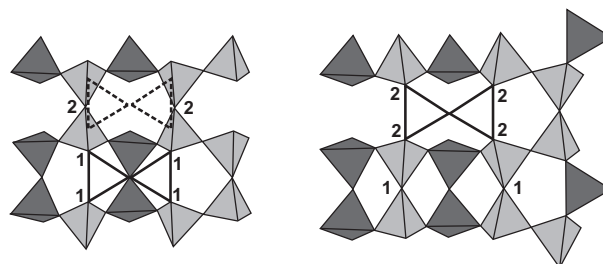


Figure 3.11: Detailed view of the (100) sheet (compare with Fig 3.10). Left: Triangles with solid outlines show the position of the overlying not shifted 4-member rings. Dotted lines represent the $c/2$ shifted positions of 4-membered rings belonging to domain B. Numbers (1, 2) indicate tetrahedral apices which need to be rearranged to allow bonding to the $c/2$ shifted 4-membered ring pillars. Right: Breaking of bonds between upwards pointing apices and a 4-membered ring (1) and disrupting a connection of two adjacent upwards pointing apices (2). New linkage of the two apices labelled (1) and new bonding of the apices labelled (2) to the 4-membered rings of the overlying domain B.

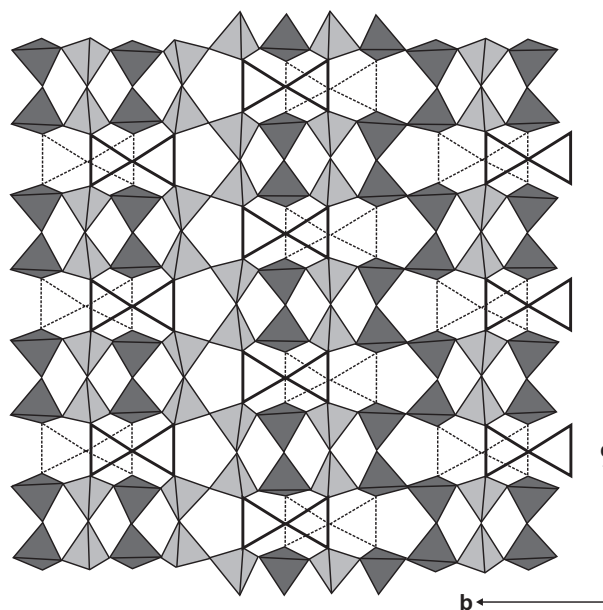


Figure 3.12: (100) defect layer projected down a . Light gray tetrahedra are pointing upwards, dark gray ones point downwards. Solid lines mark the position of the 4-membered rings (seen edge-wise) belonging to the overlying domain B. The entire overlying B domain is shifted $c/2$ relative to the underlying A domain. Fine dotted lines show the underlying 4-membered rings of domain A. Three 4-membered rings are flanked by compressed 12-membered rings forming rows along b .

study are consistent with structural $c/2$ defects. For correlated $c/2$ shifts Campbell and Cheetham [18] have developed a strongly simplified model where the defect concentration (p_0) is related to the average diffuse intensity in $l = 2n + 1$ layers by a factor of $4p_0(1-p_0)$ whereas the intensity of the Bragg reflections in the corresponding layers decreases by $(1-2p_0)^2$. However, the diffuse intensity is not homogeneous in $l = 2n + 1$ layers but enhanced in form of halos around specific reflections which are mainly related to the size and spatial correlation of the $c/2$ shifted domains. No attempts have yet been made for a quantitative interpretation of the diffuse scattering features (e.g. [39]) in mordenite.

3.4.7 Open questions

After we demonstrated in this study that two mordenite crystals with tetrahedral Al concentrations of 16 (natural) and 12.5% (synthetic), respectively, have both $c/2$ shifted B domain defect concentrations of only ca. 3%, the concentration of B domains derived from powder Rietveld refinements [14, 18] can not be used as an indicator for the framework Al concentration. Other parameters related to the concentration of this type of defect have to be considered. Natural mordenites (small port) and the synthetic mordenite (large port) investigated by us show the same qualitative diffuse scattering features and $c/2$ defects. It remains enigmatic why natural mordenites show small port behavior. Although $c/2$ defects are expected to cause diffuse scattering within reciprocal layers with $l = 2n + 1$, the inhomogeneous distribution of diffuse scattering has not yet been interpreted on a quantitative level. Thus the size and the spatial correlation of the intercalated B domains remain unknown. The true symmetry of mordenite [1, 11] remains controversial. Due to the strong $Cmcm$ pseudosymmetry of the average structure we can neither reject nor support the microtwin model of Gramlich-Meier [11].

3.5 Crystallographic data

Table 3.3 - 3.4: Atomic coordinates and B_{eq} values for natural mordenite from Jarbridge, Nevada. Refinement in space group $Cmc2_1$ with all framework positions constrained to $Cmcm$ symmetry. All atomic positions labeled B are fully constrained and belong to a domain of mordenite shifted $c/2$ relative to the main part of the structure.

Starred atoms with standard deviation were refined isotropically, those without standard deviations were fixed. Anisotropically refined atoms are given in the form of the isotropic equivalent thermal parameter defined as $B_{eq} = 8/3 \pi^2 \sum_i (\sum_j (U_{ij} a_i^* a_j^* a_i \cdot a_j))$

Table 3.5 - 3.6: Atomic coordinates and B_{eq} values for synthetic mordenite-Na.. Refinement in space group $Cmc2_1$ with all framework positions constrained to $Cmcm$ symmetry. All atomic positions labeled B are fully constrained and belong to a domain of mordenite shifted $c/2$ relative to the main part of the structure .

Starred atoms with standard deviation were refined isotropically, those without standard deviations were fixed. Anisotropically refined atoms are given in the form of the isotropic equivalent thermal parameter defined as $B_{eq} = 8/3 \pi^2 \sum_i (\sum_j (U_{ij} a_i^* a_j^* a_i \cdot a_j))$

Table 3.7 and 3.8: T-O distances (\AA) and T-O-T angles ($^\circ$) of natural mordenite and synthetic mordenite-Na, uncorrected T-O distances with standard deviations in parentheses and T-O distances corrected for riding motion [30] in brackets. Al% is estimated from the relationship by Jones [29]. Norm. refers to the Al% [29] normalized to the analyzed Al bulk composition.

Table 3.9 and 3.10: Anisotropic displacement parameters U_{ij} of natural mordenite and synthetic mordenite-Na

Atom	Population	x	y	z	B_{eq} [\AA^2]
T1	0.973(2)	0.30126(4)	0.07249(4)	0.0419(1)	1.18(1)
T1'	0.973(2)	-0.30126(4)	-0.07249(4)	-0.0419(1)	1.18(1)
T2	0.973(2)	0.30343(4)	0.30905(4)	0.0457(1)	1.32(1)
T2'	0.973(2)	-0.30343(4)	-0.30905(4)	-0.0457(1)	1.32(1)
T3	0.973(2)	0.08719(6)	0.38323(5)	1/4	1.07(2)
T4	0.973(2)	0.08636(6)	0.22720(5)	1/4	1.14(2)
O1	0.973(2)	0.1239(1)	0.4161(1)	0.4290(3)	2.83(5)
O1'	0.973(2)	-0.1239(1)	-0.4161(1)	-0.4290(3)	2.83(5)
O2	0.973(2)	0.1228(1)	0.1941(1)	0.4268(3)	2.91(4)
O2'	0.973(2)	-0.1228(1)	-0.1941(1)	-0.4268(3)	2.91(4)
O3	0.973(2)	0.2372(2)	0.1227(1)	0.9858(4)	3.54(5)
O3'	0.973(2)	-0.2372(2)	-0.1227(1)	-0.9858(4)	3.54(5)
O4	0.973(2)	0.0976(2)	0.3048(2)	0.232(3)	2.7(1)
O5	0.973(2)	0.1698(2)	0.1949(2)	3/4	3.33(8)
O6	0.973(2)	0.1777(2)	0.4203(2)	3/4	2.65(6)
O7	0.973(2)	0.2686(2)	0	0	2.42(6)
O8a	0.25	0.2401(8)	0.2597(4)	0.529(4)	1.7(1)*
O8b	0.25	-0.2401(8)	-0.2597(4)	-0.529(4)	1.7(1)*
O8b	0.25	0.245(1)	0.251(1)	0.475(4)	1.7(1)*
O8d	0.25	-0.245(1)	-0.251(1)	-0.475(4)	1.7(1)*
O9	0.973(2)	0	0.4058(2)	1/4	2.13(8)
O10	0.973(2)	0	0.2054(2)	1/4	2.50(9)
Ca (8MRc)	0.466(8)	0	1/2	1/2	4.89(9)
K1a (12MRc)	0.24(2)	0	-0.0221(4)	0.267(4)	3.4(3)*
K1b (12MRc)	0.10(2)	0	-0.021(1)	0.166(4)	2.4(7)*
Na2a (12MRc)	0.47(1)	0	0.152(1)	0.691(3)	7.9(7)*
K2b (12MRc)	0.11(2)	0	0.130(2)	0.536(6)	6.5(14)*
K3 (12MRc)	0.24(2)	0	0.188(1)	0.782(3)	6.7(6)*
W1 (8MRb)	1.0	0	0.4315(4)	0.751(4)	6.9(2)
W2 (12MRc)	0.08(4)	0.369(4)	0.492(6)	3/4	4.9(31)*
W3 (12MRc)	0.53(4)	0.3734(9)	0.529(1)	0.715(3)	6.9(7)*
W4 (12MRc)	0.80(7)	0	0.071(1)	0.064(4)	10.26(5)*
W5 (12MRc)	0.23(4)	0.091(3)	0.060(3)	-0.168(7)	9.18(4)*
W6 (8MRb)	0.52(2)	0.033(1)	0.302(1)	0.694(5)	18.2(15)*
W7 (12MRc)	0.5	0.042(2)	0.065(1)	0.465(4)	11.1(8)*
W8 (12MRc)	0.42(8)	0	0.093(3)	-0.08(1)	11.3(23)*
W9 (12MRc)	0.30(5)	-0.105(2)	0.021(3)	-0.064(8)	11.4(24)*
W10 (12MRc)	0.32(4)	0.403(3)	0.453(3)	0.82(1)	19.1(33)*

Table 3.3: Atomic coordinates and B_{eq} values for natural mordenite from Jarbridge, Nevada

Atom	Population	x	y	z	B_{eq} [\AA^2]
T1B	0.027(2)	0.30126(4)	0.07249(4)	-0.0419(1)	2.37*
T1B'	0.027(2)	-0.30126(4)	-0.07249(4)	0.0419(1)	2.37*
T2B	0.027(2)	-0.30343(4)	-0.30905(4)	0.0457(1)	2.37*
T2B'	0.027(2)	0.30343(4)	0.30905(4)	-0.0457(1)	2.37*
T3B	0.027(2)	0.08719(6)	0.38323(5)	3/4	2.37*
T4B	0.027(2)	0.08636(6)	0.22720(5)	3/4	2.37*
O1B	0.027(2)	0.1239(1)	0.4161(1)	-0.4290(3)	2.37*
O1B'	0.027(2)	-0.1239(1)	-0.4161(1)	0.4290(3)	2.37*
O2B	0.027(2)	0.1228(1)	0.1941(1)	-0.4268(3)	2.37*
O2B'	0.027(2)	-0.1228(1)	-0.1941(1)	0.4268(3)	2.37*
O3B	0.027(2)	0.2372(2)	0.1227(1)	-0.9858(4)	2.37*
O3B'	0.027(2)	-0.2372(2)	-0.1227(1)	0.9858(4)	2.37*
O4B	0.027(2)	0.0976(2)	0.3048(2)	-0.232(3)	2.37*
O5B	0.027(2)	0.1698(2)	0.1949(2)	1/4	2.37*
O6B	0.027(2)	0.1777(2)	0.4203(2)	1/4	2.37*
O7B	0.027(2)	0.2686(2)	0	1/2	2.37*
O9B	0.027(2)	0	0.4058(2)	3/4	2.37*
O10B	0.027(2)	0	0.2054(2)	3/4	2.37*

Table 3.4: Atomic coordinates and B_{eq} values for natural mordenite from Jarbridge, Nevada; continued

Atom	Population	x	y	z	B_{eq} [\AA^2]
T1	0.968(1)	0.30243(2)	0.07270(2)	0.04241(5)	1.106(6)
T1'	0.968(1)	-0.30243(2)	-0.07270(2)	-0.04241(5)	1.106(6)
T2	0.968(1)	0.30335(2)	0.30941(2)	0.04531(5)	1.158(6)
T2'	0.968(1)	-0.30335(2)	-0.30941(2)	-0.04531(5)	1.158(6)
T3	0.968(1)	0.08689(3)	0.38261(2)	1/4	0.955(7)
T4	0.968(1)	0.08638(3)	0.22709(2)	1/4	0.990(7)
O1	0.968(1)	0.12280(8)	0.41515(8)	0.4284(2)	2.82(2)
O1'	0.968(1)	-0.12280(8)	-0.41515(8)	-0.4284(2)	2.82(2)
O2	0.968(1)	0.12248(8)	0.19422(7)	0.4266(2)	2.54(2)
O2'	0.968(1)	-0.12248(8)	-0.19422(7)	-0.4266(2)	2.54(2)
O3	0.968(1)	-0.23715(9)	-0.12207(7)	-0.9887(2)	3.44(3)
O3'	0.968(1)	0.23715(9)	0.12207(7)	0.9887(2)	3.44(3)
O4	0.968(1)	0.0983(1)	0.30462(9)	0.248(1)	3.29(5)
O5	0.968(1)	0.1700(1)	0.1937(1)	3/4	3.17(4)
O6	0.968(1)	0.1750(1)	0.4205(1)	3/4	2.46(3)
O7	0.968(1)	0.2708(1)	0	0	2.39(3)
O8a	0.25	0.2401(6)	0.2602(4)	0.532(1)	1.66(6)*
O8b	0.25	-0.2401(6)	-0.2602(4)	-0.532(1)	1.66(6)*
O8c	0.25	0.2446(5)	0.2521(5)	0.480(1)	1.66(6)*
O8d	0.25	-0.2446(5)	-0.2521(5)	-0.480(1)	1.66(6)*
O9	0.968(1)	0	0.4034(1)	1/4	2.24(4)
O10	0.968(1)	0	0.2069(1)	1/4	2.24(4)
Na1 (8MRc)	0.290(5)	0.0118(2)	-0.5073(2)	0.5104(8)	2.3(1)*
Na2 (12MRc)	0.09(1)	0	0.008(1)	-0.229(4)	3.3(6)*
Na3 (12MRc)	0.26(2)	0	0.201(2)	0.774(6)	9.87*
Na4a (12MRc)	0.21(2)	0	0.072(2)	0.495(8)	9.87*
Na4b (12MRc)	0.23(2)	0	0.080(2)	0.019(7)	9.87*
W1 (8MRb)	1.0	0	0.4344(3)	0.754(2)	6.2(1)
W2 (12MRc)	0.31(1)	0.128(1)	-0.0151(9)	0.222(3)	7.90*
W3 (12MRc)	0.40(3)	1/2	0.332(2)	0.269(5)	7.90*
W4 (12MRc)	0.22(1)	0.111(1)	-0.019(1)	0.018(5)	7.90*
W5 (12MRc)	0.27(1)	0.103(1)	-0.040(1)	0.354(3)	7.90*
W6 (8MRb)	0.32(2)	1/2	0.223(1)	0.302(4)	7.90*
W7 (12MRc)	0.22(2)	1/2	0.383(2)	0.379(7)	7.90*
W8 (8MRb)	0.24(1)	0.455(1)	0.190(1)	0.195(3)	7.90*
W9 (12MRc)	0.20(2)	1/2	0.321(3)	0.128(8)	7.90*
W10 (12MRc)	0.18(2)	1/2	0.447(2)	-0.205(7)	7.90*
W11 (12MRc)	0.46(3)	1/2	0.388(1)	0.017(4)	7.90*

Table 3.5: Atomic coordinates and B_{eq} values for synthetic mordenite-Na

Atom	Population	x	y	z	B_{eq} , [\AA^2]
T1B	0.032(1)	0.30243(2)	0.07270(2)	-0.04241(5)	2.37*
T1B'	0.032(1)	-0.30243(2)	-0.07270(2)	0.04241(5)	2.37*
T2B	0.032(1)	-0.30335(2)	-0.30941(2)	0.04531(5)	2.37*
T2B'	0.032(1)	0.30335(2)	0.30941(2)	-0.04531(5)	2.37*
T3B	0.032(1)	0.08689(3)	0.38261(2)	3/4	2.37*
T4B	0.032(1)	0.08638(3)	0.22709(2)	3/4	2.37*
O1B	0.032(1)	0.12280(8)	0.41515(8)	-0.4284(2)	2.37*
O1B'	0.032(1)	-0.12280(8)	-0.41515(8)	0.4284(2)	2.37*
O2B	0.032(1)	0.12248(8)	0.19422(7)	-0.4266(2)	2.37*
O2B'	0.032(1)	-0.12248(8)	-0.19422(7)	0.4266(2)	2.37*
O3B	0.032(1)	-0.23715(9)	-0.12207(7)	0.9887(2)	2.37*
O3B'	0.032(1)	0.23715(9)	0.12207(7)	-0.9887(2)	2.37*
O4B	0.032(1)	0.0983(1)	0.30462(9)	-0.248(1)	2.37*
O5B	0.032(1)	0.1700(1)	0.1937(1)	1/4	2.37*
O6B	0.032(1)	0.1750(1)	0.4205(1)	1/4	2.37*
O7B	0.032(1)	0.2708(1)	0	1/2	2.37*
O9B	0.032(1)	0	0.4034(1)	3/4	2.37*
O10B	0.032(1)	0	0.2069(1)	3/4	2.37*

Table 3.6: Atomic coordinates and B_{eq} values for synthetic mordenite-Na; continued

Bond	(Å)	(corr.)	Al%	Bond	(Å)	(corr.)	Al%
T1 - O1	1.616(2)	[1.634]		T2 - O2	1.608(2)	[1.625]	
T1 - O3'	1.605(3)	[1.631]		T2 - O5	1.612(1)	[1.630]	
T1 - O6	1.616(1)	[1.633]		T2 - O8ave	1.61(1)		
T1 - O7	1.628(1)	[1.641]		T2 - O3	1.597(2)	[1.622]	
average	1.616	[1.635]	7.9	average	1.606	[1.621]	1.5
			Norm. 14				Norm. 3
T3 - O1	1.644(2)	[1.663]		T4 - O2	1.631(2)	[1.650]	
T3 - O4	1.622(4)	[1.640]		T4 - O4	1.608(4)	[1.626]	
T3 - O9	1.644(2)	[1.655]		T4 - O10	1.625(2)	[1.639]	
T3 - O1'	1.644(2)	[1.663]		T4 - O2'	1.631(2)	[1.650]	
average	1.639	[1.656]	22.7	average	1.624	[1.641]	13.0
			Norm. 41				Norm. 24
<hr/>							
T - O - T	(°)			T - O - T	(°)		
T1-O1-T3	145.83(18)			T2-O2-T4	143.58(17)		
T1'-O3-T2	158.1(2)			T3-O4-T4	163.0(8)		
T2-O5-T2'	144.5(3)			T1-O6-T1'	150.8(3)		
T1-O7-T1'	137.4(2)			T2-O8A/C-T2'	155(1) / 165(1)		
T3-O9-T3	147.4(3)			T4-O10-T4	148.2(3)		

Table 3.7: T-O distances (Å) and T-O-T angles (°) of natural mordenite

Bond	(Å)	(corr.)	Al%	Bond	(Å)	(corr.)	Al%
T1 - O1	1.6232(13)	[1.642]		T2 - O2	1.6160(14)	[1.631]	
T1 - O3'	1.6092(14)	[1.636]		T2 - O5	1.6148(8)	[1.635]	
T1 - O6	1.6203(6)	[1.636]		T2 - O8ave.	1.6184(6)		
T1 - O7	1.6291(8)	[1.643]		T2 - O3	1.6060(13)	[1.632]	
average	1.620	[1.639]	10.5	average	1.614	[1.629]	6.6
			Norm. 13				Norm. 8
T3 - O1	1.6343(13)	[1.655]		T4 - O2	1.6269(13)	[1.644]	
T3 - O4	1.6124(19)	[1.640]		T4 - O4	1.6047(19)	[1.631]	
T3 - O9	1.6319(9)	[1.646]		T4 - O10	1.6202(9)	[1.634]	
T3 - O1'	1.6343(13)	[1.655]		T4 - O2'	1.6269(13)	[1.644]	
average	1.628	[1.649]	15.6	average	1.620	[1.638]	10.5
			Norm. 20				Norm. 13

T - O - T	(°)	T - O - T	(°)
T1-O1-T3	146.01(11)	T2-O2-T4	143.61 (10)
T1'-O3-T2	157.95(13)	T3-O4-T4	164.82(16)
T2-O5-T2'	144.92(15)	T1-O6-T1'	149.04 (14)
T1-O7-T1'	138.72(12)	T2-O8A/C-T2'	154.2(9) / 166.7(4)
T3-O9-T3	149.74(18)	T4-O10-T4	150.33(19)

Table 3.8: T-O distances (Å) and T-O-T angles (°) of synthetic mordenite-Na

Atom	U_{11}	U_{22}	U_{33}	U_{12}	U_{13}	U_{23}
T1	0.0192(4)	0.0154(3)	0.0103(3)	0.0018(3)	0.0018(3)	0.0008(3)
T1'	0.0192(4)	0.0154(3)	0.0103(3)	0.0018(3)	0.0018(3)	0.0008(3)
T2	0.0208(4)	0.0172(3)	0.0121(4)	0.0037(4)	0.0012(3)	-0.0013(3)
T2'	0.0208(4)	0.0172(3)	0.0121(4)	0.0037(4)	0.0012(3)	-0.0013(3)
T3	0.0117(5)	0.0158(5)	0.0132(5)	-0.0017(4)	0	0
T4	0.0119(5)	0.0162(5)	0.0153(5)	0.0013(4)	0	0
O1	0.030(1)	0.055(2)	0.023(1)	-0.007(1)	-0.008(1)	-0.006(1)
O1'	0.030(1)	0.055(2)	0.023(1)	-0.007(1)	-0.008(1)	-0.006(1)
O2	0.032(1)	0.051(1)	0.028(1)	0.000(1)	-0.009(1)	0.010(1)
O2'	0.032(1)	0.051(1)	0.028(1)	0.000(1)	-0.009(1)	0.010(1)
O3	0.052(2)	0.035(1)	0.047(2)	0.021(1)	-0.006(1)	0.005(1)
O3'	0.052(2)	0.035(1)	0.047(2)	0.021(1)	-0.006(1)	0.005(1)
O4	0.036(2)	0.019(1)	0.048(7)	-0.002(2)	0.011(4)	0.001(4)
O5	0.052(2)	0.057(2)	0.016(2)	0.017(2)	-0.020(6)	0.008(8)
O6	0.045(2)	0.042(2)	0.013(1)	-0.008(2)	0	0
O7	0.033(2)	0.021(1)	0.038(2)	0	0	-0.005(1)
O9	0.015(2)	0.030(2)	0.036(3)	0	0	-0.01(1)
O10	0.019(2)	0.029(3)	0.047(3)	0	0	0
Ca	0.056(3)	0.065(3)	0.065(3)	0	0	-0.037(2)
W1	0.050(4)	0.080(5)	0.133(9)	0	0	-0.05(1)

Table 3.9: Anisotropic displacement parameters U_{ij} of natural mordenite

Atom	U_{11}	U_{22}	U_{33}	U_{12}	U_{13}	U_{23}
T1	0.0187(2)	0.0126(2)	0.0107(2)	0.0017(1)	0.0017(1)	0.0013(1)
T1'	0.0187(2)	0.0126(2)	0.0107(2)	0.0017(1)	0.0017(1)	0.0013(1)
T2	0.0174(2)	0.0149(2)	0.0117(2)	0.0033(1)	0.0007(1)	-0.0011(1)
T2'	0.0174(2)	0.0149(2)	0.0117(2)	0.0033(1)	0.0007(1)	-0.0011(1)
T3	0.0108(2)	0.0132(2)	0.0123(2)	-0.0016(2)	0	0
T4	0.0102(2)	0.0130(2)	0.0145(2)	0.0012(2)	0	0
O1	0.0305(6)	0.0523(8)	0.0242(5)	-0.0086(6)	-0.0094(5)	-0.0072(5)
O1'	0.0305(6)	0.0523(8)	0.0242(5)	-0.0086(6)	-0.0094(5)	-0.0072(5)
O2	0.0282(6)	0.0432(8)	0.0252(6)	-0.0023(5)	-0.0093(5)	0.0087(5)
O2'	0.0282(6)	0.0432(8)	0.0252(6)	-0.0023(5)	-0.0093(5)	0.0087(5)
O3	0.0502(9)	0.0332(7)	0.0472(8)	0.0229(6)	-0.0072(7)	0.0063(6)
O3'	0.0502(9)	0.0332(7)	0.0472(8)	0.0229(6)	-0.0072(7)	0.0063(6)
O4	0.035(1)	0.0146(8)	0.076(2)	0.0030(7)	0.021(3)	0.017(2)
O5	0.044(1)	0.061(2)	0.0150(8)	0.019(1)	-0.016(2)	-0.017(2)
O6	0.040(1)	0.041(1)	0.0118(6)	-0.0071(8)	0	0
O7	0.0333(9)	0.0193(7)	0.0382(9)	0	0	-0.0061(7)
O9	0.0149(9)	0.033(1)	0.038(1)	0	0	0.019(3)
O10	0.0127(9)	0.031(1)	0.042(1)	0	0	0
W1	0.062(3)	0.097(4)	0.078(4)	0	0	-0.042(6)

Table 3.10: Anisotropic displacement parameters U_{ij} of synthetic mordenite-Na

Bibliography

- [1] W.M. Meier, “The crystal structure of mordenite”, *Zeit. Kristallogr.*, Vol. 115, p. 439–450, 1961.
- [2] W.M. Meier, *Natural Zeolites: Occurrence, Properties, Use*, Chapter Constituent Sheets in the Zeolite Frameworks of the Mordenite Group, p. 99–103, Pergamon Press, 1978.
- [3] T. Armbruster and M.E. Gunter, *Natural Zeolites: Occurrence, Properties, Applications*, Vol. 45 of *Reviews in Mineralogy and Geochemistry*, Chapter Crystal Structure of Natural Zeolites, p. 1–67, Mineralogical Society of America, 2002.
- [4] O. Terasaki, K. Yamazaki, J.M. Thomas, T. Ohsuna, D. Watanabe, and J.V. Sanders, “The incorporation of selenium into the channels of mordenite: An electron microscopic study”, *J. Solid State Chem.*, Vol. 77, p. 72–83, 1988.
- [5] R. Lilis, “Fibrous zeolites and endemic mesothelioma in Cappadocia, Turkey”, *J. Occupat. Medic.*, Vol. 23, p. 548–550, 1981.
- [6] D.J. Stephenson, C.I. Fairchild, R.M. Buchan, and M.E. Dakins, “A fiber characterization of natural zeolite mordenite: A potential inhalation health-hazard”, *Aerosol Sci. Tech.*, Vol. 30, p. 467–476, 1999.
- [7] L.B. Sand, “Synthesis of large-port and small-port mordenites”, in *Molecular Sieves*, 1968, Papers of Conference, Meeting Date 1967, p. 71–77.
- [8] F. Raatz, C. Marcilly, and E. Freund, “Comparison between small-port and large-port mordenites”, *Zeolites*, Vol. 5, p. 329–333, 1985.

- [9] F. Hamidi, M. Pamba, A. Bengueddach, F. di Renzo, and F. Faujula, “Factors affecting composition and morphology of mordenite”, in *Zeolites and Mesoporous Materials at the Dawn of the 21st century*, A. Galarnau, F. di Renzo, F. Faujula, and J. Verdine, Eds., 2001, Vol. 135 of *Studies in Surface Science and Catalysis*, p. 334.
- [10] T. Sano, S. Wakabayashi, Y. Oumi, and T. Uozumi, “Synthesis of large mordenite crystals in the presence of aliphatic alcohol”, *Microporous Mesoporous Materials*, Vol. 46, p. 67–74, 2001.
- [11] R. Gramlich-Meier, *Strukturparameter in Zeolithen der Mordenitefamilie*, Dissertation, ETH Zurich, Nr. 6760, 1981.
- [12] A. Alberti, P. Davoli, and G. Vezzalini, “The crystal structure refinement of a natural mordenite”, *Zeit. Kristallogr.*, Vol. 175, p. 249–256, 1986.
- [13] K. Shiokawa, M. Ito, and K. Itabashi, “Crystal structure of synthetic mordenite”, *Zeolites*, Vol. 9, p. 170–176, 1989.
- [14] P.R. Rudolf and J.M. Graces, “Rietveld refinement of several structural models for mordenite that account for differences in X-ray powder pattern”, *Zeolites*, Vol. 14, p. 137–146, 1994.
- [15] I.S. Kerr, “Possible structures related to mordenite”, *Nature*, Vol. 197, p. 1194–1195, 1963.
- [16] J.D. Sherman and J.M. Bennett, “Framework structures related to the zeolites mordenite”, in *Molecular Sieves*, 1968, Papers of Conference, Meeting Date 1967, p. 53–65.
- [17] J.V Sanders, “Crystallographic faulting in the mordenite group zeolites”, *Zeolites*, Vol. 5, p. 81–89, 1985.
- [18] B.J. Campbell and A.K. Cheetham, “Linear framework defects in zeolite mordenite”, *J. Phys. Chem. B.*, Vol. 106, p. 57–62, 2002.
- [19] S.G. Song, “Crystal defects of mordenite crystals”, *J. Mater. Res.*, Vol. 14, p. 2616–2620, 1999.

- [20] J. Warzywoda, A.G. Dixon, R.W. Thompson, and A.Jr. Sacco, “Synthesis and control of the size of large mordenite crystals using porous silica substrates”, *J. Mater. Chem.*, Vol. 5, No. 7, p. 1019–1025, 1995.
- [21] J. Warzywoda, A.G. Dixon, R.W. Thompson, A.Jr. Sacco, and S.L. Suib, “The role of the dissolution of silicic acid powders in aluminosilicate synthesis mixtures in the crystallization of large mordenite single crystal”, *Zeolites*, Vol. 16, p. 125–137, 1996.
- [22] G. Calzaferri, D. Brühwiler, D. Megelski, M. Pfenniger, M. Pauchard, B. Hennessy, H. Maas, A. Devaux, and U. Graf, “Playing with dye molecules at the inner and outer surface of zeolite L”, *Solid State Sci.*, Vol. 2, p. 421–447, 2000.
- [23] P. Simoncic and T. Armbruster, “Synthesis of mordenite single crystals for dye incorporation”, in *Zeolites '02, International Conference on the Occurrence, Properties and Utilization of Natural Zeolites*, P. Misaelides, Ed., 2002, Vol. Book of Abstracts, p. 336.
- [24] Enraf Nonius, *Structure Determination Package (SDP)*, Enraf Nonius, Delft, Netherlands, 1983.
- [25] Oxford Diffraction, *CrysAlis Software Package 1.169, User Manual*, Xcalibur System, Oxfordshire, UK, 2001.
- [26] G.M. Sheldrik, *ShelX-97*, University of Göttingen, Germany, 1997.
- [27] W.J. Mortier, J.J. Pluth, and J.V. Smith, “Positions of cations and molecules in zeolite with the mordenite-type framework: II Dehydrated hydrogen-ptilolite”, *Mater. Res. Bull.*, Vol. 10, p. 1319–1326, 1975.
- [28] A. Alberti and G. Gottardi, “The determination of the Al-content in the tetrahedra of framework silicates”, *Zeit. Kristallogr.*, Vol. 184, p. 49–61, 1988.
- [29] J.B. Jones, “Al-O and Si-O tetrahedral distances in aluminosilicate framework structures”, *Acta Cryst. B*, Vol. 24, p. 335–358, 1968.

- [30] C.K. Johnson, *Crystallographic Computing*, Chapter The Effect of Thermal Motion on Interatomic Distances and Angles, p. 220–226, Munksgaard, Copenhagen, 1970.
- [31] A. Alberti, “Location of Bronsted sites in mordenite”, *Zeolites*, Vol. 19, p. 411–415, 1997.
- [32] E. Passaglia, “The crystal chemistry of mordenite”, *Contrib. Mineral. Petr.*, Vol. 50, p. 65–77, 1975.
- [33] M. Ito and Y. Saito, “The crystal structure of ion-exchanged mordenite”, *Bull. Chem. Soc. Jap.*, Vol. 58, p. 3035–3036, 1985.
- [34] M. Akizuki, Y. Kudoh, and S. Nakamura, “Growth texture and symmetry of heulandite-Ca from Poona, India”, *Can. Mineralogist*, Vol. 37, p. 1307–1312, 1999.
- [35] Y.I. Tarasevich, D.A. Krysenko, and V.E. Polyakov, “Selectivity of low- and high-silica clinoptilolites with respect to alkali and alkaline earth metal cations”, *Colloid J.*, Vol. 64, p. 759–764, 2002.
- [36] W.M. Meier, R. Meier, and V. Gramlich, “Mordenite: Interpretation of a superposed structure”, *Zeit. Kristallogr.*, Vol. 147, p. 329, 1978.
- [37] W.J. Mortier, J.J. Pluth, and J.V. Smith, *Natural Zeolites: Occurrence, Properties, Use*, Chapter Positions of Cations and Molecules in Zeolites with the Mordenite-Type Framework. IV. Dehydrated and Rehydrated K-exchanged ‘Ptilolite’, p. 53–75, Pergamon Press, 1978.
- [38] K. Itabashi, T. Fukushima, and K. Igawa, “Synthesis and characteristic properties of siliceous mordenite”, *Zeolites*, Vol. 6, p. 30–34, 1986.
- [39] T. Weber and H.B. Bürgi, “Determination of disordered crystal structures using evolutionary algorithms in combination with Monte Carlo methods”, *Acta Cryst. A*, Vol. 58, p. 526–540, 2002.

4 Se Incorporated into Zeolite Mordenite-Na: A Single-Crystal X-ray Study ¹

Petra Simoncic and Thomas Armbruster

Abstract

Single crystals of self-synthesized mordenite-Na were used for incorporation of elemental selenium. The mordenite sample was first dehydrated at 280 °C and selenium was subsequently incorporated as gas-phase at 450 °C for 72 h. Bright orange-coloured Se-loaded mordenite was quantitatively analysed by an electron-microprobe yielding $\text{Na}_6\text{Al}_{6.02}\text{Si}_{42.02}\text{O}_{96} \times [\text{Se}_{7.9}]$. X-ray data collection of mordenite-Na and Se-loaded mordenite-Na single-crystals were performed at 120 K with synchrotron radiation ($\lambda = 0.79946 \text{ \AA}$) using the single-crystal diffraction line at SNBL (ESRF, Grenoble) where diffracted intensities were registered with a MAR image plate. The structures of mordenite-Na and Se-mordenite-Na were both refined in the monoclinic space group Cc converging at $R_1 = 5.25\%$ (mordenite-Na), and $R_1 = 6.65\%$ (Se-mordenite-Na). A strongly broadened Raman band at ca. 254 cm^{-1} confirmed the existence of Se chains in the 12-membered channels along the c -axis. Several, low-populated, disordered Se chains with a length up to 10 \AA and 7 Se atoms were located in the large mordenite channels. During structure refinement nearest and next nearest neighbor Se-Se distances were fixed at 2.34 \AA and 3.62 \AA , respectively. Other distances and angles remained unconstrained. Because of electrostatic interaction with the framework and influence of extraframework occupants such as Na^+ and H_2O molecules, the chains show different geometrical Se arrangement with highly variable dihedral angles. Any other Se species such as Se_6 or Se_8 rings were neither confirmed by structure refinement nor by Raman spectroscopy. There was no indication of a trigonal Se chain geometry within the 12-membered ring channel.

¹Lab. für chem. and mineral. Kristallographie. "Microporous Mesoporous Materials, Vol.71, p. 185-189, 2004

4.1 Introduction

Microporous materials as zeolites are more and more applied for the design and development of new materials. With their channels and cavities of several angstroms in size, they allow a spatial arrangement and stabilization of individual atoms, clusters or molecules. One aspect of modern technology and new materials are one-dimensional systems and miniaturized electronic devices with fast response, high selectivity and efficiency, e.g. semiconductors organized as quantum dots or chains in zeolites channels. Semiconductor materials were encapsulated in synthetic zeolites such as $\text{AlPO}_4\text{-5}$, zeolites A, and Y [1–3] with their uniform and large channels ($> 7 \text{ \AA}$), but also the naturally occurring mordenite with its compressed channels ($7 \times 6.5 \text{ \AA}$) was successfully used for molecular organization of atoms and molecules. The structure of mordenite can be described as built by edge-sharing 5-membered rings of tetrahedra (secondary building unit 5-1) forming chains along the c -axis [4]. However, the mordenite framework can also be more comprehensibly envisioned as formed by puckered sheets parallel to (100), assembled of six-membered rings of tetrahedra [5, 6]. These sheets are interlinked by four-membered rings (Fig. 4.1) in a way that large, ellipsoidal 12-membered (12MRc: aperture $7 \times 6.5 \text{ \AA}$) and strongly compressed 8-membered rings (8MRc: aperture $5.7 \times 2.6 \text{ \AA}$) define channels parallel to the c -axis. Another set of compressed 8-membered rings (8MRb: aperture $3.4 \times 4.8 \text{ \AA}$) connects the wide channels with the strongly compressed channels parallel to the b -axis.

Elemental selenium incorporated into zeolite mordenite is a good example of a one-dimensional semiconductor, and this host-guest system has widely been investigated. Two methods have been established for encapsulation of Se in mordenite: (1) Adsorption in gas phase and (2) molten selenium injection under pressure. Elemental selenium exists in different solid modification: two monoclinic, both characterized by Se_8 rings, a trigonal, an amorphous, and a cubic modification. The trigonal phase is the only stable phase under ambient conditions. The trigonal Se modification builds helical chains. Typical bond lengths to nearest and next nearest neighbors are $2.373(5) \text{ \AA}$, and 3.72 \AA , respectively. The Se-Se-Se bond angle is $103^\circ \pm 0.02$ [7]. The channel wall, as well as extraframework cations and H_2O molecules affect Se incorporated into mordenite. Therefore, it can be expected that the form of a helical chain will be influenced by the zeolite structure and symmetry and will be different to the trigonal helical chain

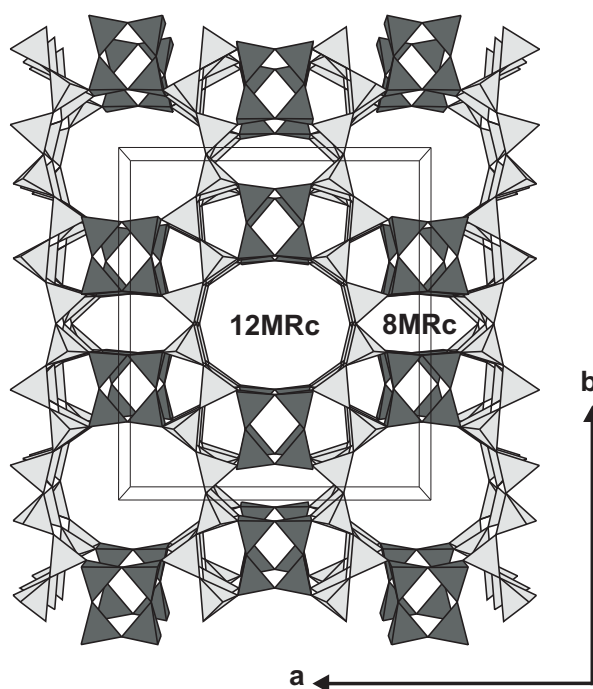


Figure 4.1: Tetrahedral framework structure of mordenite with unit-cell outlines. The structure can be envisioned as built by puckered sheets (light gray shading) parallel to (100) formed by six-membered rings of tetrahedra. These sheets are connected along a by 4-membered ring pillars (dark gray shading) in a way that 12-membered ring channels (12MRc) and compressed 8-membered ring channels (8MRc) are formed, both extending along c .

known from the Se polytype. Structure and arrangement of Se atoms in zeolites were mainly investigated by Raman spectroscopy, X-ray adsorption, EXAFS, XANES and electron microscopy where helical Se chains and their forms were verified in mordenite channels.

A slightly inclined selenium chain within the large channels of mordenite along c is composed of approximately 6 Se atoms yielding the periodicity of the mordenite c translation (7.5 Å). Thus, if the channels are completely occupied by Se chains, the maximum Se concentrations amounts to ca. 12 Se per formula unit (pfu).

First experiments concerning elemental Se in mordenite were done by Bogomolov et al. [8]. They incorporated Se and Te by gas phase as well as by injection from Se melt under pressure and reported optical density spectra of Se- and Te-mordenite. They postulated that the symmetry of the chains in the mordenite channels differs

from the symmetry of elemental Se and Te (D_3), due to variation of the dihedral angle but with constant bond length and bond angle. In a second study, Bogomolov et al. [9] compared Raman spectra of trigonal and monoclinic Se with those of Se incorporated into mordenite. They observed a clear shift of the Raman active A1 symmetric stretching mode to higher frequency for Se in mordenite. Due to similar modes in Se-mordenite compared with the symmetric bond-bending modes of Se_8 , they proposed ring- and chain-like Se fragments in the mordenite channel distinct by variation of the dihedral angle. They expected that the dihedral angle could deviate up to 30° from the preferred value of 102° .

Poborchii et al. performed series of experiments [10–15] with Se loaded in different zeolites (mordenite, cancrinite, $AlPO_4-5$) applying EXAFS and Raman spectroscopy. They discussed the influence of ion exchange and different incorporation methods of Se in mordenite on the form of the Se in the channels. Poborchii et al. [10–15] observed that Se chains are more regular if Se is incorporated by vapor adsorption. In addition to Se chains, they postulated also six-membered Se rings located in the mordenite channel. The relative concentration of rings or chains is not dependent of the incorporation method but of type of extraframework cations in mordenite. The Se chain concentration is decreasing compared to Se_6 -rings and Se-Se bond lengths increase if extraframework Na-ions are substituted by other monovalent cations. Poborchii et al. [10] discussed also the geometry of Se chains. Based on the work of Bogomolov et al. [8, 9], Poborchii derived a Se chain arrangement in the mordenite channel from stretching and bending modes of Raman spectra.

Terasaki et al. [16] performed an electron-microscopy study on synthetic H^+ -exchanged mordenite, modified with vapor-induced Se. High-resolution images showed that channels are patch-wise filled with selenium.

Based on EXAFS experiments, bond lengths and angles of Se chains in mordenite were discussed by Khouchaf et al. [17], Parise et al. [18] and Katayama et al. [19]. The nearest neighbor distance between Se atoms was determined by all groups to 2.33 Å, next nearest neighbor distance to 3.62 Å with a bond angle of 102° . Nearest and next nearest distances of Se atoms in mordenite are therefore shorter than in trigonal Se. The third neighbor distance was more difficult to determine. Khouchaf et al. [17] and Katayama et al. [19] derived from EXAFS data a corresponding distance of 4.3 Å. This distance was assumed [17] to be due to an overlap of two chains (interchain

distance), whereas Katayama et al. [19] interpreted it as an intrachain distance to the third neighbor. Thus the details of the third neighbor distance, which is crucial for the form of the Se chain in mordenite, remained unclear.

Ikawa et al. [20, 21] calculated semi-empirical models for the electronic and lattice structure of isolated Se chains in mordenite channels and discussed internal defects of Se-chains and interactions with cations, H₂O molecules, and framework oxygen. They postulated that incorporated Se is highly influenced by the zeolite host. The modeled chains show different geometries due to variation of the dihedral angle, which are distinct from the trigonal Se chains.

Whereas the existence of rings and chains in mordenite channels is confirmed by different spectroscopic methods, the exact structure of encapsulated Se has not been solved yet. In particular, the form of Se chains is controversially discussed. Single-crystal X-ray diffraction is a suitable method for investigating Se-modified mordenite. The aims of this study are: (1) Incorporation of Se in self-synthesized, large mordenite single-crystals; (2) study the location and bonding of Se in mordenite channels by single-crystal X-ray diffraction.

4.2 Experimental

4.2.1 Sample

Pure mordenite-Na crystals were synthesized hydrothermally in the home lab after a modified method by Warzywoda et al. [22]. The exact synthesis conditions are summarized in Table 3.1. The crystallization products were 100% mordenite with platy and uniform morphology. The run products were studied with a polarizing microscope and the single crystals were examined with a scanning electron microscope and showed well-defined, but slightly curved faces and no apparent twinning. Average size of the mordenite crystals was about $0.06 \times 0.04 \times 0.05$ mm (Fig. 4.2). Previous ion-exchange experiments with cationic dyes [23] showed that the used sample is a large port mordenite, and therefore suitable for incorporation of Se chains.

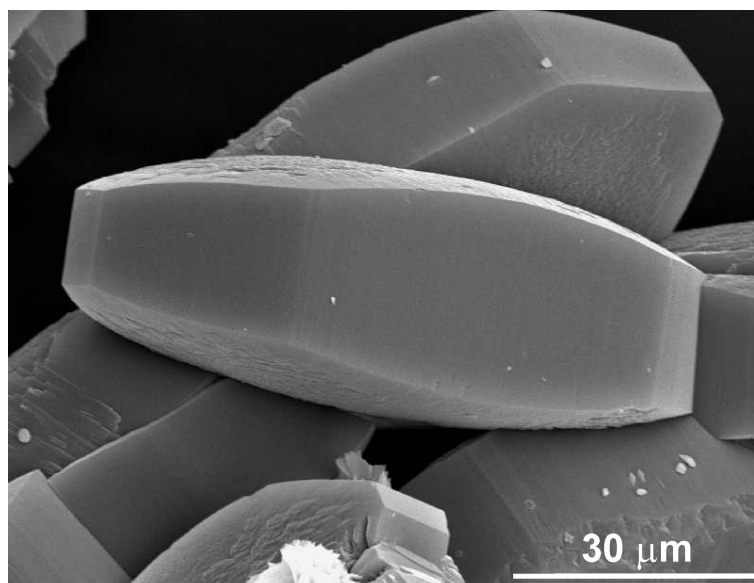


Figure 4.2: Scanning electron microscopic image of synthetic, platy mordenite of $\text{Na}_6\text{Al}_6.02\text{Si}_{42.02}\text{O}_{96} \times 19 \text{H}_2\text{O}$ composition. Notice that the (001) face is rough and slightly curved. The large channels (Figs. 4.1 and 3.2) run perpendicular to this face.

4.2.2 Selenium incorporation

Self-synthesized mordenite-Na was used for encapsulation of elemental selenium. Mordenite single-crystals (ca. 5 mg) were dehydrated at 280 °C in an open glass tube (0.3 ml, outer diameter: 5mm, wall thickness: 1mm) for 2 h. Previous thermo-gravimetric analysis (TG) showed that mordenite-Na is completely dehydrated after this treatment and no extraframework H_2O is present in mordenite-Na before Se incorporation. After dehydration the temperature was rapidly lowered to 150 °C and ca. 10 mg Se (Aldrich, 99.5 %) was added into the glass tube, which was immediately sealed. The sealed tube was subsequently heated in an oven at 450 °C for 72 h and then cooled down in the oven to room temperature. The crystals were examined under an optical microscope showing a clear pleochroism changing from orange to yellow. Successful incorporation was also confirmed by Raman spectroscopy performed on a RamSpec spectrometer using a laser with 532.12 nm wavelength attached to an optical polarizing microscope, which enables single crystal studies (Fig. 4.3).

Se-loaded mordenite was quantitatively determined by electron-microprobe analyses

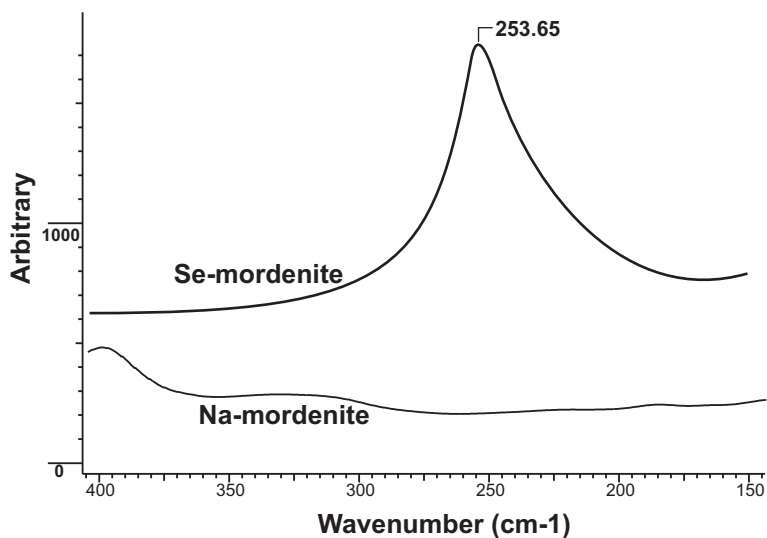


Figure 4.3: Raman spectrum from 150 to 400 cm^{-1} of Se-mordenite-Na and mordenite-Na. A dominant vibration band at 253.65 cm^{-1} in Se-mordenite-Na is absent in mordenite-Na. According to literature data [9-15], this band can be attributed to the symmetric stretching band A1 in a Se chain.

resulting in a chemical composition of $\text{Na}_6\text{Al}_{6.02}\text{Si}_{42.02}\text{O}_{96} \times [\text{Se}_{7.9}] \times n\text{H}_2\text{O}$. Electron-microprobe analysis showed also that Se is uniformly incorporated into mordenite; no zoning was detected.

4.2.3 X-ray data collection

X-ray data collection of synthetic mordenite-Na (as synthesized) and Se-treated (Se-mordenite-Na) single crystals were performed at 120 K using a conventional liquid- N_2 device with synchrotron radiation (wavelength $\lambda = 0.79946 \text{ \AA}$) on the single-crystal diffraction line at SNBL (ESRF, Grenoble) where diffracted intensities were registered with a MAR image plate. The double experiments were performed to detect possible phase transitions in the mordenite structure at low temperature due to the influence of Se incorporation. The reason for intensity data collection at low temperature was to reduce thermal vibration of extraframework Se in order to allow more accurate localization. Data reduction was performed with the program package CrysAlis [24] and an empirical absorption correction was made with Sadabs [25]. A summary of experimental parameters is given in Table 4.1.

Structure refinement for mordenite-Na and Se-mordenite-Na was carried out with

Sample	Mordenite-Na	Se-Mordenite-Na
Crystal size (mm)	0.05 × 0.04 × 0.50	0.06 × 0.04 × 0.05
Diffractionmeter	Mar image plate	Mar image plate
X-ray radiation	Synchrotron (0.7995 Å)	Synchrotron (0.7995 Å)
Temperature	120 K	120 K
Space Group	<i>Cc</i>	<i>Cc</i>
Cell dimensions (Å)	18.073(3), 20.463(3), 7.5145(9)	18.077(3), 20.509(2), 7.5172(9)
β (°)	90.05(1)	90.03(2)
Absorption corr.	Sadabs	Sadabs
Maximum 2θ	55.13	55.09
Measured reflections	15595	15670
Index range	$-20 \leq h \leq 20, -23 \leq k \leq 23, -8 \leq l \leq 8$	$-20 \leq h \leq 20, -23 \leq k \leq 23, -8 \leq l \leq 8$
Unique reflections	4468	4440
Reflections $> 4\sigma(F_o)$	4180	4212
R_{int}	0.0347	0.0355
R_σ	0.0398	0.0317
Number of l.s. parameters	362	359
GooF	1.131	1.096
$R1, F_o > 4\sigma(F_o)$	0.0525	0.0665
$R1, all\ data$	0.0573	0.0700
wR2 (on F_o^2)	0.1095	0.1517

Table 4.1: Experimental parameters for X-ray data collection and refinement of mordenite-Na and Se-mordenite-Na

the program SHELXL97 [25], using neutral-atom scattering factors (Si for all tetrahedral sites - labeled T sites). Refinements were performed with anisotropic displacement parameters for all framework sites and highly populated extraframework positions. Test refinements were carried out in space groups *Cmcm*, *Cmc2₁*, *C2/c* and *Cc*. Final data were presented in space group *Cc* for both structures. In addition, a *c/2*-shifted defect domain was introduced and fully constrained to the Si/Al framework [26]. The O8 site was split into four isotropic satellite positions, which were approximately equally occupied. Na- and H₂O positions were determined by comparison with diffraction data of synthetic mordenite at room temperature [26]. Se sites were identified by analyzing difference Fourier maps focusing on the 12-membered-ring channel of mordenite-Na and Se-mordenite-Na. Clear differences of electron density in the channels are visible (Fig. 4.4). High electron density (3-5 e/Å³) in the 12-membered channel of the Se-mordenite-Na is concentrated around the channel center, whereas only low electron density occurs in the corresponding mordenite-Na channel.

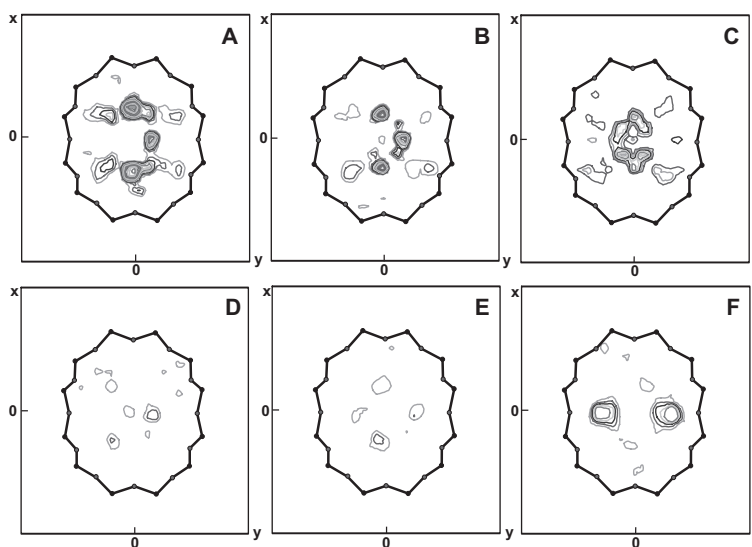


Figure 4.4: Difference Fourier maps of Se-mordenite-Na and mordenite-Na, contours at 0.25 electron intervals for all maps. Upper line Se-mordenite-Na: A) (001) section of 12-membered ring channel at $z = -0.64$: Strong peaks shifted $\pm x$ from the center of the channel, as well as one strong peak shifted $+y$ from the center. B) (001) section at $z = -0.51$: Strong peaks shifted $\pm x$ and $+y$ from the channel center. C) (001) section at $z = -0.38$: Strong, smeared electron density rhombus like around the center. Lower line: mordenite-Na: D) (001) section of 12-membered channel at $z = -0.64$ and E) (001) section at $z = -0.51$: Only weak electron density inside the channel. F) (001) section at -0.38 : Two peaks shifted $\pm y$ from the center, attributed to Na3.

4.3 Results

4.3.1 Structure refinement

The single-crystal X-ray diffraction pattern of mordenite-Na and Se-treated mordenite-Na exhibited no difference concerning diffuse scattering features. In particular, there were no indications for super-structure reflections in the Se-treated mordenite-Na. The cell dimensions of both samples are very similar (Table 4.1) and the Se-treated crystal displayed only a significant expansion (0.2%) along the b -axis, the direction where the large channel with elliptical cross section is oblate. The results of the structure refinement, comprising atomic coordinates, populations, isotropic displacement parameters are given in Tables 4.3 - 4.6 for Se-mordenite-Na and 4.7 - 4.9 for mordenite-Na in the "crystallographic data" part of this chapter.

Both samples show within two standard deviations the same mean T-O bond lengths

(Table 4.10 and 4.11). Mean T-O distances vary between 1.596 for T2c-O and 1.640 for T3a-O. Shortest bond lengths are in both samples around T2a-d. No estimations were made about Si/Al ordering, but based on T-O bond lengths a slight Al enrichment is assumed for tetrahedra in the 4-membered rings (T3 and T4), which is in agreement with literature data [26, 27].

In mordenite-Na 4 Na sites were located, whereas in Se-mordenite-Na only 3 sites were found. Highest occupied Na1 (2.64 pfu in Se-mordenite-Na, 2.32 pfu in mordenite-Na) is situated in the center of the compressed 8-membered ring channel along c . Na2 is located at the intersection of the large 12-membered ring channel along c to the 8-membered ring channel along b . Na2 in the Se-mordenite-Na is occupied with 2.28 pfu, whereas the Na2 site in mordenite-Na was split in two satellite positions Na2a (0.52 pfu) and Na2b (0.76 pfu). The third Na site is located in the 12-membered ring channel but shifted from the center along b . Na3 in Se-mordenite-Na has the lowest occupation with 1.76 pfu. In mordenite-Na this site is also split in two satellite positions Na3a (1.36 pfu) and Na3b (1.16 pfu). In mordenite-Na, another site (Na4) is located in the center of the 12-membered ring channel along c , which is missing in the Se-mordenite-Na. Comparing extraframework cation distributions in synthetic mordenite-Na at room temperature [26] and 120 K, positions and occupations of the other Na sites are almost identical, whereas the Na3 site in low-temperature mordenite is slightly higher occupied than at room temperature. By comparison of the extraframework cation distribution in Se-mordenite-Na and mordenite-Na, it is obvious that the Na2 site in Se-mordenite-Na is higher occupied than in mordenite-Na, whereas the Na3 position situated in the 12-membered ring channel, is significantly lower occupied in Se-mordenite-Na. This can be explained by a partial displacement of Na by the Se chains and the partially dehydrated status of Se-mordenite-Na.

4.3.2 Se incorporation

Se incorporated under different conditions and in different types of mordenite has been widely investigated by Raman spectroscopy [9-15]. Prominent vibration bands in Se-modified mordenites lie between 200 cm^{-1} and 300 cm^{-1} . Raman spectra of Se-mordenite can be compared with the vibration spectra of elemental Se. The most active Raman band in helical, trigonal Se is the A1 symmetric stretching mode at 237 cm^{-1} ,

which strongly depends on chain interactions [28]. The most dominant vibrational band in our Se-mordenite-Na was detected at 254 cm^{-1} . According to the literature, the 254 cm^{-1} band in Se-mordenite can be attributed to the A1 symmetric stretching mode in elemental trigonal Se [9-15]. The difference between the A1 mode of elemental Se and Se in mordenite can be interpreted as interaction of Se with channel wall atoms, but also as a missing chain interaction in Se-mordenite because the single chains are laterally separated through the mordenite channels.

Bands characteristic of other forms than chains, e.g. Se_6 or Se_8 rings, were not observed. Our results from Raman spectroscopy are completely consistent with other spectroscopy studies according to incorporation conditions, methods, and used mordenite samples. The results clearly suggest a chain like arrangement of incorporated Se. Compared to the sharp 237 cm^{-1} stretching mode in trigonal Se [29], the 254 cm^{-1} band of Se-mordenite-Na is strongly broadened. This broadening can be interpreted as an overlay due to Se chains with different geometries. To check the existence of SeO species (SeO_2 , selenites, selenates), the Raman spectra of Se-mordenite-Na was compared with Se-O stretching modes as they occur in SeO species. The vibrational behaviour of SeO_2 is well established [30] and shows prominent modes between 500 cm^{-1} and 900 cm^{-1} . Our Raman spectra displays no bands in this region. Therefore, it can be concluded to that no moieties containing Se-O bonds are present in the structure.

4.3.3 Se atoms

Six chains (all only partly occupied) consisting of up to 7 Se atoms were found, all located in the large 12-membered channel along the c -axis. Because 1^{st} neighbor and 2^{nd} neighbor distances in Se chains are well established, these distances were fixed to 2.34 \AA (1^{st} neighbor) and 3.62 \AA (2^{nd} neighbor) [17–19], resulting in bond angles of 102° . Such constrains were necessary to handle the overlay of partly occupied chain fragments. Distances of 3^{rd} and further neighbors were not fixed resulting in bonds of different lengths ($4 - 6\text{ \AA}$ to the 3^{rd} neighbor) and different dihedral angles. The population was constrained to be equal within a chain, and isotropic displacement parameters were constrained to be equal for all Se atoms.

Chain A has a length of 9.85 \AA and is made up of 7 Se atoms. The chain has a total

population of 2.1 Se pfu. The closest distance to channel oxygen is 3.14 Å from Se atom A7 to O7b. 3rd neighbor distances are A1-A4 4.79 Å, A2-A5 5.45 Å, A3-A6 4.47 Å and A4-A7 5.56 Å with torsion angles of 99.4° (A1-A2-A3-A4), 142.9° (A2-A3-A4-A5), 81.8° (A3-A4-A5-A6) and 159.8° (A4-A5-A6-A7).

Chain B contains also 7 Se atoms and is 8.84 Å long with a total population of 1.8 Se pfu. The shortest distance to the channel wall is between Se at B4 and O10 with 3.08 Å. 3rd neighbor distances are B1-B4 4.10 Å, B2-B5 5.62 Å, B3-B6 4.93 Å and B4-B7 5.61 Å with torsion angles of 67.3° (B1-B2-B3-B4), 172.9° (B2-B3-B4-B5), 107.1° (B3-B4-B5-B6) and 178.4° (B4-B5-B6-B7).

Se chain C consists of 6 atoms with a length of 8.5 Å and has a low occupancy of 0.6 Se pfu. The closest framework oxygen is O3d to C6 with a distance of 3.24 Å. 3rd neighbor distances are C1-C4 5.117 Å, C2-C5 4.48 Å and C3-C6 5.57 Å with torsion angles of -112.6° (C1-C2-C3-C4), -75.6° (C2-C3-C4-C5) and -147.5° (C3-C4-C5-C6).

Chain D with 7 Se atoms has a length of 8.9 Å and is populated with 1.12 Se pfu. Closest distance to channel oxygen is 3.12 Å from Se atom D2 to O3b. 3rd neighbor distances are D1-D4 5.57 Å, D2-D5 4.61 Å, D3-D6 5.41 Å and D4-D7 4.73 Å with torsion angles of 163.1° (D1-D2-D3-D4), -90.9° (D2-D3-D4-D5), -140.2° (D3-D4-D5-D6) and 97.5° (D4-D5-D6-D7).

Chain E has a length of 8.1 Å and a low occupancy of 0.84 Se pfu. O7b is nearest to E7 with a bond length of 3.04 Å. 3rd neighbor distances are E1-E4 4.3 Å, E2-E5 4.94 Å, E3-E6 5.62 Å and E4-E7 5.18 Å with torsion angles of 73.7° (E1-E2-E3-E4), -107.7° (E2-E3-E4-E5), -176.9° (E3-E4-E5-E6) and 121.8° (E4-E5-E6-E7).

Chain F is the longest chain with 10.3 Å and has a high population of 2.1 pfu. F1 is closely located to O7a (3.07 Å). 3rd neighbor distances are F1-F4 5.06 Å, F2-F5 5.35 Å, F3-F6 5.35 Å and F4-F7 5.63 Å with torsion angles of 113.8° (F1-F2-F3-F4), 136.2° (F2-F3-F4-F5), -134.1° (F3-F4-F5-F6) and 173.3° (F4-F5-F6-F7). Four additional low occupied Se positions were located in the 12-membered ring channel but could not be assigned to a chain. Distances and angles are summarized in Table 4.2.

3rd neighbor			Torsion angle				
Atom 1	Atom 2	Distance	Atom 1	Atom 2	Atom 3	Atom 4	Angle
A1	A4	4.80(2)	A1	A2	A3	A4	99.415(7)
A2	A5	5.46(2)	A2	A3	A4	A5	142.908(6)
A3	A6	4.47(2)	A3	A4	A5	A6	81.796(9)
A4	A7	5.57(2)	A4	A5	A6	A7	159.746(4)
Chain length							
A1	A7	9.85(2)					
3rd neighbor			Torsion angle				
Atom 1	Atom 2	Distance	Atom 1	Atom 2	Atom 3	Atom 4	Angle
B1	B4	4.11(3)	B1	B2	B3	B4	67.342(9)
B2	B5	5.62(2)	B2	B3	B4	B5	172.961(1)
B3	B6	4.93(3)	B3	B4	B5	B6	107.146(9)
B4	B7	5.62(2)	B4	B5	B6	B7	178.421(2)
Chain length							
B1	B7	8.85(3)					
3rd neighbor			Torsion angle				
Atom 1	Atom 2	Distance	Atom 1	Atom 2	Atom 3	Atom 4	Angle
C1	C4	5.12(5)	C1	C2	C3	C4	-112.606(1)
C2	C5	4.48(5)	C2	C3	C4	C5	-75.639(7)
C3	C6	5.56(4)	C3	C4	C5	C6	147.487(5)
Chain length							
C1	C6	8.54(5)					
3rd neighbor			Torsion angle				
Atom 1	Atom 2	Distance	Atom 1	Atom 2	Atom 3	Atom 4	Angle
D1	D4	5.57(3)	D1	D2	D3	D4	163.132(3)
D2	D5	4.61(3)	D2	D3	D4	D5	-90.874(8)
D3	D6	5.41(3)	D3	D4	D5	D6	-140.340(4)
D4	D7	4.73(3)	D4	D5	D6	D7	97.531(2)
Chain length							
D1	D7	8.87(3)					
3rd neighbor			Torsion angle				
Atom 1	Atom 2	Distance	Atom 1	Atom 2	Atom 3	Atom 4	Angle
E1	E4	4.30(4)	E1	E2	E3	E4	73.686(8)
E2	E5	4.94(3)	E2	E3	E4	E5	-107.649(9)
E3	E6	5.62(4)	E3	E4	E5	E6	-176.911(7)
E4	E7	5.18(4)	E4	E5	E6	E7	121.863(7)
Chain length							
E1	E7	8.10(4)					
3rd neighbor			Torsion angle				
Atom 1	Atom 2	Distance	Atom 1	Atom 2	Atom 3	Atom 4	Angle
F1	F4	5.06(2)	F1	F2	F3	F4	113.806(6)
F2	F5	5.35(2)	F2	F3	F4	F5	136.173(7)
F3	F6	5.35(2)	F3	F4	F5	F6	-134.121(5)
F4	F7	5.63(2)	F4	F5	F6	F7	173.326(8)
Chain length							
F1	F7	10.27(2)					

Table 4.2: Chain lengths (\AA), 3^{rd} neighbour distances (\AA) and torsion angles ($^{\circ}$) of Se chains. 1^{st} and 2^{nd} neighbour distances and bond angle are not displayed because they were fixed during refinement. Corresponding mean bond lengths and angle are: $2.34(3) \text{\AA}$ (1^{st} neighbour), $3.62(2) \text{\AA}$ (2^{nd} neighbour) and $102(1)^{\circ}$ (bond angle)

4.4 Discussion

4.4.1 H₂O in Se-loaded mordenite-Na

Dehydration of natural and cation exchanged mordenites is widely discussed in the literature [31–35]. The framework of mordenite shows almost no lattice deformation upon dehydration. Total water loss in natural mordenite was predicted at 300 °C [32], for mordenite-Ca at 500 °C, respectively [33]. The H₂O site, which is most resistant to dehydration, coordinates the extraframework cations within the compressed 8-membered ring channels. In natural mordenite Ca usually occupies this site [26], which bonds considerably stronger to H₂O than Na in our synthetic mordenite-Na. This explains the lower dehydration temperature (ca. 280 °C) for mordenite-Na. Compared to mordenite-Na (19 H₂O per formula unit, Fig. 4.5), 10 pfu H₂O molecules were detected in Se-mordenite-Na. This H₂O content can be explained by rehydration due to subsequent storage of the sample at ambient humidity conditions. Even if the large channels are plugged by Se chains, H₂O molecules find appropriate diffusion pathways along the compressed 8-membered ring channels along *b* and *c*. A reaction of this re-incorporated H₂O and Se within the structure at ambient conditions cannot be expected. The H₂O molecules in Se-mordenite-Na are located at 5 different sites: (1) A highly populated position in the 8-membered ring channel along *c*, which is coordinated to Na1. (2) Two positions in the 8-membered ring channel along *b*, (3) two positions in the 12-membered ring channel along *c* close to the Na2 and Na3 positions (Fig. 4.6).

4.4.2 The mordenite framework

The mordenite structure at room temperature is usually refined in space group *Cmcm* or *Cmc2₁*, respectively [4, 27]. Simonic and Armbruster [26] proposed a domain like structure where about 3% of the Si/Al framework is shifted by *c*/2. In spite of these studies, the symmetry of the framework is generally handled as pseudosymmetry and represents only a fair approximation. Lower symmetries or micro-twin models are also supposed [36] but not proven by experiments. Several space groups were tested during structural refinement: orthorhombic *Cmcm* and *Cmc2₁*, and monoclinic *C2/c* and *Cc*. For mordenite-Na and Se-mordenite-Na at 120 K the space group *Cc* represents the

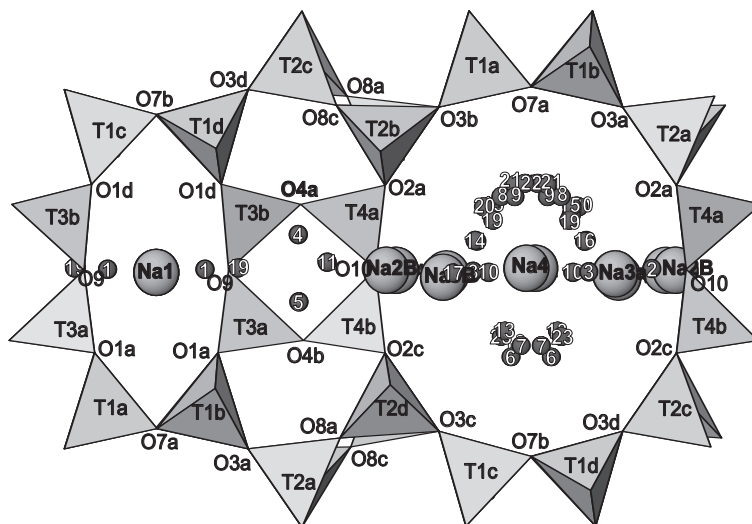


Figure 4.5: Extraframework cation and H₂O molecule positions in mordenite-Na. Small circles with numbers correspond to H₂O positions.

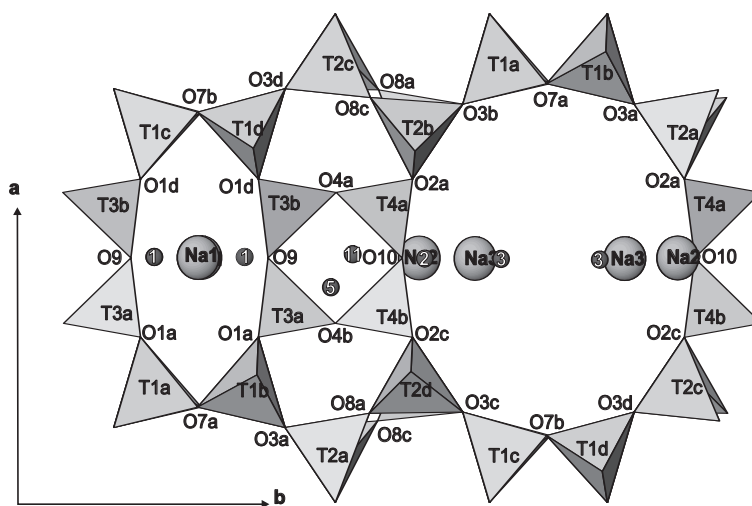


Figure 4.6: Extraframework cation and H₂O molecule positions in Se-mordenite-Na. Small circles with numbers correspond to H₂O positions. Se positions are not displayed.

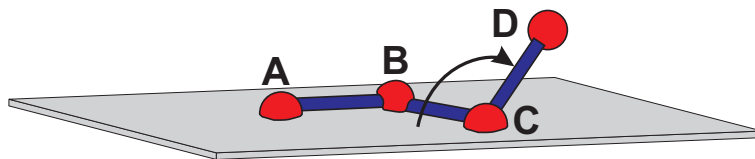


Figure 4.7: Torsion angle within a group of four atoms A-B-C-D: A torsion angle is defined as the angle from the plane built by atom A, B and C to atom D. Positive angles are clockwise oriented, negative angles counter clockwise.

most suitable model. Because the Cc model fits both structures, it can be ruled out that a phase transition from $Cmc2_1$ to Cc occurred due to Se incorporation. Application of low temperature (120 K), chosen for an improved resolution of extraframework occupants, led also to a better resolution of the complex disordered microstructure within the tetrahedral framework [36]. However, we were not able to develop a correct intergrowth/twinning model for the description of the tetrahedral framework. After refinements in space group $Cmcm$ and $Cmc2_1$ indicated only poor agreement between structure model and diffraction data, we have chosen as a "best" compromise the monoclinic space group Cc . Furthermore, to reduce correlation problems due to pseudo symmetry, related tetrahedral sites and their atomic displacement parameters were constrained to each other. As will be shown below, Se chains may be longer than the periodicity of the framework parallel to the channel axis. The fact that we did not observe any superstructure reflection or diffuse scattering evidence for the Se-treated mordenite-Na, different to mordenite-Na, indicates that the distribution of Se chains along the c -axis is rather random.

4.4.3 Arrangement of Se atoms in mordenite

For a better understanding of Se arrangement in mordenite, it is important to discuss some principal geometrical features of Se chains. In a chain of atoms A-B-C-D, the torsion angle or dihedral angle is defined as the angle between the plane containing the atoms A, B, C and that containing B, C, D, having an absolute value between 0° and 180° (Fig. 4.7).

Positive torsion angles are oriented clockwise, negative angles counter clockwise. Minimal 3^{rd} neighbor distance results from a torsion angle of 0° , which is the energet-

ically most unfavorable conformation, whereas maximal 3^{rd} neighbor distance results from a torsion angle of 180° . For comparison, the torsion angle in trigonal helical Se is ideally 101° with a 3^{rd} neighbor distance of 4.95 \AA , which corresponds to the c -axis of the unit cell of this modification [7]. 101° is for trigonal Se the energetically most favorable dihedral angle because of repulsion between non-bonding lone-pair electrons on the adjacent Se atoms in the chain [19]. Most studies concerning Se incorporated into mordenite investigated short-range order and bonding of the Se atoms. Therefore the 1^{st} and 2^{nd} neighbor distances in mordenite Se chains are well established, but the 3^{rd} neighbor distance and torsion angle are difficult to determine with spectroscopic methods and rather controversial models were proposed. The dihedral angle is crucial for the geometry of the Se chain because it represents the "softest" structural parameter with the highest rotational potential. In our refinement we arranged 6 Se chains, each with different geometry related to torsion angles and 3^{rd} neighbor distances. 7.9 Se per formula unit were determined analytically by electron microprobe, but 10.04 Se pfu. were obtained from structure refinement. The excess of refined Se may be explained by disorder of Se chains, and possible overlay with extraframework Na and H_2O , or even due to Se loss under the electron beam of the electron microprobe. Torsion angles within the chains differ between 67° and 180° , which deviate clearly from the value in trigonal Se. 3^{rd} neighbor distances range between $4.11(3) \text{ \AA}$ and $5.63(2) \text{ \AA}$. The arrangement in the refined Se chains can be simplified by introducing two idealized geometrical conformations: (1) Torsion angle $< 160^\circ$ resulting in a staggered arrangement of 4 coherent Se atoms, similar to the conformation in trigonal Se. (2) Torsion angle $> 160^\circ$ resulting in a planar, zigzag-shaped arrangement of 4 coherent Se atoms (Fig. 4.8).

These two conformations appear side by side in the Se chains, which is shown in Figs. 4.9 and 4.10 for chain B and F. The zigzag-like geometry corresponds to the chains calculated by the semi-empirical models of Ikawa et al. [20, 21]. They showed that Se chain geometries with dihedral angles between 70° and 180° are possible. Although a planar arrangement disagrees with the torsion angle in trigonal Se, this can be interpreted [20, 21] as chain defects due to the influence of channel cations or H_2O molecules. Katayama et al. [19] used results from EXAFS to derive 1^{st} , 2^{nd} and 3^{rd} neighbor distances as well as bond- and dihedral angle and postulated that the helical chain form is preserved. However, the uniform dihedral angle of 74° and 3^{rd} neighbor

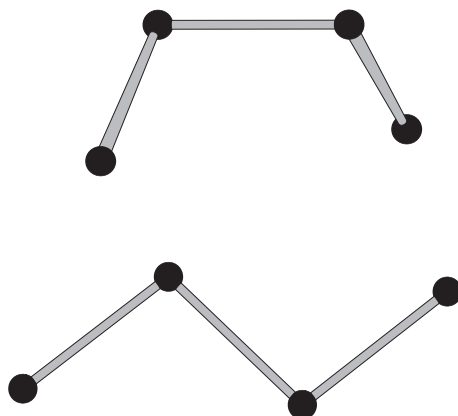


Figure 4.8: Staggered arrangement with dihedral angle $< 160^\circ$. Planar arrangement with dihedral angle $> 160^\circ$

distance of $4.32(4)$ Å as principal structure parameters for a Se chain in mordenite cannot be confirmed by our refinements. Porbochii et al. [10] proposed, based on Raman spectroscopy, a uniformly shaped Se chain formed by cis- and trans-segments. These segments consist of two different bond lengths (1^{st} neighbor distances) and two different bond angles with varying negative and positive dihedral angle of 90° . This Se arrangement cannot be supported by our study nor by other spectroscopic studies where the 1^{st} neighbor distances were clearly determined at 2.34 Å. The study of Boglomov et al. [8] supports our suggestion that the Se chain in mordenite differs from trigonal Se and shows variable geometry. Due to the influence of framework atoms and the symmetry-superposition principle, they concluded that Se chains located in the mordenite channel has not the symmetry of trigonal Se as the dihedral angle of the Se chain varies randomly. The Se-chain geometry is also influenced by adjacent framework oxygen. Closest distances between a chain atom and a framework oxygen range from 3.04 Å to 3.40 Å. This is longer than the covalent Se-O bond length (1.624 Å, 1.795 Å, respectively) in SeO_2 [37], but shorter than the sum of the van der Waals radii of Se and O (3.42 Å) Thus there is a slight electrostatic interaction between the Se atom and the adjacent oxygen of the framework. Other Se species like Se_6 and even Se_8 rings were postulated by Poborchii et al. [11, 12]. The latter authors compared Raman spectra of Se-mordenite and trigonal as well as monoclinic elemental Se and postulated the existence of chains and rings in the 12-membered channel of mordenite.

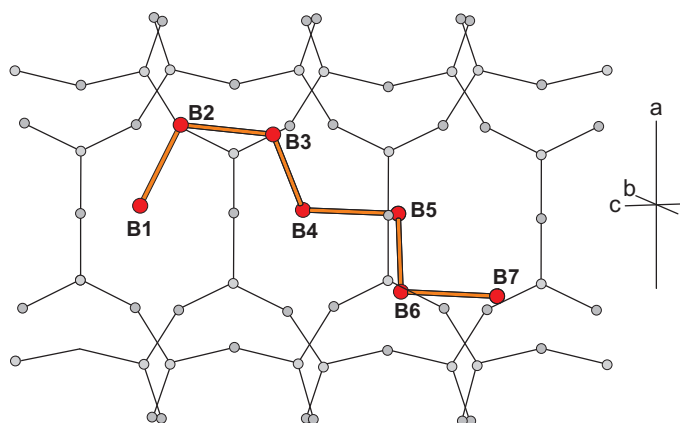


Figure 4.9: Chain B: Atoms B1-B2-B3-B4 (67°) and B3-B4-B5-B6 (107°) build a staggered geometry whereas B2-B3-B4-B5 (173°) and B4-B5-B6-B7 (178°) have a zigzag geometry

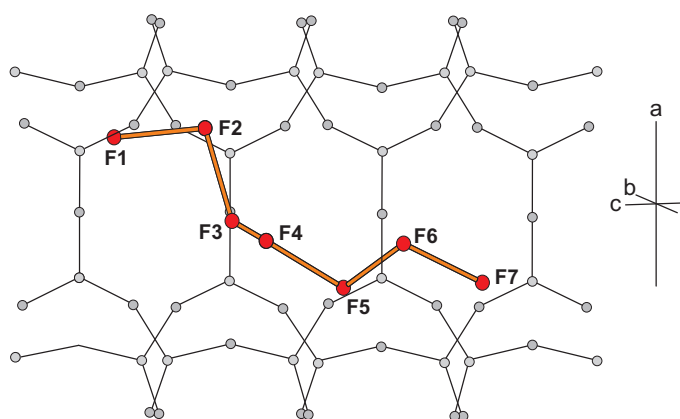


Figure 4.10: Torsion angle from atom groups F1-F2-F3-F4, F2-F3-F4-F5 and F3-F4-F5-F6 have all staggered geometry, only F4-F5-F6-F7 has zigzag geometry.

In our study Se_6 or Se_8 rings were neither confirmed by structure refinement nor by Raman spectroscopy. Poborchii et al. [13] investigated also the dependence of type of extraframework cations on the concentration of Se species, observing higher concentrations of Se_6 rings in mordenite-K than in mordenite-Na. Because of electrostatic interactions between Se chains and framework, influence of disordered channel cations and H_2O molecules, the Se chains display variable forms. Furthermore, due to residual Se positions in the difference Fourier map, the proposed refined arrangement of Se chains can only be taken as a fair approximation to the real chain geometry. However, regular chain geometry as in trigonal Se cannot be confirmed by our data. Strong disorder of the Se arrangement has to be supposed and no prediction can be made about the real length of a Se chain. Summarizing it must be concluded that Se chains in mordenite are not uniform, but show highly variable geometrical arrangement.

4.5 Crystallographic data

Table 4.3 - 4.6: Atomic coordinates and Beq values for synthetic Se-mordenite-Na (space group Cc). ¹⁻²² coordinates with the same superscript were constrained to be equal. All atomic parameters (coordinates, population, isotropic displacement factors) labeled B are fully constrained and belong to a domain of mordenite shifted $c/2$ relative to the main part of the structure [26]. ^{a-g} Parameters of the Se-sites with the same superscript were constrained to be equal.

Starred atoms with standard deviation were refined isotropically, those without standard deviations were fixed. Anisotropically refined atoms are given in the form of the isotropic equivalent thermal parameter defined as $B_{eq} = 8/3 \pi^2 \sum_i (\sum_j (U_{ij} a_i^* a_j^* a_i \cdot a_j))$

Table 4.7 - 4.9: Atomic coordinates and Beq values for synthetic mordenite-Na (space group Cc). ¹⁻²⁵ coordinates with the same superscript were constrained to be equal. All atomic parameters (coordinates, population, isotropic displacement factors) labeled B are fully constrained and belong to a domain of mordenite shifted $c/2$ relative to the main part of the structure [26].

Starred atoms with standard deviation were refined isotropically, those without standard deviations were fixed. Anisotropically refined atoms are given in the form of the isotropic equivalent thermal parameter defined as $B_{eq} = 8/3 \pi^2 \sum_i (\sum_j (U_{ij} a_i^* a_j^* a_i \cdot a_j))$

Table 4.10 and 4.11: T-O distances (\AA) and T-O-T angles of Se-mordenite-Na and mordenite-Se with standard deviations in parentheses

Table 4.12 and 4.13: Anisotropic displacement parameters U_{ij} of Se-mordenite-Na and mordenite-Na

Atom	Population	x	y	z	B_{eq} [\AA^2]
T1a	0.970(1)	0.30252(4) ¹	0.07286(9) ²	0.1683(3) ³	1.03(3)
T1b	0.970(1)	0.30252(4) ¹	-0.07286(9) ²	0.0835(6)	1.03(3)
T1c	0.970(1)	-0.30252(4) ¹	0.07286(9) ²	0.1683(3) ³	1.11(4)
T1d	0.970(1)	-0.30252(4) ¹	-0.07286(9) ²	0.0837(3)	1.11(4)
T2a	0.970(1)	0.19671(4) ⁴	0.19037(9) ⁵	0.6698(4)	1.11(3)
T2b	0.970(1)	0.19671(4) ⁴	0.19037(9) ⁵	0.0789(3) ⁶	1.11(3)
T2c	0.970(1)	-0.19671(4) ⁴	0.19037(9) ⁵	-0.3304(3)	1.18(4)
T2d	0.970(1)	-0.19671(4) ⁴	0.19037(9) ⁵	0.0789(3) ⁶	1.18(4)
T3a	0.970(1)	0.4132(2)	-0.11776(5) ⁷	0.3743(4) ⁸	1.10(3)
T3b	0.970(1)	-0.4122(2)	-0.11776(5) ⁷	0.3743(4) ⁸	0.84(3)
T4a	0.970(1)	0.0865(2)	0.22740(5) ⁹	0.3766(4) ¹⁰	0.84(3)
T4b	0.970(1)	-0.0877(2)	0.22740(5) ⁹	0.3766(4) ¹⁰	1.10(3)
O1a	0.970(1)	0.3778(1) ¹¹	-0.0845(1) ¹²	0.1989(7) ¹³	2.62(5)
O1b	0.970(1)	0.3778(1) ¹¹	-0.0845(1) ¹²	0.5558(6) ¹⁴	2.62(5)
O1c	0.970(1)	-0.3778(1) ¹¹	-0.0845(1) ¹²	0.1989(7) ¹³	2.62(5)
O1d	0.970(1)	-0.3778(1) ¹¹	-0.0845(1) ¹²	0.5558(6) ¹⁴	2.62(5)
O2a	0.970(1)	0.1224(1) ¹⁵	0.1946(1) ¹⁶	0.2021(7) ¹⁷	2.1(1)
O2b	0.970(1)	0.1224(1) ¹⁵	0.1946(1) ¹⁶	0.5558(6) ¹⁴	2.1(1)
O2c	0.970(1)	-0.1224(1) ¹⁵	0.1946(1) ¹⁶	0.2021(7) ¹⁷	2.3(1)
O2d	0.970(1)	-0.1224(1) ¹⁵	0.1946(1) ¹⁶	0.5558(6) ¹⁴	2.3(1)
O3a	0.970(1)	0.2380(1) ¹⁸	0.1228(1) ¹⁹	0.639(1)	3.04(7)
O3b	0.970(1)	0.2380(1) ¹⁸	0.1228(1) ¹⁹	0.119(1)	2.90(7)
O3c	0.970(1)	-0.2380(1) ¹⁸	-0.1228(1) ¹⁹	0.615(1)	3.04(7)
O3d	0.970(1)	-0.2380(1) ¹⁸	-0.1228(1) ¹⁹	0.142(1)	2.90(7)
O4a	0.970(1)	-0.3991(4)	-0.1960(3)	0.3578(9)	2.01(5)
O4b	0.970(1)	0.4015(4)	-0.1953(3)	0.3572(9)	2.05(7)
O5a	0.970(1)	0.1665(5)	0.1912(4)	0.876(1)	2.75(8)
O5b	0.970(1)	-0.1746(5)	0.1970(4)	-0.122(1)	2.75(8)
O6a	0.970(1)	0.3192(4)	0.0821(4)	0.3736(9) ²⁰	2.01(5)
O6b	0.970(1)	-0.3302(4)	0.0772(4)	0.3736(9) ²⁰	2.01(5)
O7a	0.970(1)	0.2700(4)	0.0014(3) ²¹	0.1148(9) ²²	1.90(6)
O7b	0.970(1)	-0.2740(4)	0.0014(3) ²¹	0.1148(9) ²²	1.90(6)
O8a	0.38(5)	0.244(1)	-0.256(1)	0.169(4)	2.4*
O8b	0.61(5)	0.2569(9)	-0.2435(8)	0.120(3)	2.4*
O8c	0.60(7)	0.2494(8)	-0.2570(6)	-0.399(3)	2.4*
O8d	0.39(7)	0.262(2)	-0.247(1)	-0.344(6)	2.4*
O9	0.970(1)	0.4999(5)	-0.0983(2)	0.386(1)	2.01(5)
O10	0.970(1)	0	0.2097(2)	0.379(2)	2.05(7)

Table 4.3: Atomic coordinates and B_{eq} values for synthetic Se-mordenite-Na

Atom	Population	x	y	z	B_{eq} [\AA^2]
T1Ba	0.029(1)	-0.30252(4)	-0.07286(9)	0.1683(3)	2.37*
T1Bb	0.029(1)	-0.30252(4)	0.07286(9)	0.0835(6)	2.37*
T1Bc	0.029(1)	0.30252(4)	-0.07286(9)	0.1683(3)	2.37*
T1Bd	0.029(1)	0.30252(4)	0.07286(9)	0.0837(3)	2.37*
T2Ba	0.029(1)	-0.19671(4)	-0.19037(9)	0.6698(4)	2.37*
T2Bb	0.029(1)	-0.19671(4)	-0.19037(9)	0.0789(3)	2.37*
T2Bc	0.029(1)	0.19671(4)	-0.19037(9)	-0.3304(3)	2.37*
T2Bd	0.029(1)	0.19671(4)	-0.19037(9)	0.0789(3)	2.37*
T3Ba	0.029(1)	-0.4132(2)	0.11776(5)	0.3743(4)	2.37*
T3Bb	0.029(1)	0.4122(2)	0.11776(5)	0.3743(4)	2.37*
T4Ba	0.029(1)	0.0877(2)	-0.22740(5)	0.3766(4)	2.37*
T4Bb	0.029(1)	-0.0865(2)	-0.22740(5)	0.3766(4)	2.37*
O1Bc	0.029(1)	0.3778(1)	0.0845(1)	0.5558(6)	2.37*
O1Bd	0.029(1)	0.3778(1)	0.0845(1)	0.1989(7)	2.37*
O1Bb	0.029(1)	-0.3778(1)	0.0845(1)	0.5558(6)	2.37*
O1Ba	0.029(1)	-0.3778(1)	0.0845(1)	0.1989(7)	2.37*
O2Ba	0.029(1)	-0.1224(1)	-0.1946(1)	0.2021(7)	2.37*
O2Bb	0.029(1)	-0.1224(1)	-0.1946(1)	0.5558(6)	2.37*
O2Bd	0.029(1)	0.1224(1)	-0.1946(1)	0.5558(6)	2.37*
O2Bc	0.029(1)	0.1224(1)	-0.1946(1)	0.2021(7)	2.37*
O3Ba	0.029(1)	-0.2380(1)	-0.1228(1)	0.639(1)	2.37*
O3Bb	0.029(1)	-0.2380(1)	-0.1228(1)	0.119(1)	2.37*
O3Bc	0.029(1)	0.2380(1)	0.1228(1)	0.615(1)	2.37*
O3Bd	0.029(1)	0.2380(1)	0.1228(1)	0.142(1)	2.37*
O4Ba	0.029(1)	0.3991(4)	0.1960(3)	0.3578(9)	2.37*
O4Bb	0.029(1)	0.1015(4)	-0.3053(3)	0.3572(9)	2.37*
O5Ba	0.029(1)	-0.1665(5)	-0.1912(4)	0.876(1)	2.37*
O5Bb	0.029(1)	0.1746(5)	-0.1970(4)	-0.122(1)	2.37*
O6Bb	0.029(1)	0.3302(4)	-0.0772(4)	0.3736(9)	2.37*
O6Ba	0.029(1)	-0.3192(4)	-0.0821(4)	0.3736(9)	2.37*
O7Bb	0.029(1)	0.2740(4)	-0.0014(3)	0.1148(9)	2.37*
O7Ba	0.029(1)	-0.2700(4)	-0.0014(3)	0.1148(9)	2.37*
O9B	0.029(1)	-0.4999(5)	0.0983(2)	0.386(1)	2.37*
O10B	0.029(1)	0	-0.2097(2)	0.379(2)	2.37*

Table 4.4: Atomic coordinates and B_{eq} values for synthetic Se-mordenite-Na; continued

Atom	Population	x	y	z	B_{eq} [\AA^2]
Na1	0.66(1)	0.5002(8)	0.0006(6)	0.125(1)	4.1(1)
Na2	0.57(1)	0.001(1)	0.1845(5)	0.848(2)	7.90*
Na3	0.44(2)	0.0011(9)	0.1252(9)	0.647(2)	7.90*
W1	1.0	0.5005(8)	-0.0648(4)	0.877(2)	5.2(2)
W2	0.25(2)	0.000(3)	-0.174(3)	0.517(8)	7.90*
W3	0.42(1)	0.002(2)	0.092(1)	0.934(3)	7.90*
W5	0.55(2)	-0.545(1)	-0.189(1)	0.871(3)	7.90*
W11	0.29(2)	-0.504(2)	-0.217(2)	0.950(5)	7.90*
Se chain A					
A1	0.075(1) ^a	0.0570(9)	0.0198(9)	0.126(2)	3.48(8)* ^g
A2	0.075(1) ^a	0.1275(8)	-0.0184(8)	0.366(2)	3.48(8)* ^g
A3	0.075(1) ^a	0.0626(9)	0.0240(6)	0.611(1)	3.48(8)* ^g
A4	0.075(1) ^a	-0.0059(8)	-0.0675(6)	0.698(2)	3.48(8)* ^g
A5	0.075(1) ^a	-0.0059(8)	-0.0604(7)	0.007(2)	3.48(8)* ^g
A6	0.075(1) ^a	-0.102(1)	0.0146(8)	0.055(2)	3.48(8)* ^g
A7	0.075(1) ^a	-0.132(1)	-0.0066(9)	0.353(2)	3.48(8)* ^g
Se chain B					
B1	0.056(1) ^b	0.006(1)	0.0580(9)	0.364(3)	3.48(8)* ^g
B2	0.056(1) ^b	0.105(1)	-0.010(1)	0.438(2)	3.48(8)* ^g
B3	0.056(1) ^b	0.0994(9)	-0.007(1)	0.750(2)	3.48(8)* ^g
B4	0.056(1) ^b	-0.012(1)	-0.062(1)	0.800(2)	3.48(8)* ^g
B5	0.056(1) ^b	-0.0121(9)	-0.0711(8)	0.109(2)	3.48(8)* ^g
B6	0.056(1) ^b	-0.103(1)	0.005(1)	0.188(2)	3.48(8)* ^g
B7	0.056(1) ^b	-0.105(1)	-0.007(1)	0.498(2)	3.48(8)* ^g
Se chain C					
C1	0.027(1) ^c	0.091(2)	-0.003(3)	0.393(6)	3.48(8)* ^g
C2	0.027(1) ^c	0.037(2)	-0.047(2)	0.647(4)	3.48(8)* ^g
C3	0.027(1) ^c	-0.072(2)	0.014(2)	0.673(3)	3.48(8)* ^g
C4	0.027(1) ^c	-0.057(2)	0.063(1)	0.949(3)	3.48(8)* ^g
C5	0.027(1) ^c	-0.093(3)	-0.019(2)	0.145(4)	3.48(8)* ^g
C6	0.027(1) ^c	-0.12361	0.039(2)	0.400(3)	3.48(8)* ^g

Table 4.5: Atomic coordinates and B_{eq} values for synthetic Se-mordenite-Na; continued

Atom	Population	x	y	z	B_{eq} [\AA^2]
Se chain D					
D1	0.041(1) ^d	0.092(2)	0.044(1)	0.293(2)	3.48(8) ^{*g}
D2	0.041(1) ^d	0.105(2)	-0.033(1)	0.517(2)	3.48(8) ^{*g}
D3	0.041(1) ^d	0.100(1)	0.033(1)	0.773(2)	3.48(8) ^{*g}
D4	0.041(1) ^d	0.0761(9)	-0.046(1)	0.991(2)	3.48(8) ^{*g}
D5	0.041(1) ^d	-0.0531(9)	-0.047(1)	0.997(2)	3.48(8) ^{*g}
D6	0.041(1) ^d	-0.075(1)	-0.0569(9)	0.303(2)	3.48(8) ^{*g}
D7	0.041(1) ^d	-0.096(2)	0.052(1)	0.383(3)	3.48(8) ^{*g}
Se chain E					
E1	0.030(1) ^e	-0.065(1)	-0.036(2)	0.533(4)	3.48(8) ^{*g}
E2	0.030(1) ^e	0.063(1)	-0.045(2)	0.560(3)	3.48(8) ^{*g}
E3	0.030(1) ^e	0.087(1)	0.019(1)	0.811(3)	3.48(8) ^{*g}
E4	0.030(1) ^e	0.044(2)	-0.048(1)	0.041(3)	3.48(8) ^{*g}
E5	0.030(1) ^e	-0.064(2)	0.008(2)	0.125(3)	3.48(8) ^{*g}
E6	0.030(1) ^e	-0.104(2)	-0.056(1)	0.365(3)	3.48(8) ^{*g}
E7	0.030(1) ^e	-0.108(2)	0.021(2)	0.594(3)	3.48(8) ^{*g}
Se chain F					
F1	0.074(1) ^f	0.102(1)	0.0031(9)	0.054(2)	3.48(8) ^{*g}
F2	0.074(1) ^f	0.1120(6)	0.0194(9)	0.363(2)	3.48(8) ^{*g}
F3	0.074(1) ^f	-0.0083(7)	0.0508(7)	0.434(2)	3.48(8) ^{*g}
F4	0.074(1) ^f	-0.0467(8)	-0.0385(6)	0.613(1)	3.48(8) ^{*g}
F5	0.074(1) ^f	-0.1056(9)	0.0174(9)	0.846(1)	3.48(8) ^{*g}
F6	0.074(1) ^f	-0.0561(9)	-0.0375(7)	0.094(1)	3.48(8) ^{*g}
F7	0.074(1) ^f	-0.1038(9)	0.0270(9)	0.327(2)	3.48(8) ^{*g}
Var. Se atoms					
G1	0.095(3)	0.0962(9)	0.0041(8)	0.678(2)	3.48(8) ^{*g}
G2	0.128(4)	-0.1084(6)	0.0078(6)	0.910(2)	3.48(8) ^{*g}
G3	0.101(3)	-0.0980(7)	-0.0080(7)	0.252(2)	3.48(8) ^{*g}
G4	0.036(2)	0.002(2)	-0.069(1)	0.216(4)	3.48(8) ^{*g}

Table 4.6: Atomic coordinates and B_{eq} values for synthetic Se-mordenite-Na; continued

Atom	Population	x	y	z	B_{eq} [\AA^2]
T1a	0.968(1)	0.30201(3) ¹	0.07217(8) ²	0.1681(2) ⁴	1.33(3)
T1b	0.968(1)	0.30201(3) ¹	-0.07217(8) ²	0.08341(1)	1.33(3)
T1c	0.968(1)	-0.30201(3) ¹	0.07282(7) ³	0.1681(2) ⁴	1.13(3)
T1d	0.968(1)	-0.30201(3) ¹	-0.07282(7) ³	0.0840(3)	1.13(3)
T2a	0.968(1)	0.19658(3) ⁵	0.19079(7) ⁶	0.6721(2)	1.24(3)
T2b	0.968(1)	0.19658(3) ⁵	0.19079(7) ⁶	0.0812(2) ⁸	1.24(3)
T2c	0.968(1)	-0.19658(3) ⁵	0.19082(7) ⁷	-0.3279(2)	1.29(3)
T2d	0.968(1)	-0.19658(3) ⁵	0.19082(7) ⁷	0.0812(2) ⁸	1.29(3)
T3a	0.968(1)	0.4137(2)	-0.11694(4) ⁹	0.3754(3)	1.37(3)
T3b	0.968(1)	-0.4119(1)	-0.11694(4) ⁹	0.3755(3)	0.70(3)
T4a	0.968(1)	0.0846(1)	0.22748(4) ¹⁰	0.3788(3) ¹¹	0.70(3)
T4b	0.968(1)	-0.0889(1)	0.22748(4) ¹⁰	0.3788(3) ¹¹	1.37(3)
O1a	0.968(1)	0.3789(2) ¹²	-0.0822(3) ¹³	0.2016(8)	2.6(1)
O1b	0.968(1)	0.3789(2) ¹²	-0.0822(3) ¹³	0.5564(5) ¹⁴	2.3(1)
O1c	0.968(1)	-0.3740(3) ¹⁵	-0.0869(3) ¹⁶	0.2041(5)	3.6(1)
O1d	0.968(1)	-0.3740(3) ¹⁵	-0.0869(3) ¹⁶	0.5564(5) ¹⁴	3.1(2)
O2a	0.968(1)	0.12278(9) ¹⁷	0.19453(9) ¹⁸	0.2040(5) ¹⁹	3.1(1)
O2b	0.968(1)	0.12278(9) ¹⁷	0.19453(9) ¹⁸	0.5564(5) ¹⁴	3.1(1)
O2c	0.968(1)	-0.12278(9) ¹⁷	0.19453(9) ¹⁸	0.2040(5) ¹⁹	2.14(9)
O2d	0.968(1)	-0.12278(9) ¹⁷	0.19453(9) ¹⁸	0.5564(5) ¹⁴	2.14(9)
O3a	0.968(1)	0.2374(1) ²⁰	0.12274(9) ²¹	0.632(1)	4.1(2)
O3b	0.968(1)	0.2374(1) ²⁰	0.12274(9) ²¹	1.113(1)	3.9(2)
O3c	0.968(1)	-0.2374(1) ²⁰	-0.12274(9) ²¹	0.609(1)	3.3(1)
O3d	0.968(1)	-0.2374(1) ²⁰	-0.12274(9) ²¹	1.137(1)	3.6(2)
O4a	0.968(1)	-0.4024(3)	-0.1939(3)	0.365(1) ²²	2.1(1)
O4b	0.968(1)	-0.1011(5)	0.3047(3)	0.365(1) ²²	3.6(2)
O5a	0.968(1)	0.1673(4)	0.1899(4)	0.8723(9)	3.2(2)
O5b	0.968(1)	-0.1744(5)	0.1977(4)	-0.126(1)	3.5(2)
O6a	0.968(1)	0.3266(4)	0.0778(3)	0.3731(8) ²³	2.6(1)
O6b	0.968(1)	-0.3232(3)	0.0802(3)	0.3731(8) ²³	2.1(1)
O7a	0.968(1)	0.2721(4)	-0.0001(3) ²⁴	0.1307(8) ²⁵	2.2(1)
O7b	0.968(1)	-0.2686(4)	-0.0001(3) ²⁴	0.1307(8) ²⁵	2.1(1)
O8a	0.498(3)	0.2612(4)	0.2406(3)	0.610(2)	1.85(7)*
O8b	0.501(3)	0.2492(4)	0.2540(4)	0.094(1)	1.85(7)*
O8c	0.498(3)	0.2492(4)	0.2540(4)	0.661(1)	1.85(7)*
O8d	0.501(3)	0.2612(4)	0.2406(3)	0.146(2)	1.85(7)*
O9	0.968(1)	0.5020(4)	-0.0963(2)	0.380(1)	2.27(7)
O10	0.968(1)	0	0.2074(2)	0.378(1)	2.38(7)

Table 4.7: Atomic coordinates and B_{eq} values for synthetic mordenite-Na

Atom	Population	x	y	z	B_{eq} [\AA^2]
T1Ba	0.031(1)	-0.30201(3)	-0.07217(8)	0.1681(2)	2.37*
T1Bb	0.031(1)	-0.30201(3)	-0.07217(8)	-0.4159(1)	2.37*
T1Bc	0.031(1)	0.30201(3)	-0.07282(7)	0.1681(2)	2.37*
T1Bd	0.031(1)	0.30201(3)	0.07282(7)	0.0840(3)	2.37*
T2Ba	0.031(1)	-0.19658(3)	-0.19079(7)	0.6721(2)	2.37*
T2Bb	0.031(1)	-0.19658(3)	-0.19079(7)	0.0812(2)	2.37*
T2Bc	0.031(1)	0.19658(3)	-0.19082(7)	-0.3279(2)	2.37*
T2Bd	0.031(1)	0.19658(3)	-0.19082(7)	0.0812(2)	2.37*
T3Ba	0.031(1)	0.4119(1)	0.11694(4)	0.3755(3)	2.37*
T3Bb	0.031(1)	-0.4137(2)	0.11694(4)	0.3754(3)	2.37*
T4Ba	0.031(1)	0.0889(1)	-0.22748(4)	0.3788(3)	2.37*
T4Bb	0.031(1)	-0.0846(1)	-0.22748(4)	0.3788(3)	2.37*
O1Ba	0.031(1)	0.3740(3)	0.0869(3)	0.5564(5)	2.37*
O1Bb	0.031(1)	0.3740(3)	0.0869(3)	0.2040(5)	2.37*
O1Bc	0.031(1)	-0.3789(2)	0.0822(3)	0.5564(5)	2.37*
O1Bd	0.031(1)	-0.3789(2)	0.0822(3)	0.2016(8)	2.37*
O2Ba	0.031(1)	0.12278(9)	-0.19453(9)	0.5564(5)	2.37*
O2Bb	0.031(1)	0.12278(9)	-0.19453(9)	0.2040(5)	2.37*
O2Bc	0.031(1)	-0.12278(9)	-0.19453(9)	0.2040(5)	2.37*
O2Bd	0.031(1)	-0.12278(9)	-0.19453(9)	0.5564(5)	2.37*
O3Ba	0.031(1)	0.2374(1)	0.12274(9)	0.609(1)	2.37*
O3Bb	0.031(1)	0.2374(1)	0.12274(9)	1.137(1)	2.37*
O3Bc	0.031(1)	-0.2374(1)	-0.12274(9)	0.632(1)	2.37*
O3Bd	0.031(1)	-0.2374(1)	-0.12274(9)	1.113(1)	2.37*
O4Ba	0.031(1)	0.4024(3)	0.1939(3)	0.365(1)	2.37*
O4Bb	0.031(1)	0.1011(5)	-0.3047(3)	0.365(1)	2.37*
O5Ba	0.031(1)	0.1744(5)	-0.1977(4)	-0.126(1)	2.37*
O5Bb	0.031(1)	-0.1673(4)	-0.1899(4)	0.8723(9)	2.37*
O6Ba	0.031(1)	0.3232(3)	-0.0802(3)	0.3731(8)	2.37*
O6Bb	0.031(1)	-0.3266(4)	-0.0778(3)	0.3731(8)	2.37*
O7Ba	0.031(1)	0.2686(4)	0.0001(3)	0.1307(8)	2.37*
O7Bb	0.031(1)	-0.2721(4)	0.0001(3)	0.1307(8)	2.37*
O9B	0.031(1)	-0.5020(4)	0.0963(2)	0.380(1)	2.37*
O10B	0.031(1)	0	-0.2074(2)	0.378(1)	2.37*

Table 4.8: Atomic coordinates and B_{eq} values for synthetic mordenite-Na; continued

Atom	Population	x	y	z	B_{eq} [\AA^2]
NA1	0.580(9)	0.5009(6)	-0.0028(5)	0.637(1)	3.5(1)
NA2A	0.083(8)	0.000(2)	0.181(2)	1.024(5)	5.6(4)*
NA2B	0.26(3)	0.002(2)	-0.193(2)	0.355(4)	5.8(7)*
NA3A	0.35(2)	0.007(1)	0.113(1)	0.641(3)	7.90*
NA3B	0.26(2)	0.010(2)	0.117(2)	0.112(4)	7.90*
NA4	0.06(1)	0.010(3)	0.009(2)	-0.109(7)	2.6 (12)*
W1	0.94(2)	-0.5021(6)	0.0654(4)	0.371(2)	4.6(1)
W2	0.44(4)	-0.001(2)	0.163(2)	0.835(4)	7.90*
W3	0.31(3)	0.005(2)	0.078(2)	0.181(6)	7.90*
W4	0.31(2)	0.049(2)	0.313(1)	0.829(5)	7.90*
W5	0.32(2)	-0.050(2)	0.312(1)	0.827(5)	7.90*
W6	0.29(2)	-0.126(2)	0.027(2)	-0.142(6)	7.90*
W7	0.28(2)	-0.105(2)	-0.005(3)	-0.396(6)	7.90*
W8	0.27(2)	0.111(2)	0.024(2)	0.100(6)	7.90*
W9	0.20(2)	0.103(3)	-0.032(3)	0.140(8)	7.90*
W10	0.30(2)	0.001(2)	0.058(1)	0.433(3)	6.4(9)*
W11	0.18(1)	0.004(4)	0.274(2)	0.908(8)	7.90*
W12	0.16(2)	0.081(4)	-0.052(3)	-0.05(1)	7.90*
W13	0.33(4)	-0.093(2)	0.036(2)	-0.250(5)	8.1 (12)*
W14	0.30(3)	0.034(3)	0.077(2)	0.108(7)	7.90*
W15	0.21(2)	0.094(3)	0.051(2)	0.34(1)	7.90*
W16	0.33(2)	0.033(2)	0.073(2)	-0.377(4)	7.90*
W17	0.23(2)	-0.005(2)	0.105(2)	0.996(7)	7.90*
W18	0.10(2)	0.000(7)	0.392(6)	0.82(1)	7.90*
W19	0.13(2)	0.073(5)	0.047(4)	0.20(1)	7.90*
W20	0.22(1)	0.089(3)	0.064(2)	-0.106(7)	7.90*
W21	0.16(2)	0.122(4)	-0.018(4)	-0.024(9)	7.90*
W22	0.26(2)	0.125(2)	-0.007(2)	0.322(6)	7.90*
W23	0.35(2)	-0.095(1)	0.041(1)	-0.012(5)	7.90*

Table 4.9: Atomic coordinates and B_{eq} values for synthetic mordenite-Na; continued

<hr/>					
Bond		Bond		Bond	
<hr/>					
T1a - O6a	1.592(7)	T2a - O3a	1.604(3)	T3a - O4b	1.600(7)
T1a - O3b	1.595(3)	T2a - O2b	1.601(4)	T3a - O1a	1.620(5)
T1a - O1b	1.620(3)	T2a - O8(ave)	1.61(1)	T3a - O9	1.630(9)
T1a - O7a	1.614(7)	T2a - O5a	1.630(9)	T3a - O1b	1.652(5)
Mean	1.605	Mean	1.612	Mean	1.625
T1b - O3a	1.604(3)	T2b - O3b	1.603(3)	T3b - O1d	1.615(5)
T1b - O6a	1.618(7)	T2b - O5a	1.630(9)	T3b - O4a	1.630(8)
T1b - O1a	1.626(3)	T2b - O2a	1.626(4)	T3b - O9	1.629(9)
T1b - O7a	1.662(7)	T2b - O8 (ave)	1.66(1)	T3b - O1c	1.646(5)
Mean	1.627	Mean	1.631	Mean	1.630
T1c - O1c	1.621(3)	T2c - O8 (ave)	1.58(1)	T4a - O4a	1.599(7)
T1c - O7b	1.576(7)	T2c - O2d	1.602(4)	T4a - O2a	1.628(5)
T1c - O3c	1.612(3)	T2c - O3d	1.594(3)	T4a - O10	1.596(3)
T1c - O6b	1.631(7)	T2c - O5b	1.611(9)	T4a - O2b	1.630(4)
Mean	1.610	Mean	1.596	Mean	1.613
T1d - O7b	1.626(7)	T2d - O5b	1.568(9)	T4b - O2c	1.610(5)
T1d - O1d	1.632(3)	T2d - O3c	1.598(3)	T4b - O4b	1.624(7)
T1d - O6b	1.649(7)	T2d - O2c	1.625(4)	T4b - O10	1.638(3)
T1d - O3d	1.620(3)	T2d - O8 (ave)	1.60(1)	T4b - O2d	1.613(4)
Mean	1.632	Mean	1.597	Mean	1.621
<hr/>					
T - O - T angle	(°)	T - O - T angle		T - O - T angle	(°)
<hr/>					
T1b - O1a - T3a	145.4(3)	T3b - O4a - T4a		159.1(5)	
T1a - O1b - T3a	144.8(2)	T3a - O4b - T4b		160.4(5)	
T1d - O1c - T3b	145.3(2)	T2a - O5a - T2b		140.6(6)	
T1c - O1d - T3b	144.6(2)	T2c - O5b - T2d		149.6(6)	
T2b - O2a - T4a	144.4(2)	T1a - O6a - T1b		153.6(5)	
T2a - O2b - T4a	143.3(2)	T1c - O6b - T1d		143.8(5)	
T4b - O2c - T2d	143.4(2)	T1a - O7a - T1b		136.4(5)	
T2c - O2d - T4b	142.4(2)	T1d - O7b - T1c		143.1(5)	
T2a - O3a - T1b	158.8(3)	T2d - O8(av) - T2a		165(1)	
T1a - O3b - T2b	159.6(2)	T2b - O8(av) - T2c		153(1)	
T2d - O3c - T1c	159.8(3)	T3a - O9 - T3b		151.0(3)	
T2c - O3d - T1d	159.2(3)	T4a - O10 - T4b		153.9(3)	
<hr/>					

Table 4.10: T-O distances and T-O-T angles of Se-mordenite-Na

Bond		Bond		Bond	
T1a - O6a	1.614(6)	T2a - O3a	1.604(2)	T3a - O4b	1.632(7)
T1a - O3b	1.614(3)	T2a - O2b	1.594(3)	T3a - O1a	1.617(6)
T1a - O1b	1.629(4)	T2a - O8 (ave)	1.612(8)	T3a - O9	1.644(7)
T1a - O7a	1.593(6)	T2a - O5a	1.595(7)	T3a - O1b	1.667(5)
Mean	1.613	Mean	1.601	Mean	1.640
T1b - O3a	1.602(3)	T2b - O3b	1.595(3)	T3b - O1d	1.597(5)
T1b - O6a	1.649(6)	T2b - O5a	1.658(7)	T3b - O4a	1.598(5)
T1b - O1a	1.652(5)	T2b - O2a	1.623(3)	T3b - O9	1.617(7)
T1b - O7a	1.621(6)	T2b - O8 (ave)	1.612(8)	T3b - O1c	1.658(5)
Mean	1.631	Mean	1.622	Mean	1.618
T1c - O1c	1.583(5)	T2c - O8 (ave)	1.612(8)	T4a - O4a	1.636(5)
T1c - O7b	1.621(6)	T2c - O2d	1.594(3)	T4a - O2a	1.625(4)
T1c - O3c	1.614(3)	T2c - O3d	1.596(3)	T4a - O10	1.580(2)
T1c - O6b	1.596(6)	T2c - O5b	1.574(7)	T4a - O2b	1.654(4)
Mean	1.603	Mean	1.594	Mean	1.624
T1d - O7b	1.626(6)	T2d - O5b	1.613(7)	T4b - O2c	1.591(4)
T1d - O1d	1.616(5)	T2d - O3c	1.589(3)	T4b - O4b	1.590(7)
T1d - O6b	1.630(6)	T2d - O2c	1.625(3)	T4b - O10	1.660(3)
T1d - O3d	1.649(3)	T2d - O8(ave)	1.611(8)	T4b - O2d	1.621(4)
Mean	1.630	Mean	1.610	Mean	1.615

T - O - T angle	(°)	T - O - T angle	(°)
T3a - O1a - T1b	144.5(3)	T3b - O4a - T4a	162.6(4)
T1a - O1b - T3a	142.9(3)	T3a - O4b - T4b	165.7(3)
T3b - O1c - T1d	151.0(5)	T2a - O5a - T2b	141.6(6)
T1c - O1d - T3b	148.4(6)	T2d - O5b - T2c	157.2(2)
T2b - O2a - T4a	145.4(3)	T1a - O6a - T1b	146.78
T2a - O2b - T4a	144.4(6)	T1c - O6b - T1d	150.8(4)
T4b - O2c - T2d	142.9(5)	T1a - O7a - T1b	140.1(7)
T2c - O2d - T4b	141.9(4)	T1c - O7b - T1d	137.1(8)
T2a - O3a - T1b	159.2(5)	T2a - O8 - T2d	159.5(3)
T2b - O3b - T1a	159.1(3)	T2b - O8 - T2c	159.8(5)
T2d - O3c - T1c	158.5(2)	T3a - O9 - T3b	150.1(5)
T2c - O3d - T1d	158.4(5)	T4a - O10 - T4b	150.5(6)

Table 4.11: T-O distances and T-O-T angles of mordenite-Na

Atom	U_{11}	U_{22}	U_{33}	U_{12}	U_{13}	U_{23}
T1a	0.0105(9)	0.020(1)	0.0110(9)	0.0007(7)	0.0027(6)	0.0055(7)
T1b	0.0105(9)	0.020(1)	0.0110(9)	0.0007(7)	0.0027(6)	0.0055(7)
T1c	0.026(1)	0.0054(8)	0.011(1)	-0.0008(7)	-0.0035(7)	-0.0026(6)
T1d	0.026(1)	0.0054(8)	0.011(1)	-0.0008(7)	-0.0035(7)	-0.0026(6)
T2a	0.012(1)	0.014(1)	0.018(1)	-0.0001(7)	0.0000(8)	0.0013(9)
T2b	0.012(1)	0.014(1)	0.018(1)	-0.0001(7)	0.0000(8)	0.0013(9)
T2c	0.022(1)	0.017(1)	0.006(1)	-0.0068(8)	-0.0002(7)	0.0016(8)
T2d	0.022(1)	0.017(1)	0.006(1)	-0.0068(8)	-0.0002(7)	0.0016(8)
T3a	0.017(1)	0.016(1)	0.011(1)	-0.0055(8)	-0.0038(7)	0.0014(7)
T3b	0.017(1)	0.016(1)	0.011(1)	-0.0055(8)	-0.0038(7)	0.0014(7)
T4a	0.0050(8)	0.0111(9)	0.015(1)	-0.0056(7)	0.0038(7)	0.0010(7)
T4b	0.0050(8)	0.0111(9)	0.015(1)	-0.0056(7)	0.0038(7)	0.0010(7)
O1a	0.029(1)	0.047(2)	0.024(1)	0.026(2)	-0.001(1)	-0.001(2)
O1b	0.029(1)	0.047(2)	0.024(1)	0.026(2)	-0.001(1)	-0.001(2)
O1c	0.029(1)	0.047(2)	0.024(1)	0.026(2)	-0.001(1)	-0.001(2)
O1d	0.029(1)	0.047(2)	0.024(1)	0.026(2)	-0.001(1)	-0.001(2)
O2a	0.032(4)	0.025(3)	0.028(3)	0.005(2)	0.001(3)	0.011(2)
O2b	0.032(4)	0.025(3)	0.028(3)	0.005(2)	0.001(3)	0.011(2)
O2c	0.022(3)	0.044(4)	0.017(3)	0.014(2)	0.001(2)	0.010(2)
O2d	0.022(3)	0.044(4)	0.017(3)	0.014(2)	0.001(2)	0.010(2)
O3a	0.045(2)	0.031(2)	0.040(2)	0.019(2)	0.003(2)	-0.004(2)
O3b	0.045(2)	0.031(2)	0.037(2)	0.019(2)	-0.002(2)	0.006(2)
O3c	0.045(2)	0.031(2)	0.040(2)	0.019(2)	0.003(2)	-0.004(2)
O3d	0.045(2)	0.031(2)	0.037(2)	0.019(2)	-0.002(2)	0.006(2)
O4a	0.026(1)	0.027(1)	0.023(1)	-0.005(2)	0.001(1)	-0.004(2)
O4b	0.026(1)	0.027(1)	0.023(1)	-0.005(2)	0.001(1)	-0.004(2)
O5a	0.034(2)	0.058(3)	0.013(2)	-0.016(3)	0.000(1)	0.004(3)
O5b	0.034(2)	0.058(3)	0.013(2)	-0.016(3)	0.000(1)	0.004(3)
O6a	0.026(1)	0.027(1)	0.023(1)	-0.005(2)	0.001(1)	-0.004(2)
O6b	0.026(1)	0.027(1)	0.023(1)	-0.005(2)	0.001(1)	-0.004(2)
O7a	0.024(2)	0.015(2)	0.030(2)	0.001(1)	-0.005(1)	0.001(1)
O7b	0.024(2)	0.015(2)	0.030(2)	0.001(1)	-0.005(1)	0.001(1)
O9	0.019(2)	0.022(2)	0.041(2)	-0.008(2)	-0.002(2)	-0.001(3)
O10	0.019(2)	0.022(2)	0.041(2)	-0.008(2)	-0.002(2)	-0.001(3)
NA1	0.077(4)	0.041(4)	0.032(3)	-0.006(3)	0.002(2)	0.014(2)
W1	0.058(4)	0.075(5)	0.057(5)	0.016(8)	0.003(3)	0.010(7)

Table 4.12: Anisotropic displacement parameters U_{ij} of Se-mordenite-Na

Atom	U_{11}	U_{22}	U_{33}	U_{12}	U_{13}	U_{23}
T1a	0.0191(9)	0.0226(8)	0.0080(7)	0.0009(6)	-0.0032(6)	0.0019(6)
T1b	0.0191(9)	0.0226(8)	0.0080(7)	0.0009(6)	-0.0032(6)	0.0019(6)
T1c	0.0214(9)	0.0056(6)	0.0184(9)	-0.0014(5)	0.0029(7)	0.0018(6)
T1d	0.0214(9)	0.0056(6)	0.0184(9)	-0.0014(5)	0.0029(7)	0.0018(6)
T2a	0.0134(9)	0.0198(8)	0.014(1)	0.0065(7)	0.0021(8)	-0.0014(8)
T2b	0.0134(9)	0.0198(8)	0.014(1)	0.0065(7)	0.0021(8)	-0.0014(8)
T2c	0.023(1)	0.0146(8)	0.010(1)	-0.0014(7)	-0.0021(8)	-0.0011(7)
T2d	0.023(1)	0.0146(8)	0.010(1)	-0.0014(7)	-0.0021(8)	-0.0011(7)
T3a	0.0122(4)	0.0135(4)	0.0130(4)	0.0051(9)	0.0003(3)	-0.0028(8)
T3b	0.0122(4)	0.0135(4)	0.0130(4)	0.0051(9)	0.0003(3)	-0.0028(8)
T4a	0.0090(4)	0.0123(4)	0.0171(4)	0.0004(9)	0.0005(3)	0.0011(8)
T4b	0.0090(4)	0.0123(4)	0.0171(4)	0.0004(9)	0.0005(3)	0.0011(8)
O1a	0.021(3)	0.038(4)	0.043(4)	0.004(3)	-0.008(3)	0.018(3)
O1b	0.023(3)	0.039(4)	0.021(3)	-0.003(3)	0.002(2)	-0.026(3)
O1c	0.046(4)	0.068(5)	0.037(4)	-0.030(4)	0.016(3)	-0.022(4)
O1d	0.044(4)	0.064(5)	0.008(3)	-0.018(4)	-0.010(3)	0.004(3)
O2a	0.027(3)	0.062(4)	0.023(3)	0.003(2)	0.010(2)	0.009(2)
O2b	0.027(3)	0.062(4)	0.023(3)	0.003(2)	0.010(2)	0.009(2)
O2c	0.029(3)	0.027(3)	0.026(3)	0.007(2)	-0.009(2)	0.009(2)
O2d	0.029(3)	0.027(3)	0.026(3)	0.007(2)	-0.009(2)	0.009(2)
O3a	0.063(6)	0.047(5)	0.048(5)	0.022(4)	0.022(4)	-0.019(4)
O3b	0.060(5)	0.028(4)	0.081(6)	0.029(4)	0.013(5)	0.014(4)
O3c	0.052(5)	0.029(4)	0.051(5)	0.024(4)	-0.009(4)	0.000(4)
O3d	0.057(5)	0.046(5)	0.021(4)	0.022(4)	-0.012(3)	0.000(3)
O4a	0.012(3)	0.014(4)	0.042(4)	0.002(2)	0.005(3)	-0.012(3)
O4b	0.056(5)	0.015(4)	0.100(7)	0.004(3)	-0.014(5)	-0.016(4)
O5a	0.035(4)	0.080(6)	0.011(3)	-0.016(3)	0.002(3)	0.000(3)
O5b	0.049(5)	0.067(5)	0.015(3)	-0.045(4)	-0.008(3)	0.005(3)
O6a	0.043(4)	0.036(4)	0.018(3)	0.013(3)	-0.007(3)	0.003(3)
O6b	0.037(3)	0.026(3)	0.010(3)	0.023(3)	0.008(3)	0.008(2)
O7a	0.036(4)	0.003(3)	0.062(5)	-0.005(3)	0.011(3)	-0.006(3)
O7b	0.023(3)	0.035(4)	0.013(3)	0.007(3)	-0.010(2)	-0.008(3)
O9	0.012(2)	0.040(2)	0.036(2)	0.022(3)	-0.004(1)	-0.016(4)
O10	0.015(2)	0.028(2)	0.045(2)	-0.002(4)	0.000(1)	0.001(5)
NA1	0.076(3)	0.035(3)	0.023(3)	0.001(2)	0.000(2)	-0.009(2)
W1	0.062(4)	0.062(5)	0.049(3)	-0.041(5)	-0.001(3)	0.011(6)

Table 4.13: Anisotropic displacement parameters U_{ij} of Se-mordenite-Na

Bibliography

- [1] V.V. Poborchii, A.V. Kolobov, J. Caro, V.V. Zhuravlev, and K. Tanaka, “Polarized raman spectra of selenium species confined in nanochannels of $\text{AlPO}_4\text{-5}$ ”, *Chem. Phys. Lett.*, Vol. 69, p. 17–23, 1997.
- [2] A. Goldbach, L. Iton, and M.-L. Saboungi, “On the formation of isolated Se_8 rings in zeolites”, *Chem. Phys. Lett.*, Vol. 281, p. 69–73, 1997.
- [3] V.V. Poborchii, “Raman microprobe polarization-measurements as a tool for studying the structure and orientation of molecules and clusters incorporated into cubic zeolites: Se_8 and Se_{12} rings in zeolite A”, *J. Chem. Phys.*, Vol. 114, No. 6, p. 27007–27117, 2001.
- [4] W.M. Meier, “The crystal structure of mordenite”, *Zeit. Kristallogr.*, Vol. 115, p. 439–450, 1961.
- [5] W.M. Meier, *Natural Zeolites: Occurrence, Properties, Use*, Chapter Constituent Sheets in the Zeolite Frameworks of the Mordenite Group, p. 99–103, Pergamon Press, 1978.
- [6] T. Armbruster and M.E. Gunter, *Natural Zeolites: Occurrence, Properties, Applications*, Vol. 45 of *Reviews in Mineralogy and Geochemistry*, Chapter Crystal Structure of Natural Zeolites, p. 1–67, Mineralogical Society of America, 2002.
- [7] P. Cherin and P. Unger, “The crystal structure of trigonal Se”, *Inorg. Chem.*, Vol. 6, No. 8, p. 1589–1591, 1967.
- [8] V.N. Bogomolov, S.V. Kholodkevich, S.G. Romanov, and L.S. Agroskin, “The absorption spectra of single selenium and tellurium chains in dielectric matrix channels”, *Solid State Comm.*, Vol. 47, No. 3, p. 181–182, 1983.

- [9] V.N. Bogomolov, V.V. Poborchii, S.G. Romanov, and S.I. Shagin, "Raman spectra of chalcogen chains isolated in zeolite matrixes", *J. Phys. Chem: Solid State Phys.*, Vol. 18, No. 3, p. 313–317, 1985.
- [10] V.V. Poborchii, "Structure of one-dimensional selenium chains in zeolite channels by polarized raman scattering", *J. Phys. Chem. Solids.*, Vol. 55, No. 8, p. 737–743, 1994.
- [11] V.V. Poborchii, "Polarized raman and optical absorption spectra of the mordenite single crystals containing sulfur, selenium, or tellurium in the one-dimensional nanochannels", *Chem. Phys. Lett.*, Vol. 251, p. 230–234, 1996.
- [12] V.V. Poborchii, A.V. Kolobov, H. Qyanagi, S.G. Romanov, and T. Tanaka, "Structure of selenium incorporated into nanochannels of mordenite: dependence on ion exchange and method of incorporation", *Chem. Phys. Lett.*, Vol. 280, p. 10–16, 1997.
- [13] V.V. Poborchii, A.V. Kolobov, H. Qyanagi, S.G. Romanov, and T. Tanaka, "Raman and X-ray absorption study of selenium incorporated into the channels of mordenite: Dependence on the ion exchange and the method of incorporation", *Nanostruct. Mater.*, Vol. 10, No. 3, p. 427–436, 1998.
- [14] V.V. Poborchii, "Raman spectra of sulfur, selenium or tellurium clusters confined in nano-cavities of zeolite A", *Solid State Comm.*, Vol. 107, No. 9, p. 513, 1998.
- [15] V.V. Poborchii, A.V. Kolobov, J. Caro, V.V. Zhuravlev, and K. Tanaka, "Dynamics of single selenium chains confined in one-dimensional nanochannels of $\text{AlPO}_4\text{-5}$: Temperature dependencies of the first- and second-order raman spectra", *Phys. Rev. Lett.*, Vol. 82, No. 9, p. 1955–1958, 1999.
- [16] O. Terasaki, K. Yamazaki, J.M. Thomas, T. Ohsuna, D. Watanabe, and J.V. Sanders, "The incorporation of selenium into the channels of mordenite: An electron microscopic study", *J. Solid State Chem.*, Vol. 77, p. 72–83, 1988.
- [17] L. Khouchaf, M.-H. Tuilier, J.L. Guth, and B. Elouadi, "Atomic structure of selenium inserted in zeolites of the Na-mordenite type", *J. Phys. Solids*, Vol. 57, No. 5, p. 251–258, 1996.

- [18] J.B. Parise, J.E. Mac Dougall, N. Herron, R. Farlee, A.W. Sleight, Y. Wang, T. Bein, K. Möller, and L.M. Moroney, “Characterization of Se-loaded molecular sieves A, X, Y, AlPO-5, and mordenite”, *Inorg. Chem.*, Vol. 27, p. 221–232, 1988.
- [19] Y. Katayama, M. Yao, Y. Ajiro, M. Inui, and H. Endo, “Photo-induced phenomena in isolated selenium chains”, *J. Phys. Soc. Jap.*, Vol. 58, No. 5, p. 1811–1822, 1989.
- [20] A. Ikawa and H. Fukutome, “Electronic and lattice structures of isolated Se chains and defects in them. I. a semi-empirical model and properties of regular Se helix”, *J. Phys. Soc. Jap.*, Vol. 58, No. 12, p. 4517–4533, 1989.
- [21] A. Ikawa and H. Fukutome, “Electronic and lattice structures of isolated Se chains and defects in them. II”, *J. Phys. Soc. Jap.*, Vol. 59, No. 3, p. 1002–1016, 1990.
- [22] J. Warzywoda, A.G. Dixon, R.W. Thompson, and A.Jr. Sacco, “Synthesis and control of the size of large mordenite crystals using porous silica substrates”, *J. Mater. Chem.*, Vol. 5, No. 7, p. 1019–1025, 1995.
- [23] P. Simoncic and T. Armbruster, “Synthesis of mordenite single crystals for dye incorporation”, in *Zeolites '02, International Conference on the Occurrence, Properties and Utilization of Natural Zeolites*, P. Misaelides, Ed., 2002, Vol. Book of Abstracts, p. 336.
- [24] Oxford Diffraction, *CrysAlis Software Package 1.169, User Manual*, Xcalibur System, Oxfordshire, UK, 2001.
- [25] G.M. Sheldrick, *ShelX-97*, University of Göttingen, Germany, 1997.
- [26] P. Simoncic and T. Armbruster, “Peculiarity and defect structure of the natural and synthetic zeolite mordenite: A single-crystal X-ray study”, *Am. Mineral.*, Vol. 89, p. 421–431, 2004.
- [27] A. Alberti, P. Davoli, and G. Vezzalini, “The crystal structure refinement of a natural mordenite”, *Zeit. Kristallogr.*, Vol. 175, p. 249–256, 1986.
- [28] G. Lucovsky, A. Mooradian, W. Taylor, and G.B. Wright, “Identification of the fundamental vibrational modes of trigonal, α -monoclinic, and amorphous selenium”, *Solid State Comm.*, Vol. 5, p. 113–117, 1967.

- [29] M.H. Brodsky, *Ligth Scattering in Solids*, p. 208, Springer, Berlin, 1975.
- [30] A. Anderson, A. Sanders, and W. Smith, “Raman spectra of selenium dioxide at low temperatures”, *J. Raman Spec.*, Vol. 32, p. 403, 2000.
- [31] L-P. van Reeuwijk, *The Thermal Dehydration of Natural Zeolites*, Phd thesis, Landbouwhogeschool Wageningen, 1974.
- [32] A. Gottardi and E. Galli, *Natural Zeolites*, p. 223, Springer, Berlin, 1985.
- [33] J. Elsen, G.S.D King, and W.J. Mortier, “Influence of temperature on the cation distribution in calcium mordenite”, *J. Phys. Chem.*, Vol. 91, p. 5800–5805, 1987.
- [34] A. Martucci, M. Sacerdoti, and G. Cruciani, “Dehydration dynamics of mordenite by in-situ time resolved synchrotron powder diffraction study: A comparison with electrostatic site energy-calculations”, in *Zeolites and Mesoporous Materials at the Dawn of the 21st Century*, A. Galarnau, F. di Renzo, F. Faujula, and J. Verdine, Eds., 2001, Vol. 135 of *Studies in Surface Science and Catalysis*, p. 290.
- [35] A. Martucci, M. Sacerdoit, G. Cruciani, and C. Dalconi, “In situ time resolved synchrotron powder diffraction study of mordenite”, *Eur. J. Mineral.*, Vol. 15, p. 485–493, 2003.
- [36] W.M. Meier, R. Meier, and V. Gramlich, “Mordenite: Interpretation of a superposed structure”, *Zeit. Kristallogr.*, Vol. 147, p. 329, 1978.
- [37] K. Stahl, J.P. Legros, and J. Galy, “The crystal structure of SeO_2 at 139 and 286 K”, *Zeit. Kristall.*, Vol. 202, p. 99–107, 1992.

5 Cationic Thionin Blue in the Channels of Zeolite Mordenite: A Single-Crystal X-ray Study ¹

Petra Simoncic^a, Thomas Armbruster^a, Phil Pattison^b

Abstract

Single crystals of self-synthesized mordenite-Na were used for incorporation of the cationic dye molecule thionin blue ($C_{12}H_{10}N_3S^+$). The planar organic molecule ($7.5 \times 15 \text{ \AA}$), which fits into the large 12-membered ring channel of mordenite, was incorporated by ion-exchange replacing extraframework Na^+ cations. Deep blue thionin-exchanged mordenite crystals were chemically analyzed by electron microprobe yielding the composition $Na_{5.5}Thionin_{0.4}Si_{42.02}Al_{5.88}O_{96} \times nH_2O$ indicating that the large 12-membered ring channels of mordenite are less than half-filled by dye molecules. X-ray data collection of thionin-loaded mordenite single-crystals was performed at 120 K with synchrotron radiation ($\lambda = 0.80000 \text{ \AA}$) using the single-crystal diffraction line at the Swiss Norwegian Beamline, SNBL (ESRF, Grenoble) where diffracted intensities were registered with a MAR image plate. The structure of thionin-mordenite-Na was refined in the monoclinic space group Cc converging at $R1 = 5.53 \%$. Optical microscopy of dye-loaded mordenite single-crystals using plane-polarized light showed striking pleochroism due to anisotropic light absorption caused by the preferred orientation of the molecule's transition dipole-moment. Corresponding anisotropic phenomena were also observed by fluorescence microscopy. Four low populated thionin sites were located in the large mordenite channel. Determined S...O ($2.97(1) - 3.18(1) \text{ \AA}$), C...O ($3.11(1) - 3.36(2) \text{ \AA}$) and N...O ($3.04(1) - 3.20(1) \text{ \AA}$) distances from the dye molecule to the channel wall indicate electrostatic interaction with the framework. The molecules are arranged slightly inclined within the large 12-membered ring channels showing significant occupational disorder along the channel-axis. The flat geometry of the thionin-molecule enables a rotation of about 12° in each direction causing distinct disorder within the channel cross-section.

¹ ^aLab. für chem. und mineral. Kristallographie, ^bSwiss Norwegian Beamline (SNBL); ESRF, France. "Journal of Physical Chemistry B" (In press)

5.1 Introduction

Zeolites are characterized by open framework systems building channels and cavities with free apertures up to 13 Å in diameter. These channel systems are crucial for the properties and applications of zeolites, e.g. the well-established use as catalysts or molecular sieves. However, new and more sophisticated functions of zeolites in photochemistry emerged in the last decade. Host-guest systems built by photochromic, luminescent dyes intercalated into zeolites allow various applications as micro-lasers, pigments, optical switches or artificial antenna systems [1–3]. The well-defined internal structure of the zeolite framework provides the organization and arrangement of incorporated chromophores in terms of thermal or mechanical stabilization. Various zeolites with suitable channel dimensions as zeolite L [1, 2], $\text{AlPO}_4\text{-5}$ [4, 5], or zeolite Y [6], but also mesoporous materials as MCM-41 [7] have successfully been used for formation of these host-guest systems. Monomeric organized dyes in zeolites have striking optical effects as anisotropic light absorption or luminescence and fluorescence phenomena caused by the preferred orientation of the transition dipole-moment of the dye molecules.

Research on zeolite guest-host systems is generally focused on three areas: (1) incorporation processes of dye molecules into zeolites, (2) investigation of the energy transfer mechanism, and (3) geometrical characterization of the dyes within the zeolite framework.

Three different methods for dye incorporation have been established: (1) Ion-exchange: Cationic dye molecules as oxonine, pyronine, thionin, or methylene blue can be encapsulated into zeolites by ion-exchange in aqueous solution where extraframework metal -cations normally filling the zeolite channels are replaced by the charged dyes. (2) Vapor phase deposition: Neutral chromophores as fluorenone, naphthalene or anthracene can be inserted into a zeolite framework bringing the dyes into gas phase. Incorporation by gas phase requires a preceding dehydration of the zeolite because H_2O molecules block the pathway for the entering molecules. (3) In-situ encapsulation during zeolite synthesis where the photochromic molecules are added to the synthesis starting-materials and encapsulated during crystal growth.

Energy-transfer mechanisms in dye-modified zeolites were mainly investigated by the group of Calzaferri applying UV/VIS, fluorescence microscopy, and IR/Raman

spectroscopy [1, 2, 8–10]. They developed artificial antenna systems built by sophisticated arrangements of different dyes in zeolite L. Light falling onto the dye molecules in the zeolite channels is absorbed and the energy is transported by the dye molecules via the Förster energy-transfer mechanism. Zeolite-dye host-guest systems were designed consisting of pyronine (donor) and oxonine (acceptor) dyes placed within the channels and a stopcock molecule at the end of the channels to improve the functionality of the artificial antenna systems.

Relatively little is known about the alignment of the dye molecules in the zeolite frameworks, but a detailed structural characterization is of great importance for the understanding of the functionality of photochromic host-guest systems. The arrangement of molecules within the zeolite framework is defined by the free aperture of the channels (dimensions of 6–8 Å for 12-membered rings) as well as by the size and shape of the molecules. The molecules can be divided in three groups: (1) molecules small enough to rotate freely within the zeolite channels. (2) Middle-sized molecules for which it is difficult to guess how they arrange within the channels. (3) Long molecules, which align along the channel-axis. Rather bulky molecules can only be encapsulated into very large cages, as they exist in the zeolite faujasite or in mesoporous materials. Structural arrangement and localisation of photochromic dyes in zeolites are mainly investigated by optical microscopy, fluorescence microscopy, and X-ray diffraction methods.

Caro et al. [4] presented several methods for defining the positions of two different neutral guest-molecules in $\text{AlPO}_4\text{-5}$. Nanoporous $\text{AlPO}_4\text{-5}$ possesses a one-dimensional channel system running along the c -axis and forms hexagonal, elongated crystals. The arrangement of these molecules was tested by optical microscopy, Raman spectroscopy, second harmonic generation, and pyroelectric studies. Based on the results of these different methods, the authors postulated a preferred orientation of the guest-molecule along the channel-axis. Megelski et al. [10] derived a relationship between the orientation of cationic oxonine and pyronine in zeolite L and emitted light intensity recorded by polarized fluorescence microscopy. Cone-shaped distributions of the transition dipole-moment were defined for these two molecule with a cone half angle of 30° for pyronine, and 40° for oxonine, respectively, indicating a significant rotational disorder within the channel cross-section.

Alvaro et al. [11] encapsulated the photoluminescent polyphenyleneyinylene oligomer (PPV) into zeolite X and Y by in situ polymerization. The organic oligomers inside

the zeolites were characterized by diffuse reflectant UV/VIS, IR, and MAS ^{13}C NMR spectroscopy. The stability of PPV in zeolite X and Y is clearly enhanced so that this system can be used for laser flash photolysis.

Structural studies of dye-zeolite guest-host systems by X-ray diffraction are relatively rare. Van Koningsveld et al. [12] describe the positions of p-xylene in the 10-membered ring channels of zeolite H-ZSM-5. P-xylene was incorporated by gas phase and subsequently analysed by applying single-crystal X-ray diffraction. The authors reported a change in space group compared to the pure H-ZSM-5 phase and located two different preferred orientations of the p-xylene molecule within the ZSM-5 channel system. Hoppe et al. [6] investigated the incorporation of methylene blue into zeolite NaY by powder X-ray diffraction. They compared two different incorporation methods (ion-exchange, crystallization inclusion) resulting in two different preferred positions within the large cages of zeolite Y. Furthermore, they observed also a striking influence of the dye on the Na distribution.

Hennessy et al. [13] characterized the arrangement of methyl viologen (MV^{2+}) in zeolite L. They combined powder X-ray diffraction, IR and Raman spectroscopy and molecular modelling to localize the molecule within the framework. Due to the shape and size of the molecule and the aperture of the channels of zeolite L, they postulated a slightly inclined orientation of the molecule along the channel-axis. In addition, they used the zeolite framework vibrations recorded by IR and Raman spectroscopy as an internal standard for a non-destructive method to determine the degree of dye loading. Probably the first example of a composite material consisting of a silicate host and an organic guest (indigo) is Maya blue, first produced in the 8th century by the Mayas in Mexico. Using powder X-ray diffraction and molecular modelling, Chiari et al. [14] investigated the synthetic pigment Maya blue, a combination of the clay-mineral palygorskite and the organic dye indigo. Palygorskite possesses large channels with free dimensions of $7.3 \times 6.3 \text{ \AA}$ in which the dye molecule fits without steric impediments. The authors describe a formation of strong hydrogen bonds between the C=O group of the molecule and structural H_2O of the clay. Furthermore, they observed a six-fold disordered arrangement of the indigo molecule with in the clay channels.

In this study, mordenite was chosen for the structural study of incorporated cationic thionin blue because of the slightly oblate cross section of the large twelve-membered ring channels. In combination with the relatively low symmetry of mordenite (pseudo-

orthorhombic) the oblate cross-section of the channels suggested a more anisotropic orientation of the molecule compared to hexagonal zeolites, such as zeolite L. In hexagonal zeolites, the main channels run parallel to the six-fold axis and molecular disorder is therefore already predetermined by the symmetry of the tetrahedral framework. The structure of mordenite possesses large, ellipsoidal 12-membered ring channels (12MRc: free aperture $7 \times 6.5 \text{ \AA}$) and compressed 8-membered ring channels (8MRc: free aperture $5.7 \times 2.6 \text{ \AA}$) parallel to the *c*-axis (Fig. 3.1). These channels are connected by another set of compressed 8-membered ring channels parallel to the *b*-axis (Fig. 3.2 [15–17]). The mordenite structure at room temperature is usually refined in space group *Cmcm* or *Cmc2*₁, respectively [15, 18]. Simoncic and Armbruster [19] proposed a domain like structure where about 3% of the Si/Al framework is shifted by *c*/2. In spite of these studies, the symmetry of the framework is generally handled as pseudo symmetry and represents only a fair approximation. Lower symmetries or micro-twin models are also proposed [20] but not proven by experiments. As already shown in the structure refinement of pure mordenite-Na and a selenium-modified mordenite-Na at 120 K [21], the monoclinic space group *Cc* was used as a "best fit" for the agreement between structure model and diffraction data. Mordenite is divided in two groups: (1) large port mordenites, which can absorb molecules $> 4.5 \text{ \AA}$, and (2) small port mordenites, which can absorb only molecules $< 4.5 \text{ \AA}$ [22]. The large port character of the mordenite crystals used in this study has already been confirmed by the incorporation of Se chains with a length up to 10 \AA [21].

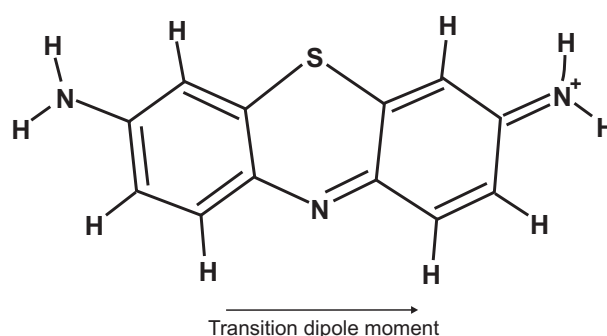


Figure 5.1: Cationic thionin molecule ($\text{C}_{12}\text{H}_{10}\text{N}_3\text{S}^+$). The planar organic molecule ($7.2 \times 15 \text{ \AA}$) fits into the large 12-membered ring channel of mordenite. Black arrow indicates the direction of the transition dipole moment.

Cationic thionin blue ($C_{12}H_{10}N_3S^+$), which was used for dye incorporation, is a sulfur-containing, single charged, flat molecule with dimensions of $7.2 \times 15 \text{ \AA}$ (Fig. 5.1). The focus of this single crystal X-ray study is the characterization of the arrangement of cationic thionin blue within the channels of the zeolite mordenite. The large ellipsoidal 12-membered ring channels along [001] with a free aperture of $7 \times 6.5 \text{ \AA}$ are tailor-made for incorporation of small organic dyes. Furthermore, the charge distribution on the internal walls of the zeolite channels may influence the orientation of the trapped molecules.

5.2 Experimental

5.2.1 Crystal synthesis

Pure mordenite-Na crystals were synthesized hydrothermally in the home lab after a modified method by Warzywoda et al. [23] The exact synthesis conditions are reported in Simoncic and Armbruster [19, 21]. The crystallization products were 100% mordenite with platy and uniform morphology. The run products were studied with a polarizing microscope and the single crystals were examined with a scanning electron microscope and showed well-defined, but slightly curved faces and no apparent twinning. Average size of the mordenite crystals was about $0.06 \times 0.04 \times 0.05 \text{ mm}$.

5.2.2 Dye incorporation

Self-synthesized mordenite-Na was used for encapsulation of cationic thionin blue. Dye incorporation was carried out by ion exchange. Pure Na-mordenite single crystals (0.5 g) were treated in $8 \times 10^{-2} \text{ M}$ aqueous thionin acetate solution ($C_{12}H_9N_3S \times C_2H_4O_2$, Aldrich, 90%) at $95 \text{ }^\circ\text{C}$ for 6 weeks in a sealed Teflon vessel. The stability of thionin blue in aqueous solution at boiling temperature was demonstrated experimentally by Calzaferri et al. [24]. In our experiment, the dye solution was renewed every week. After ion exchange crystals were extensively washed with distilled water and hydrochlorite solution (14%, Hänseler) to remove adsorbed molecules from the crystal surface.

For geometric reasons, the dye loading in the mordenite structure cannot exceed 1 molecule per formula unit. The periodicity of the mordenite c translation (7.5 \AA)

corresponds to the half-length of the molecule (15 Å). With two 12-membered ring channels per unit cell, this results in complete filling for 1 molecule per formula unit. Thionin-loaded mordenite was quantitatively determined by electron-microprobe analyses resulting in the composition $\text{Na}_{5.5}\text{Thionin}_{0.4}\text{Si}_{42.02}\text{Al}_{5.88}\text{O}_{96} \times n\text{H}_2\text{O}$, where the S-concentration was taken as measure of the thionin content. Furthermore, dye loaded mordenite single-crystals were investigated with plane-polarized light using an optical microscope determining the pleochroism, which is indicative of the orientation of the transition dipole-moment of the dye molecule.

5.2.3 X-ray data collection

X-ray data collection of synthetic mordenite-Na (as synthesized) and thionin blue-treated (thionin-mordenite-Na) single crystals were performed at 120 K using a conventional N₂ gas cooling device (Oxford cryosystems) and synchrotron radiation (wavelength $\lambda = 0.79946$ Å for mordenite-Na, $\lambda = 0.80000$ Å for thionin-mordenite-Na) on the single-crystal diffraction line at SNBL (ESRF, Grenoble) where diffracted intensities were registered with a MAR image plate. Wavelengths for both measurements were calibrated against a reference Si powder sample. The double experiments were performed to detect possible phase transitions in the mordenite structure at low temperature due to the influence of thionin incorporation. The reason for intensity data collection at low temperature was to reduce thermal vibration of extraframework dye molecules in order to allow more accurate localization. The diffraction data did not reveal diffuse features or superstructure reflections as could have been expected due to the relation between the periodicity of the mordenite *c* translation (7.5 Å) and the length of the molecule (15 Å).

Data reduction was performed with the program package CrysAlis [25] and an empirical absorption correction was made with Sadabs [26]. A summary of experimental parameters is given in Table 5.1. Structure refinement for mordenite-Na and thionin-mordenite-Na was carried out with the program SHELXL97 [27], using neutral-atom scattering factors (Si for all tetrahedral sites - labeled T sites). Refinements were performed with anisotropic displacement parameters for all framework sites. Previous structure refinement of pure mordenite-Na and Se-modified mordenite-Na at 120 K suggested space group *Cc* as an adequate model [21], because it led to an appropriate

description of the tetrahedral framework. Therefore final data for thionin-mordenite were also refined in this space group. In addition, a $c/2$ -shifted defect domain was introduced and fully constrained to the Si/Al framework [19, 21]. Coordinates of tetrahedral sites showing strong correlations were constrained to each other. Na- and H₂O positions were determined by comparison with diffraction data of synthetic mordenite at room temperature, analyzing interatomic distances and difference Fourier maps [19]. Thionin-molecule sites were determined comparing the difference-Fourier maps of the large 12-membered ring channel with corresponding electron density of the pure mordenite-Na. More details about the refinement of the Si, Al framework of mordenite-Na at 120 K can be found in Simoncic and Armbruster [21].

Sample	Mordenite-Na	Thionin-Mordenite-Na
Crystal size (mm)	0.05 × 0.04 × 0.50	0.06 × 0.05 × 0.03
Diffractometer	MAR image plate	MAR image plate
X-ray radiation	Synchrotron (0.79946 Å)	Synchrotron (0.80000 Å)
Temperature	120 K	120 K
Space Group	<i>Cc</i>	<i>Cc</i>
Cell dimensions (Å)	18.073(3), 20.463(3), 7.5145(9)	18.126(3), 20.403(2), 7.499(1)
β (°)	90.05(1)	90.02(2)
Absorption corr.	Sadabs	Sadabs
Maximum 2θ	55.13	58.53
Measured reflections	15595	18616
Index range	-20 ≤ <i>h</i> ≤ 20, -23 ≤ <i>k</i> ≤ 23, -8 ≤ <i>l</i> ≤ 8	-22 ≤ <i>h</i> ≤ 22, -24 ≤ <i>k</i> ≤ 24, -9 ≤ <i>l</i> ≤ 9
Unique reflections	4468	5205
Reflections > 4σ (F _o)	4180	4564
R _{int}	0.0347	0.0390
R _σ	0.0398	0.0350
Number of l.s. parameters	362	373
GooF	1.131	1.127
R1, F _o > 4σ (F _o)	0.0525	0.0549
R1, all data	0.0573	0.0621
wR2 (on F _o ²)	0.1095	0.1441

Table 5.1: Experimental parameters for X-ray data collection and refinement of mordenite-Na [21] and thionin-mordenite-Na.

5.3 Results

5.3.1 Structure of thionin-mordenite-Na

The unit cell of the thionin-modified sample shows a clear expansion of the a -axis and a shortening of the b -axis due to the incorporation of the flat organic molecule. Mean T-O bond lengths of thionin-mordenite-Na show within two standard deviations the same T-O distances as for pure mordenite-Na at 120 K [21]. Due to geometrical and space-filling considerations, the thionin molecule can only be incorporated into the large 12-membered ring channel. Molecule sites were identified by analyzing the difference Fourier map. The position of thionin can be best located by determining the position of the sulfur atom, because it has the largest scattering factor within the organic molecule. The sulfur site is clearly detectable on the difference Fourier map within the larger 12-membered channel along the c -axis (Fig. 5.2). The electron density of the thionin-loaded mordenite shows distinct peaks shifted $\pm x$ from the center of the 12-membered ring channel. These peaks were not found in the electron density map of the pure mordenite-Na but a weaker electron density distribution around the center of the channel is visible indicating disordered H₂O molecules in mordenite-Na [21].

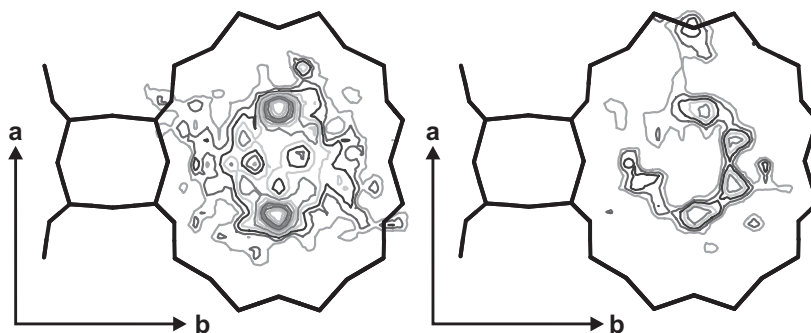


Figure 5.2: Difference Fourier maps of thionin-mordenite-Na and mordenite-Na, contours at 0.1 electron interval for both maps. Left: thionin-mordenite-Na, (001) section of the 12-membered ring channel at $z = 0.90$. Strong peaks shifted $\pm x$ from the center of the channel indicating the position of sulfur atoms. Smearred electron density around the center of the channel pointing to the presence of the thionin molecule. Right: mordenite-Na, (001) section of the 12-membered ring channel at $z = 0.90$. Electron density around the center of the large 12-membered channel is due to H₂O molecules.

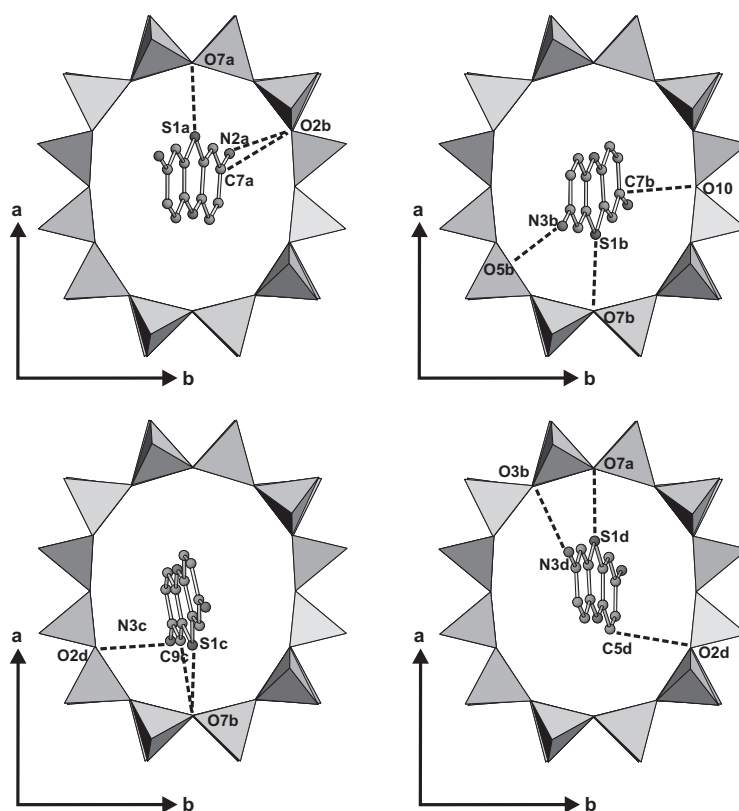


Figure 5.3: Thionin molecule sites within the large 12-membered ring channel showing inclined orientation within the channel cross-section. Shortest S...O, C...O and N...O distances from the molecules to the channel wall oxygens are indicated by dashed lines. H-atoms are not displayed.

Four different, partly occupied thionin sites are oriented slightly inclined along the channel-axis (Fig. 5.3). Two molecule sites were located at opposite positions at $x \approx \pm 0.1$ and $z \approx 0$, the other two at $x \approx \pm 0.1$ are separated by $c/2$ at $z \approx \pm 0.25$ (Fig. 5.4). Because the electron density peaks within the 12-membered ring channel indicated distinct disorder, the nearest neighbor and next nearest neighbor distances within the molecule were fixed during the refinement using bond lengths reported for methylene blue [28], and optimized with ChemSketch structure package [29]. S-C nearest neighbor distances were fixed to 1.73 - 1.74 Å, C-C distances to 1.35 - 1.49 Å, and N-C distances to 1.30 - 1.40 Å. All molecules were constrained to flat geometry. The population of individual atoms was constrained to be equal within one molecule. Isotropic displacement parameters for the sulfur-atom were free during the refinement whereas the displacement parameters of C- and N-atoms were fixed. Positions and

isotropic displacement parameters of H-atoms were not determined. Shortest S...O distance (2.97(1) Å) was determined between the sulfur-atom of molecule A (S1a) and channel wall oxygen O7b whereas the shortest N...O distance is between N3b (Molecule B) ...O5b and N3d (Molecule D)...O3b, both yielding 3.04(1) Å. Shortest C...O distance (3.11(1) Å) is between C9c (Molecule C) and O7b. Other short C...O and N...O distances and population parameters for each molecule are summarized in Table 5.2.

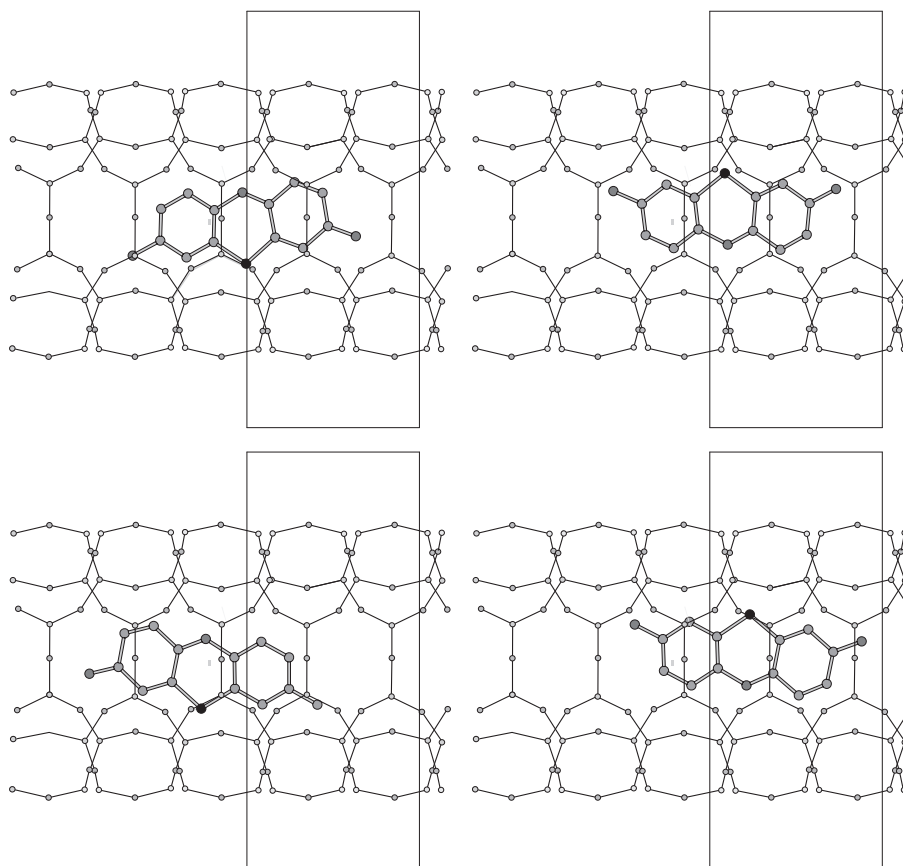


Figure 5.4: Thionin molecule sites within the large 12-membered ring channel along c . Unit cell dimensions are indicated by squares. Black dots represent the sulphur atom. Upper row: Molecules at $x \approx \pm 0.1$ and $z \approx 0$. Lower row: $x \approx \pm 0.1$ and $z \approx \pm 0.25$.

In the large 12-membered ring channel, besides the dye molecules, 5 H₂O sites and only 1 Na site were found. Two H₂O sites (population 0.2 - 0.5) were found in the center of the channel shifted along the b -axis, another set of H₂O molecules (popula-

S...O distances		Shortest N...O distances	
S1a - O7a	2.97(1) Å	N2a - O2b	3.07(2) Å
S1b - O7b	3.18(1) Å	N3b - O5b	3.04(1) Å
S1c - O7b	3.05(2) Å	N3c - O2d	3.20(1) Å
S1d - O7a	3.12(1) Å	N3d - O3b	3.04(1) Å
Shortest C...O distances		Molecules per formula unit	
C7a - O2b	3.27(1) Å	Molecule A	0.045(8) pfu
C7b - O10	3.20(2) Å	Molecule B	0.207(9) pfu
C9c - O7b	3.11(1) Å	Molecule C	0.098(6) pfu
C5d - O2d	3.36(1) Å	Molecule D	0.042(8) pfu

Table 5.2: Shortest S...O, C...O and N...O distances from the thionin-molecule to the channel wall oxygens. Concentrations are given in units per formula..

tion 0.21 -0.34) sites are also close to the center of the channel but shifted along the *a*-axis. One Na site (Na3, population 0.16) is also located in the center of the channel shifted along the *b*-axis. At the intersection between the large 12-membered channel and the 8-membered ring channel along the *b*-axis, as well as within the 8MR channel along *b*, additional H₂O and Na sites were found. Three Na sites (Na2, population 0.20; Na6, population 0.22, Na7, population 0.15) are close to the cross section of the 12MRc and 8MRb. Na3 (population 0.15) and Na4 (population 0.16) are close to the intersection of 8MRb and 8MRc. Another two H₂O molecules are found in the 8-membered ring channel along *b*. In the compressed 8-membered channel along the *c*-axis, Na1 (population 0.16) is coordinated by a highly populated H₂O site (population 0.5). The results of the structure refinement, including atomic coordinates, populations, and isotropic displacement parameters, as well as T-O distances and anisotropic displacement parameters, are given in Table 5.3 - 5.9 for the thionin-mordenite-Na sample. Crystallographic data for mordenite-Na at 120 K can be found in Chapter 4.

5.3.2 Optical microscopy

Striking pleochroism phenomena of the dye-loaded mordenite single-crystals were observed by optical microscopy using plane-polarized light. In Figs. 5.5a-d, the crystal orientation is indicated by the direction of the cell axes, polarization direction is shown

by a double-headed arrow. Figs. 5.5a and b show the (100) face of the mordenite crystal. The crystal appears blue, if the polarization direction is parallel to the c -axis (Fig. 5.5a), whereas the crystal is only slightly blue, if the polarization direction is parallel to the b -axis (Fig. 5.5b). Figs. 5.5c and d display the (001) face of the crystal, a section perpendicular to the large channels. With a polarization direction parallel to the a -axis, the crystal appears purple, while a polarizer orientation parallel to the b -axis shows a blue crystal.

These observations can be interpreted by the orientation of the thionin molecule's transition dipole-moment, which runs along the molecule's long axis [10]. If the electric field of the polarized light is oriented parallel to the transition dipole-moment (Fig. 5.5a), light is absorbed by the dye molecule and the crystal appears blue. On the other hand, the crystal appears only slightly blue, if the polarization direction is parallel to the b -axis (Fig. 5.5b). This indicates that the dye molecules within the channel are not exactly aligned parallel to the channel-axis but inclined regarding the channel cross-section. This assumption is also confirmed by the pleochroism observed in the crystal section perpendicular to the large channels (Figs. 5.5c and d). Light is also absorbed by the organic molecules in this alignment (blue, purple), which is only possible if the molecules are inclined within the channel cross section. If the molecules were arranged exactly upright in the channel, no light would be absorbed in this orientation and the crystal would appear colorless. In addition, the color change from blue to purple indicates a non-random orientation of the dyes within the channel cross-section. Corresponding phenomena can be observed by fluorescence microscopy of dye loaded mordenite single-crystals using plane-polarized light (Fig. 5.6a-d).

Fluorescence of the thionin molecules was excited using light from a 100 W mercury lamp passed through a U-MWIY excitation cube (wavelength 545-580 nm). Excited dye-loaded mordenite single-crystals emitted red light. The same crystal and polarization directions as for optical microscopy were applied, showing also anisotropic behavior of light emission. Intense red fluorescence is emitted, if the polarization direction is parallel to the c -axis whereas only very weak intensity appears, if the polarization direction is parallel to the b -axis (Figs. 5.6a and b, (100) orientation of the mordenite crystal). A difference in the fluorescence intensity is also observed at the (001) crystal orientation (Fig 5.6c and d): a polarization direction parallel to the a -axis shows a slightly more intense light emission (Fig. 5.6c) than with a polarization direction parallel to

the b -axis (Fig. 5.6d). The appearance of anisotropic fluorescence phenomena can be explained by the orientation of the transition-dipole moment of the thionin molecule as it was derived from the optical microscopy experiments.

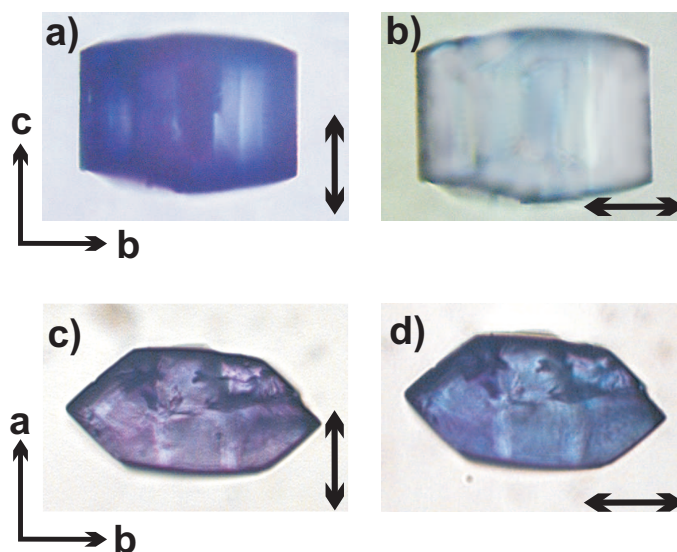


Figure 5.5: Optical micrographs of a dye-loaded mordenite single-crystal under plane-polarized light. 5.5a and b: (100) of the crystal. Crystal orientation is envisioned with the unit-cell axes, polarization direction with double-headed arrows. 5.5a shows a dark blue crystal under plane-polarized light parallel to the c -axis, 5.5b shows the same crystal with plane-polarized light parallel to the b -axis appearing only slightly blue. 5.5c and d shows a section perpendicular to the large channels ((001) face). Polarization direction parallel to the a -axis shows a purple crystal, parallel to the b -axis a blue crystal.

5.4 Discussion

5.4.1 The mordenite framework

Application of low temperature (120 K), chosen for an improved resolution of extraframework occupants and dye molecules, led also to a better resolution of the complex disordered microstructure within the tetrahedral framework. One has to assume that the refinement in space group Cc does not express the true framework symmetry

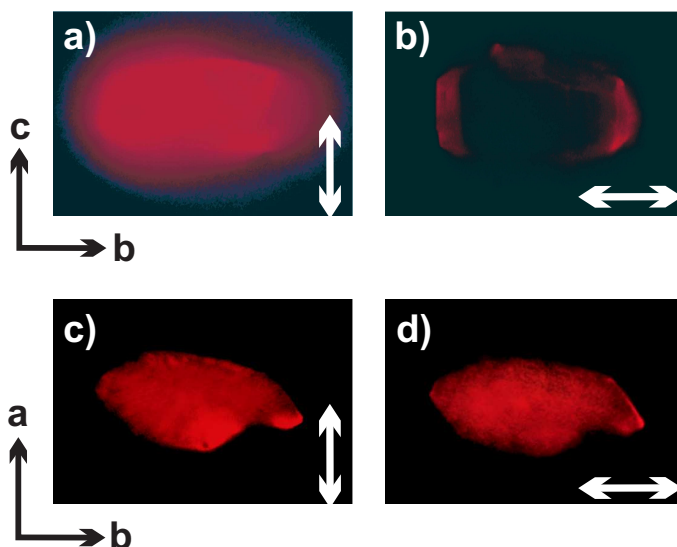


Figure 5.6: Fluorescence microscopic pictures of thionin-loaded mordenite single-crystals, excitation at 545-580 nm. 5.5a and b display the (100) crystal face. 5.5a shows intense light emission with polarization direction parallel to the c -axis. 5.5b shows only very weak emission with polarization direction parallel to the b -axis. 5.5c and d show a section perpendicular to the large channels. The polarization direction parallel to the a -axis shows more intense light emission (Fig. 5.5c) than with the polarizer parallel to the b -axis (Fig. 5.6d).

because lower symmetry or micro-twin models, as proposed by Gramlich-Meier [20], cannot be ruled out. Mordenite-Na, Se-mordenite-Na [19] as well as thionin-mordenite-Na have the same space group Cc in common; thus a phase transition caused by dye incorporation can be excluded.

5.4.2 Extraframework atoms

Extraframework Na and H_2O distribution of the thionin-loaded mordenite-Na is highly influenced by the incorporation of the organic molecule. By comparison with diffraction data of pure the mordenite-Na (Figs. 5.7, 5.8) [19], two points are remarkable: (1) the population of the Na sites is more uniformly distributed than in pure mordenite-Na, and (2) the large 12-membered ring channel is much less populated by Na than in pure mordenite-Na. It is striking that the Na1 site in the compressed 8-membered ring channel along the c -axis is populated with only 0.64 Na per formula unit (pfu) whereas this site is highly populated in mordenite-Na (2.28 Na pfu). In contrast, additional Na

sites (Na4, Na5, Na6, Na7) within the 8-membered channel along the b -axis were found, which do not occur in the pure mordenite-Na sample. As the organic thionin molecule is located in the large 12-membered ring channel, there are remarkable differences between the Na and H₂O extraframework distribution in the thionin-mordenite-Na and pure mordenite-Na. In mordenite-Na, 2.72 Na per formula unit were found in the large 12-membered ring channel along the c -axis whereas in the thionin-mordenite only 0.64 Na per formula unit are located in this channel.

Because the incorporation of cationic thionin blue is based on ion-exchange, part of the Na-ions located in the 12-membered ring channel were replaced or shifted towards the 8-membered ring channels along the b -axis, providing space for the entering organic molecule. Both the chemical analysis by electron microprobe and the structure refinement yielded about 0.42 thionin molecules per formula unit. To maintain charge balance this requires about 5.5 Na pfu, but in the structure refinement only 4.8 Na pfu were determined. This slight discrepancy can be explained by a more random distribution of the Na sites within the mordenite channels. Although only 0.4 Na pfu were replaced by thionin⁺, the entire Na distribution is influenced by the dye incorporation because the large 12-membered channels are filled by the large molecule which forces the extraframework cations to relocate at new positions.

In addition, the distribution of the H₂O molecules is influenced by the dye incorporation. Compared to 19 H₂O pfu in the pure Na-mordenite, only 10 H₂O pfu are present. In particular, only 6.5 H₂O pfu remained in this channel in the 12-membered ring channel of the thionin-exchanged mordenite, whereas 17 H₂O pfu are located in the pure mordenite-Na.

5.4.3 Arrangement of thionin blue in the mordenite channels

As most studies on dye-loaded zeolites were performed on zeolites with nearly circular shaped channel cross-sections (AlPO₄-5, zeolite L, zeolite Y) [4, 6, 10, 13] dye localization is hampered by the high, 6-fold symmetry of these channels. The circular channels and the shape of the incorporated molecules do not allow a preferred orientation, and the molecules arrange randomly within the channel cross section. This assumption is confirmed by fluorescence microscopy performed on dye-loaded zeolite L crystals building hexagonal, elongated columns [10]. Crystals lying on the column side (incident light

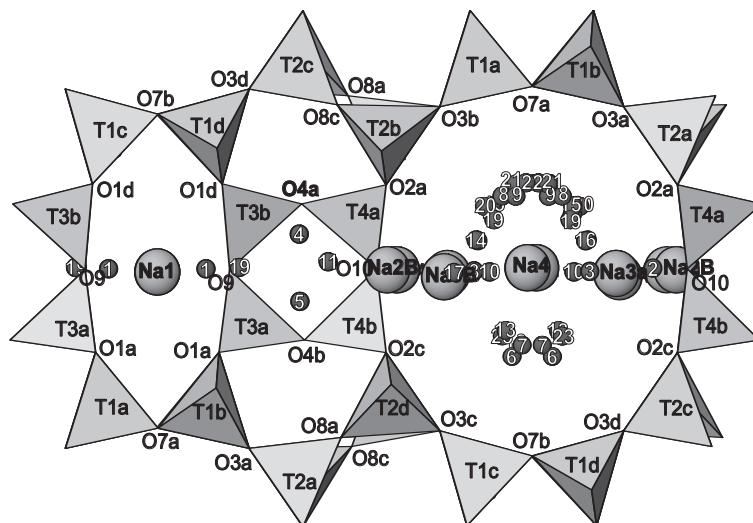


Figure 5.7: Extraframework cation and H_2O molecule positions in mordenite-Na. Small circles with numbers correspond to H_2O positions. Compare H_2O positions with electron density in Fig. 5.2

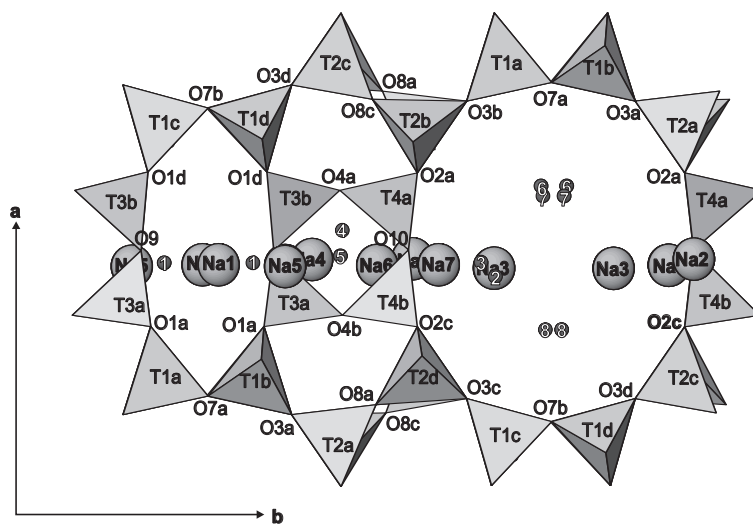


Figure 5.8: Extraframework cation and H_2O molecule positions in thionin-mordenite-Na. Small circles with numbers correspond to H_2O positions. Thionin molecule positions are not displayed. Note the Na sites shifted to the 8-membered ring channel along the b -axis, which do not appear in mordenite-Na.

perpendicular to the channel-axis) showed anisotropic light emission upon changing of the polarization direction whereas crystals standing on the hexagonal end faces (incident light parallel to the channel-axis) displayed radial distribution of light emission. This suggests that the transition dipole-moment of the dye molecules are fanned out radially perpendicular to the channel axis, and the molecules are not arranged in a preferred orientation.

The choice of a thionin-mordenite guest-host system should simplify the structural characterization and dye localization in two ways: (1) The anisotropic, ellipsoidal shape of the large 12-membered ring channel forces the molecule to arrange in a more ordered way. (2) The relatively heavy sulfur atom of the thionin-molecule is easily located by analyzing the difference Fourier map. In contrast, most studies mentioned above used dye molecules consisting of C, N and O, which are more difficult to localize in the relatively heavy matrix of the zeolite. On the other hand, due the shape and the size of the thionin molecule a slight rotational disorder of the molecule within the channel cross section has to be expected. Because the position of the sulfur atom can be assumed as well defined, as it was obvious from the difference Fourier map, the molecule can rotate around three axes defining a coordinate system with the S-atom as a center and axis parallel to the crystal's unit cell axes (Fig. 5.9).

This rotational disorder within the large 12-membered channels can be quantified using the minimum C...O (channel wall) and N...O distances. In a p-xylene loaded ZSM-5 [12], C...O distances from 3.16 to 3.68 Å were determined. Studies of interactions between CH-groups and H₂O molecules showed C...O distances around 3.3 Å [30]. Furthermore, N...O distances between NH₄⁺ ions and the cavities walls of the zeolite heulandite are 3.0 Å [31]. These reported distances are in good agreement with C...O and N...O distances yielded in this study, which are between 3.1 - 3.36 Å for C...O, and 3.04 - 3.2 Å for N...O respectively. Therefore, taking these minimum distances (C...O: 3.1 Å and N...O: 3 Å) into account, a rotation of the molecule (vibrational disorder) is limited. In particular, molecule positions with the molecule's long axis parallel to the *a*-axis, and *b*-axis respectively are not possible. Furthermore, a molecule orientation with the molecule's long axis parallel to the *c*-axis but with the molecule's plane parallel to (100) is not possible. Applying the AmiraMol visualization package [32], a maximum rotation of the molecule of about 12° in each direction with sulfur as a center of the above mentioned coordinate system, seems possible.

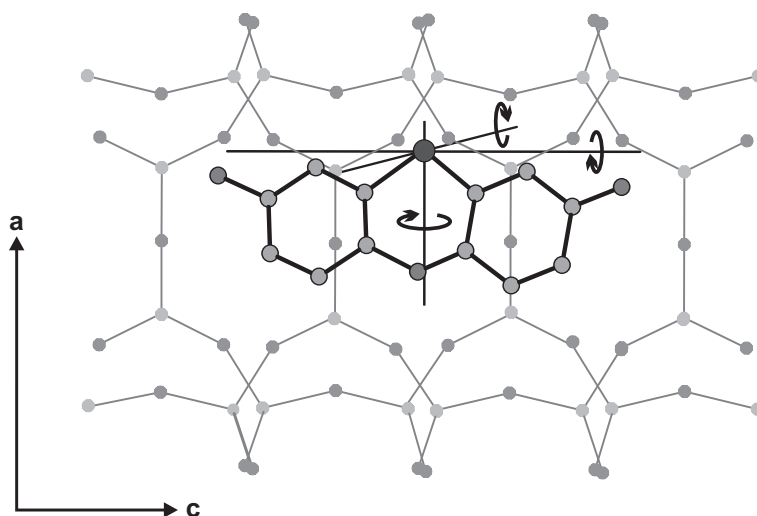


Figure 5.9: Thionin molecule within the large 12-membered ring channel long the c -axis. H-atoms are not shown. Possible rotation directions of the molecule are envisioned by a coordinate system with origin in the S-atom and axes parallel to the unit cell axes.

The molecule-framework distances are shorter than the sum of the van der Waals radii, suggesting electrostatic interaction between the molecule and the zeolite framework. The short C...O and N...O distances point to presence of relatively strong CH...O and NH...O hydrogen bonds, which is confirmed by the structural study of methyl viologen in zeolite L [13]. Finally, one can assume that the molecule even prefers an inclined position within the channel cross-section, because this results in the formation of stronger hydrogen bonding to the framework. In contrast, a hypothetical perfectly centered and upright orientation of the molecule along the channel-axis results in a C...O distance of 3.8 Å and a N...O distance of 3.88 Å suggesting considerably softer bonding to the framework than observed for the inclined orientation.

The refined inclined arrangements of the thionin-molecules are in good agreement with the observations made by optical and fluorescence microscopy. Appearance of light absorption and pleochroism observed at incident plane-polarized light parallel to the (001) crystal face can only be explained by an inclined arrangement of the dye molecule within the 12-membered ring channel. Furthermore, the pleochroic change from blue to purple indicates a partially ordered, non-random orientation of the dye within the channel cross section. In addition to the rotational disorder within the channel cross-section, there is also occupational disorder along the channel-axis, which

means that the four resolved sites of dye molecules are statistically occupied. This is supported by the non-observed diffuse features or superstructures in the diffraction data. Taking into account that the length of the molecule is twice the periodicity of the c-axis, the dye loading of 40% and missing superstructure reflections as well as non-observed diffuse scattering features indicate that the dye molecules are randomly anchored to specific framework sites.

The incomplete filling (ca. 40%) of the large mordenite channels with thionin may be explained by the applied temperature for dye incorporation. Dye incorporation at 95 °C suggests under these conditions strong dynamic translational and librational disorder of the dye molecules, leading to mutual repulsion of the cationic dye molecules along the channel-axis. This dynamic disorder was not observed in the X-ray experiment because the molecules were "frozen" at 120 K at energetically preferred channel sites. Nevertheless, significant disorder (librational and occupational) has been found for the four resolved dye-molecule orientations. It has been shown for zeolite L that a higher dye loading could be achieved if the dye incorporation experiments were carried out at room temperature [13, 33]. On the other hand, zeolite L crystals were about one order of magnitude smaller (particle size 0.2 - 0.5 μm) than the crystals used in this study (particle size 60 μm). Thus room-temperature exchange was possible due to the shorter diffusion path-ways. Ion exchange of thionin⁺ for 6 weeks at 95 °C reached equilibrium condition because no color or chemical zoning was detected parallel to the zeolite channel-axis (Figs. 5.5a and 5.6a).

We showed that the structural study of organic dyes in a zeolite with an oblate channel cross-section simplifies the localization of the guest-molecule and gives new insight into guest-host framework interactions. Single-crystal X-ray diffraction represents a powerful tool for a detailed characterization of guest-host systems and completes methods as IR, Raman or fluorescence spectroscopy also applied for guest-localization in zeolites.

5.5 Crystallographic data

Table 5.3 - 5.7: Atomic coordinates and B_{eq} values for synthetic thionin-mordenite-Na (space group Cc). ¹⁻³ coordinates with the same superscript were constrained to be equal. All atomic parameters (coordinates, population, isotropic displacement factors) labeled B are fully constrained and belong to a domain of mordenite shifted $c/2$ relative to the main part of the structure [19]. ^{a-d} Parameters of the thionin molecule-sites with the same superscript were constrained to be equal.

Starred atoms with standard deviation were refined isotropically, those without standard deviations were fixed. Anisotropically refined atoms are given in the form of the isotropic equivalent thermal parameter defined as $B_{eq} = 8/3 \pi^2 \sum_i (\sum_j (U_{ij} a_i^ a_j^* a_i \cdot a_j))$

Table 5.8: T-O distances (Å) and T-O-T angles of thionin-mordenite-Na with standard deviations in parentheses.

Table 5.9: Anisotropic displacement parameters U_{ij} of thionin-mordenite-Na.

Atom	Population	x	y	z	B_{eq} [\AA^2]
T1a	0.967(1)	0.3042(1)	0.0730(1)	0.1429(3)	1.46(3)
T1b	0.967(1)	0.3040(1)	-0.0728(1)	0.0567(3)	1.84(4)
T1c	0.967(1)	-0.3037(1)	0.0737(1)	0.1419(3)	1.37(3)
T1d	0.967(1)	-0.3036(1)	-0.0736(1)	0.0577(3)	1.77(4)
T2a	0.967(1)	0.1967(1)	0.1904(1)	0.6453(3)	1.61(4)
T2b	0.967(1)	0.19681(4) ¹	0.1902(1)	0.0554(3)	1.56(4)
T2c	0.967(1)	-0.19681(4) ¹	0.1899(1)	-0.3552(3)	1.45(4)
T2d	0.967(1)	-0.1971(1)	0.1897(1)	0.0561(3)	1.39(3)
T3a	0.967(1)	0.4139(1)	-0.11968(9)	0.3462(3)	1.45(3)
T3b	0.967(1)	-0.4140(1)	-0.1183(1)	0.3463(2)	1.32(3)
T4a	0.967(1)	0.08550(4) ²	0.2248(1)	0.3478(3) ³	1.61(3)
T4b	0.967(1)	-0.08550(4) ²	0.22479(9)	0.3478(2) ³	1.17(3)
O1a	0.967(1)	0.3780(4)	-0.0824(3)	0.175(1)	3.4(1)
O1b	0.967(1)	0.3788(4)	-0.0863(3)	0.533(1)	3.4(1)
O1c	0.967(1)	-0.3763(5)	-0.0892(4)	0.177(1)	4.6(2)
O1d	0.967(1)	-0.3763(4)	-0.0937(4)	0.5301(9)	3.9(1)
O2a	0.967(1)	0.1241(4)	0.1959(4)	0.177(1)	4.0(2)
O2b	0.967(1)	0.1223(4)	0.1972(4)	0.530(1)	3.5(2)
O2c	0.967(1)	-0.1236(4)	0.1907(3)	0.176(1)	2.9(1)
O2d	0.967(1)	-0.1218(4)	0.1921(3)	0.5311(9)	2.8(1)
O3a	0.967(1)	0.2360(5)	0.1192(3)	0.6088(9)	3.8(1)
O3b	0.967(1)	0.2328(4)	0.1214(3)	0.093(1)	4.0(2)
O3c	0.967(1)	-0.2386(5)	-0.1252(4)	0.594(1)	4.9(2)
O3d	0.967(1)	-0.2415(4)	-0.1224(4)	0.109(1)	4.5(2)
O4a	0.967(1)	-0.4056(5)	-0.1972(3)	0.361(1)	4.0(2)
O4b	0.967(1)	0.4069(4)	-0.1979(3)	0.363(1)	4.1(2)
O5a	0.967(1)	0.1729(5)	0.1950(3)	0.8507(9)	4.0(2)
O5b	0.967(1)	-0.1695(4)	0.1909(3)	-0.1497(9)	2.8(1)
O6a	0.967(1)	0.3276(3)	0.0800(3)	0.3484(8)	2.4(1)
O6c	0.967(1)	-0.3270(4)	0.0809(3)	0.3479(9)	3.0(1)
O7a	0.967(1)	0.2742(4)	0.0009(3)	0.1060(8)	2.3(1)
O7b	0.967(1)	-0.2757(3)	0.0011(3)	0.1063(8)	2.7(1)
O8a	0.967(1)	0.2498(6)	-0.2530(5)	0.101(1)	4.36(9)
O8b	0.967(1)	0.2519(6)	-0.2479(5)	-0.394(1)	4.24(9)
O9	0.967(1)	0.4986(4)	-0.0974(2)	0.350(1)	3.18(8)
O10	0.967(1)	0.0002(5)	0.2018(2)	0.359(1)	2.66(7)

Table 5.3: Atomic coordinates and B_{eq} values for synthetic thionin-mordenite-Na

Atom	Population	x	y	z	B_{eq} [\AA^2]
T1Ba	0.033(1)	-0.3042(1)	-0.0730(1)	0.1429(3)	2.37*
T1Bb	0.033(1)	-0.3040(1)	0.0728(1)	0.0567(3)	2.37*
T1Bc	0.033(1)	0.3037(1)	-0.0737(1)	0.1419(3)	2.37*
T1Bd	0.033(1)	0.3036(1)	0.0736(1)	0.0577(3)	2.37*
T2Ba	0.033(1)	-0.1967(1)	-0.1904(1)	0.6453(3)	2.37*
T2Bb	0.033(1)	-0.19681(4)	-0.1902(1)	0.0554(3)	2.37*
T2Bc	0.033(1)	0.19681(4)	-0.1899(1)	-0.3552(3)	2.37*
T2Bd	0.033(1)	0.1971(1)	-0.1897(1)	0.0561(3)	2.37*
T3Ba	0.033(1)	-0.4139(1)	0.11968(9)	0.3462(3)	2.37*
T3Bb	0.033(1)	0.4140(1)	0.1183(1)	0.3463(2)	2.37*
T4Ba	0.033(1)	-0.08550(4)	-0.2248(1)	0.3478(3)	2.37*
T4Bb	0.033(1)	0.08550(4)	-0.22479(9)	0.3478(2)	2.37*
O1Ba	0.033(1)	-0.3780(4)	0.0824(3)	0.175(1)	2.37*
O1Bb	0.033(1)	-0.3788(4)	0.0863(3)	0.533(1)	2.37*
O1Bc	0.033(1)	0.3763(5)	0.0892(4)	0.177(1)	2.37*
O1Bd	0.033(1)	0.3763(4)	0.0937(4)	0.5301(9)	2.37*
O2Ba	0.033(1)	-0.1241(4)	-0.1959(4)	0.177(1)	2.37*
O2Bb	0.033(1)	-0.1223(4)	-0.1972(4)	0.530(1)	2.37*
O2Bc	0.033(1)	0.1236(4)	-0.1907(3)	0.176(1)	2.37*
O2Bd	0.033(1)	0.1218(4)	-0.1921(3)	0.5311(9)	2.37*
O3Ba	0.033(1)	-0.2360(5)	-0.1192(3)	0.6088(9)	2.37*
O3Bb	0.033(1)	-0.2328(4)	-0.1214(3)	0.093(1)	2.37*
O3Bc	0.033(1)	0.2386(5)	0.1252(4)	0.594(1)	2.37*
O3Bd	0.033(1)	0.2415(4)	0.1224(4)	0.109(1)	2.37*
O4Ba	0.033(1)	0.4056(5)	0.1972(3)	0.361(1)	2.37*
O4Bb	0.033(1)	-0.4069(4)	0.1979(3)	0.363(1)	2.37*
O5Ba	0.033(1)	-0.1729(5)	-0.1950(3)	0.8507(9)	2.37*
O5Bb	0.033(1)	0.1695(4)	-0.1909(3)	-0.1497(9)	2.37*
O6Ba	0.033(1)	-0.3276(3)	-0.0800(3)	0.3484(8)	2.37*
O6Bb	0.033(1)	0.3270(4)	-0.0809(3)	0.3479(9)	2.37*
O7Ba	0.033(1)	-0.2742(4)	-0.0009(3)	-0.1060(8)	2.37*
O7Bb	0.033(1)	0.2757(3)	-0.0011(3)	0.1063(8)	2.37*
O8Ba	0.033(1)	-0.2499(6)	0.2528(5)	0.1006(1)	2.37*
O8Bb	0.033(1)	-0.2519(6)	0.2479(5)	-0.394(1)	2.37*
O9B	0.033(1)	-0.4986(4)	0.0974(2)	0.350(1)	2.37*
O10B	0.033(1)	-0.0002(5)	-0.2018(2)	0.359(1)	2.37*

Table 5.4: Atomic coordinates and B_{eq} values for synthetic thionin-mordenite-Na; continued

Atom	Population	x	y	z	B_{eq} [\AA^2]
NA1	0.159(9)	0.496(1)	0.008(1)	0.595(3)	3.1(4)*
NA2	0.20(2)	0.007(2)	-0.204(2)	0.332(5)	6.4(9)*
NA3	0.16(1)	0.001(2)	0.105(2)	0.999(5)	7.90*
NA4	0.15(2)	0.006(2)	0.350(2)	0.816(5)	7.7 (14)*
NA5	0.16(1)	-0.007(2)	0.394(1)	0.839(4)	4.0(7)*
NA6	0.22(1)	-0.002(1)	0.2562(8)	0.815(2)	5.6(6)*
NA7	0.14(2)	-0.002(2)	0.167(2)	0.805(4)	6.3 (11)*
W1	0.50(2)	-0.499(1)	0.0644(7)	0.327(2)	5.2(4)*
W2	0.21(3)	-0.021(3)	0.084(2)	0.089(7)	7.90*
W3	0.50(2)	-0.007(1)	0.087(1)	-0.367(3)	7.90*
W4	0.16(1)	0.053(3)	0.306(3)	0.831(8)	7.90*
W5	0.16(2)	0.012(3)	0.309(3)	0.965(8)	7.90*
W6	0.22(2)	0.126(2)	0.018(2)	0.850(6)	7.90*
W7	0.35(2)	0.109(1)	-0.015(2)	0.120(4)	7.90*
W8	0.34(2)	-0.108(1)	0.012(1)	-0.352(4)	7.90*
S1a	0.012(8) ^a	0.1108(5)	0.0056(2)	0.088(1)	3.8(42)*
C1a	0.012(8) ^a	0.0545(3)	0.0230(2)	0.267(1)	11.84* ^e
C2a	0.012(8) ^a	0.0522(5)	-0.0152(2)	-0.088(1)	11.84* ^e
C3a	0.012(8) ^a	-0.0237(5)	-0.0154(2)	-0.0664(8)	11.84* ^e
C4a	0.012(8) ^a	-0.0272(1)	0.0185(3)	0.250(1)	11.84* ^e
N1a	0.012(8) ^a	-0.0603(5)	0.00170(2)	0.1044(3)	11.84* ^e
C5a	0.012(8) ^a	-0.0727(5)	0.0340(3)	0.410(1)	11.84* ^e
C6a	0.012(8) ^a	-0.0366(3)	0.0515(3)	0.562(1)	11.84* ^e
C7a	0.012(8) ^a	0.0391(8)	0.0560(3)	0.580(2)	11.84* ^e
C8a	0.012(8) ^a	0.0852(7)	0.0407(3)	0.423(2)	11.84* ^e
N2a	0.012(8) ^a	0.0732(6)	0.07342	0.732(2)	11.84* ^e
C9a	0.012(8) ^a	0.0833(5)	-0.0316(3)	-0.251(1)	11.84* ^e
C10a	0.012(8) ^a	0.0379(2)	-0.0484(3)	-0.393(1)	11.84* ^e
C11a	0.012(8) ^a	-0.0379(2)	-0.0485(3)	-0.371(1)	11.84* ^e
C12a	0.012(8) ^a	-0.0689(5)	-0.0322(3)	-0.2087(6)	11.84* ^e
N3a	0.012(8) ^a	0.0681(9)	-0.0652	-0.560(2)	11.84* ^e

Table 5.5: Atomic coordinates and B_{eq} values for synthetic thionin-mordenite-Na; continued

Atom	Population	x	y	z	B_{eq} [\AA^2]
S1b	0.051(9) ^b	-0.1062(7)	0.0042(2)	-0.004(1)	5.9 (15)*
C1b	0.051(9) ^b	-0.0436(7)	0.0207(1)	0.164(1)	11.84* ^e
C2b	0.051(9) ^b	-0.0543(7)	-0.0148(1)	-0.193(1)	11.84* ^e
C3b	0.051(9) ^b	0.0222(7)	-0.0145(2)	-0.189(1)	11.84* ^e
C4b	0.051(9) ^b	0.0371(7)	0.0160(1)	0.1282(8)	11.84* ^e
N1b	0.051(9) ^b	0.0648(8)	0.0015(3)	-0.0256(2)	11.84* ^e
C5b	0.051(9) ^b	0.0892(6)	0.0319(2)	0.276(1)	11.84* ^e
C6b	0.051(9) ^b	0.0639(4)	0.0479(3)	0.438(1)	11.84* ^e
C7b	0.051(9) ^b	-0.0160(1)	0.0511(3)	0.471(1)	11.84* ^e
C8b	0.051(9) ^b	-0.0685(5)	0.0370(3)	0.326(1)	11.84* ^e
N2b	0.051(9) ^b	-0.0403(9)	0.0670(4)	0.632(2)	11.84* ^e
C9b	0.051(9) ^b	-0.0910(5)	-0.0302(2)	-0.350(1)	11.84* ^e
C10b	0.051(9) ^b	-0.0509(3)	-0.0455(3)	-0.503(1)	11.84* ^e
C11b	0.051(9) ^b	0.0254(2)	-0.0452(3)	-0.497(1)	11.84* ^e
C12b	0.051(9) ^b	0.0621(6)	-0.0298(3)	-0.341(1)	11.84* ^e
N3b	0.051(9) ^b	-0.0871(9)	-0.0613	-0.662(2)	11.84* ^e
S1c	0.025(6) ^c	-0.1160(5)	-0.00078	-0.2645(9)	2.1 (13) *
C1c	0.025(6) ^c	-0.0521(3)	-0.0005(1)	-0.435(1)	11.84 * ^e
C2c	0.025(6) ^c	-0.0679(5)	0.0195(2)	-0.0699(9)	11.84 * ^e
C3c	0.025(6) ^c	0.0073(5)	0.0321(3)	-0.073(1)	11.84 * ^e
C4c	0.025(6) ^c	0.0261(1)	0.0152(3)	-0.397(1)	11.84 * ^e
N1c	0.025(6) ^c	0.0511(5)	0.0293(3)	-0.238(1)	11.84 * ^e
C5c	0.025(6) ^c	0.0821(5)	0.0158(4)	-0.541(2)	11.84 * ^e
C5c	0.025(6) ^c	0.0646(6)	0.00237(5)	-0.710(2)	11.84 * ^e
C7c	0.025(6) ^c	-0.0160(8)	-0.0136(3)	-0.745(1)	11.84 * ^e
C8c	0.025(6) ^c	-0.0729(7)	-0.0145(3)	-0.604(1)	11.84 * ^e
N2c	0.025(6) ^c	-0.0323(3)	-0.0268(3)	-0.913(2)	11.84 * ^e
C8c	0.025(6) ^c	-0.1058(5)	0.0229(2)	0.0899(3)	11.84 * ^e
C10c	0.025(6) ^c	0.0443(5)	0.0481(4)	0.083(1)	11.84 * ^e
C11c	0.025(6) ^c	0.00686(4)	0.0516(4)	0.2447(9)	11.84 * ^e
C12c	0.025(6) ^c	-0.0686(4)	0.0389(3)	0.2447(9)	11.84 * ^e
N3c	0.025(6) ^c	-0.1066(8)	0.04254	0.409(1)	11.84 * ^e

Table 5.6: Atomic coordinates and B_{eq} values for synthetic thionin-mordenite-Na; continued

Atom	Population	x	y	z	B_{eq} [\AA^2]
S1d	0.011(8) ^d	0.1100(5)	0.00034	0.232(1)	3.0(53)*
C1d	0.011(8) ^d	0.0487(3)	0.0164(2)	0.406(1)	11.84* ^e
C2d	0.011(8) ^d	0.0569(5)	-0.0123(1)	0.042(1)	11.84* ^e
C3d	0.011(8) ^d	-0.0194(5)	-0.0089(3)	0.0471(8)	11.84* ^e
C4d	0.011(8) ^d	-0.0316(2)	0.0164(2)	0.368(1)	11.84* ^e
N1d	0.011(8) ^d	-0.0605(5)	0.0057(4)	0.2129(6)	11.84* ^e
C5d	0.011(8) ^d	-0.0844(5)	0.0307(3)	0.516(1)	11.84* ^e
C6d	0.011(8) ^d	-0.0566(5)	0.0409(4)	0.678(1)	11.84* ^e
C7d	0.011(8) ^d	0.0204(8)	0.0416(3)	0.716(1)	11.84* ^e
C8d	0.011(8) ^d	0.0738(7)	0.0282(3)	0.571(1)	11.84* ^e
N2d	0.011(8) ^d	0.0452(4)	0.0534(3)	0.881(2)	11.84* ^e
C9d	0.011(8) ^d	0.0922(5)	-0.0262(2)	-0.118(1)	11.84* ^e
C10d	0.011(8) ^d	0.0508(3)	-0.0365(2)	-0.272(1)	11.84* ^e
C11d	0.011(8) ^d	-0.0254(2)	-0.0329(3)	-0.265(1)	11.84* ^e
C12d	0.011(8) ^d	-0.0605(5)	-0.0192(4)	-0.1065(3)	11.84* ^e
N3d	0.011(8) ^d	0.0857(9)	-0.05061	-0.435(2)	11.84* ^e

Table 5.7: Atomic coordinates and B_{eq} values for synthetic thionin-mordenite-Na; continued

Bond	(Å)	Bond	(Å)	Bond	(Å)
T1a - O6a	1.605(7)	T2a - O2b	1.616(8)	T3a - O4b	1.606(9)
T1a - O3b	1.653(7)	T2a - O8b	1.641(1)	T3a - O1a	1.620(6)
T1a - O1b	1.606(6)	T2a - O3a	1.628(8)	T3a - O1b	1.682(7)
T1a - O7a	1.597(7)	T2a - O5a	1.600(6)	T3a - O9	1.606(7)
Mean	1.6215	Mean	1.621	Mean	1.628
T1b - O3a	1.606(6)	T2b - O5a	1.606(6)	T3b - O4a	1.616(6)
T1b - O7a	1.642(7)	T2b - O2a	1.598(9)	T3b - O9	1.635(6)
T1b - O1a	1.615(6)	T2b - O3b	1.657(7)	T3b - O1c	1.565(8)
T1b - O6a	1.634(7)	T2b - O8a	1.621(1)	T3b - O1d	1.627(7)
Mean	1.624	Mean	1.620	Mean	1.611
T1c - O6b	1.600(7)	T2c - O8a	1.601(9)	T4a - O4a	1.593(7)
T1c - O1d	1.611(6)	T2c - O3d	1.619(7)	T4a - O10	1.625(9)
T1c - O3c	1.623(7)	T2c - O2d	1.616(6)	T4a - O2a	1.578(6)
T1c - O7b	1.588(7)	T2c - O5b	1.613(6)	T4a - O2b	1.614(7)
Mean	1.606	Mean	1.612	Mean	1.603
T1d - O7b	1.574(6)	T2d - O3c	1.554(6)	T4b - O2c	1.563(6)
T1d - O1d	1.618(7)	T2d - O8b	1.561(1)	T4b - O2d	1.658(7)
T1d - O3d	1.567(7)	T2d - O5b	1.623(8)	T4b - O4b	1.602(7)
T1d - O6b	1.634(6)	T2d - O2c	1.599(7)	T4b - O10	1.615(9)
Mean	1.598	Mean	1.584	Mean	1.610
T - O - T	(°)	T - O - T	(°)		
T3a - O1a - T1b	145.5(5)	T3b - O4a - T4a	166.8(6)		
T1a - O1b - T3a	144.1(5)	T3a - O4b - T4b	167.7(6)		
T1d - O1c - T3b	152.2(6)	T2b - O5a - T2a	147.6(6)		
T1c - O1d - T3b	150.0(2)	T2d - O5b - T2c	144.2(5)		
T2b - O2a - T4a	149.2(6)	T1a - O6a - T1b	147.6(4)		
T2a - O2b - T4a	146.1(5)	T1c - O6b - T1d	148.2(5)		
T4b - O2c - T2d	143.3(4)	T1b - O7a - T1a	141.7(5)		
T4b - O2d - T2c	141.3(4)	T1d - O7b - T1c	142.3(5)		
T2a - O3a - T1b	152.5(4)	T2b - O8a - T2c	163.2(1)		
T2b - O3b - T1a	152.4(5)	T2a - O8b - T2d	164.1(1)		
T2d - O3c - T1c	162.4(6)	T3b - O9 - T3a	148.4(2)		
T2c - O3d - T1d	161.3(6)	T4a - O10 - T4b	145.9(3)		

Table 5.8: T-O distances (Å) and T-O-T angles of thionin-mordenite-Na

Atom	U_{11}	U_{22}	U_{33}	U_{12}	U_{13}	U_{23}
T1A	0.018(1)	0.024(1)	0.014(1)	0.0029(8)	0.0008(7)	0.0054(8)
T1B	0.032(1)	0.023(1)	0.015(1)	0.000(1)	0.0003(9)	0.0020(8)
T1C	0.020(1)	0.0147(9)	0.018(1)	-0.0035(8)	-0.0051(8)	0.0031(7)
T1D	0.036(1)	0.012(1)	0.019(1)	0.0004(9)	0.0026(9)	-0.0001(7)
T2A	0.027(1)	0.021(1)	0.012(1)	0.0038(9)	0.0033(9)	-0.0023(7)
T2B	0.021(1)	0.023(1)	0.015(1)	0.0004(8)	0.0054(9)	-0.0016(8)
T2C	0.022(1)	0.016(1)	0.016(1)	-0.0046(8)	-0.0055(9)	0.0002(7)
T2D	0.017(1)	0.019(1)	0.018(1)	-0.0002(8)	-0.0054(8)	-0.0051(7)
T3A	0.0157(9)	0.0152(9)	0.024(1)	0.0002(9)	0.0048(7)	-0.0006(8)
T3B	0.0161(9)	0.021(1)	0.0123(9)	-0.0016(9)	-0.0047(7)	0.0001(8)
T4A	0.016(1)	0.020(1)	0.025(1)	0.0037(9)	0.0008(8)	-0.0050(9)
T4B	0.0111(9)	0.0167(9)	0.0165(9)	-0.0001(9)	-0.0009(7)	-0.0043(8)
O1A	0.045(4)	0.042(3)	0.040(3)	-0.002(3)	-0.018(3)	0.012(3)
O1B	0.042(4)	0.052(4)	0.036(4)	0.000(3)	0.010(3)	0.004(3)
O1C	0.062(5)	0.085(6)	0.027(3)	-0.022(4)	0.021(3)	0.018(3)
O1D	0.053(4)	0.076(5)	0.022(3)	-0.029(4)	-0.016(3)	0.010(3)
O2A	0.030(4)	0.091(6)	0.031(4)	0.015(3)	0.015(3)	-0.017(3)
O2B	0.031(4)	0.073(5)	0.027(3)	-0.003(3)	-0.004(3)	0.016(3)
O2C	0.036(4)	0.042(4)	0.031(3)	0.014(2)	-0.016(3)	-0.013(2)
O2D	0.039(4)	0.038(3)	0.029(3)	0.020(2)	0.003(3)	0.013(2)
O3A	0.069(5)	0.034(4)	0.042(4)	0.017(3)	0.026(3)	-0.007(3)
O3B	0.071(5)	0.020(3)	0.059(4)	0.019(3)	-0.016(3)	0.004(3)
O3C	0.055(5)	0.045(4)	0.084(6)	0.031(4)	0.003(4)	-0.015(4)
O3D	0.038(4)	0.068(5)	0.065(5)	0.026(3)	-0.020(3)	0.020(4)
O4A	0.040(4)	0.018(3)	0.096(6)	0.003(2)	-0.027(4)	-0.002(3)
O4B	0.029(4)	0.022(3)	0.106(6)	0.003(3)	0.024(4)	0.001(3)
O5A	0.068(6)	0.071(5)	0.013(3)	0.026(4)	-0.007(3)	0.003(3)
O5B	0.031(4)	0.053(4)	0.024(3)	0.007(3)	0.007(3)	0.005(3)
O6A	0.041(4)	0.031(3)	0.020(3)	-0.008(3)	-0.007(3)	0.009(2)
O6B	0.049(4)	0.041(3)	0.025(3)	0.001(3)	0.004(3)	0.010(3)
O7A	0.037(3)	0.021(3)	0.031(3)	0.000(2)	0.010(2)	-0.008(2)
O7B	0.038(4)	0.027(3)	0.039(3)	0.000(3)	-0.010(3)	-0.012(3)
O8A	0.045(2)	0.047(3)	0.073(3)	0.028(2)	-0.012(2)	-0.026(2)
O8B	0.042(2)	0.050(2)	0.069(3)	0.025(2)	0.010(2)	0.027(2)
O9	0.020(2)	0.031(2)	0.071(3)	0.007(3)	-0.002(2)	-0.026(4)
O10	0.016(1)	0.028(2)	0.058(3)	0.001(3)	-0.001(1)	-0.005(3)

Table 5.9: Anisotropic displacement parameters U_{ij} of thionin-mordenite-Na.

Bibliography

- [1] G. Calzaferri, “Organic-inorganic composites as photonic antenna”, *Chimia*, Vol. 55, p. 1009–1013, 2001.
- [2] G. Calzaferri, M. Pauchard, H. Maas, S. Huber, A. Khatyr, and T. Schaafsma, “Photonic antenna system for light harvesting, transport and trapping”, *J. Mater. Chem.*, Vol. 12, p. 1–13, 2002.
- [3] I. Braun, M. Bockstette, G. Schulz-Ekloff, and D. Wöhrle, “Microwave-assisted crystallization inclusion of coumarin and azo dyes in AlPO₄-5 molecular sieves”, *Zeolites*, Vol. 19, p. 128–132, 1997.
- [4] J. Caro, F. Marlow, and M. Wüst, “Chromophore-zeolite composites: The organizing role of molecular sieves”, *Adv. Mater.*, Vol. 6, No. 5, p. 413–416, 1994.
- [5] G. Ihnlein, G. Schüth, O. Kraus, U. Vietze, and F. Laeri, “Alignment of a laser dye in the channels of AlPO₄-5 molecular sieve”, *Adv. Mater.*, Vol. 10, No. 14, p. 1117–1119, 1998.
- [6] R. Hoppe, G. Schulz-Ekloff, D. Wöhrle, C. Kirschhock, H. Fuess, L. Uytterhoeven, and R. Schoonheydt, “Incorporation of methylene blue in NaY zeolite at crystallographic defined positions”, *Adv. Mater.*, Vol. 7, No. 1, p. 61–64, 1995.
- [7] B. Onida, B. Bonelli, M. Lucco-Borlera, L. Flora, C. Otero Arean, and E. Garrone, “Spectroscopic properties of dye-loaded mesoporous silicas of the structural type MCM-41”, *Stud. Surf. Sci. Catal.*, Vol. 135, p. 364, 2001.
- [8] H. Maas and G. Calzaferri, “Constructing dye-zeolite photonic nanodevices”, *The Spectrum*, Vol. 16, No. 3, p. 18–23, 2003.

- [9] A. Devaux, C. Minkowski, and G. Calzaferri, “Electronic and vibrational properties of fluorenone in the channels of zeolite L”, *Chem. Eur. J.*, Vol. 10, p. 2391–2408, 2004.
- [10] S. Megelski, A. Lieb, M. Pauchard, A. Drechsler, S. Glaus, C. Debus, A.J. Meixner, and G. Calzaferri, “Orientation of fluorescent dyes in the nanochannels of zeolite L”, *J. Phys. Chem. B*, Vol. 105, p. 25–35, 2001.
- [11] M. Alvaro, A. Corma, B. Ferrer, M.S. Galletero, H. Garcia, and E. Peris, “Increasing the stability of electroluminescent phenylenevinylene polymers by encapsulation in nanoporous inorganic materials”, *Chem. Mater.*, Vol. 16, p. 2142–2147, 2004.
- [12] H. van Koningsveld, F. Tuinstra, H. van Bekkum, and J.C. Jansen, “The location of p-xylene in a single crystal of zeolite H-ZSM-5 with a new, sorbate-induced, orthorhombic framework symmetry”, *Acta Cryst B*, Vol. 45, p. 423–431, 1989.
- [13] B. Hennessy, S. Megelski, C. Marcolli, V. Shklover, C. Bärlocher, and G. Calzaferri, “Characterization of methyl viologen in the channels of zeolite L”, *J. Phys. Chem. B*, Vol. 103, p. 3340–3351, 1999.
- [14] G. Chiari, R. Giustetto, and G. Ricchiardi, “Crystal structure refinements of palygorskite and Maya Blue from molecular modelling and powder synchrotron diffraction”, *Eur. J. Mineral*, Vol. 15, p. 21–33, 2003.
- [15] W.M. Meier, “The crystal structure of mordenite”, *Zeit. Kristallogr.*, Vol. 115, p. 439–450, 1961.
- [16] W.M. Meier, *Natural Zeolites: Occurrence, Properties, Use*, Chapter Constituent Sheets in the Zeolite Frameworks of the Mordenite Group, p. 99–103, Pergamon Press, 1978.
- [17] T. Armbruster and M.E. Gunter, *Natural Zeolites: Occurrence, Properties, Applications*, Vol. 45 of *Reviews in Mineralogy and Geochemistry*, Chapter Crystal Structure of Natural Zeolites, p. 1–67, Mineralogical Society of America, 2002.
- [18] A. Alberti, P. Davoli, and G. Vezzalini, “The crystal structure refinement of a natural mordenite”, *Zeit. Kristallogr.*, Vol. 175, p. 249–256, 1986.

- [19] P. Simoncic and T. Armbruster, "Peculiarity and defect structure of the natural and synthetic zeolite mordenite: A single-crystal X-ray study", *Am. Mineral.*, Vol. 89, p. 421–431, 2004.
- [20] W.M. Meier, R. Meier, and V. Gramlich, "Mordenite: Interpretation of a superposed structure", *Zeit. Kristallogr.*, Vol. 147, p. 329, 1978.
- [21] P. Simoncic and T. Armbruster, "Se incorporated into zeolite mordenite-na: A single-crystal X-ray study", *Microporous Mesoporous Mater.*, Vol. 71, p. 185–198, 2004.
- [22] L.B. Sand, "Synthesis of large-pore and small-pore mordenites", in *Molecular Sieves*, 1968, Papers of Conference, Meeting Date 1967, p. 71–77.
- [23] J. Warzywoda, A.G. Dixon, R.W. Thompson, and A.Jr. Sacco, "Synthesis and control of the size of large mordenite crystals using porous silica substrates", *J. Mater. Chem.*, Vol. 5, No. 7, p. 1019–1025, 1995.
- [24] G. Calzaferri, D. Brühwiler, D. Megelski, M. Pfenniger, M. Pauchard, B. Hennessy, H. Maas, A. Devaux, and U. Graf, "Playing with dye molecules at the inner and outer surface of zeolite L", *Solid State Sci.*, Vol. 2, p. 421–447, 2000.
- [25] Oxford Diffraction, *CrysAlis Software Package 1.169, User Manual*, Xcalibur System, Oxfordshire, UK, 2001.
- [26] G.M. Sheldrick, *Sadabs 2.06: Empirical Absorption Correction Program*, University of Göttingen, Germany, 2002.
- [27] G.M. Sheldrick, *ShelX-97*, University of Göttingen, Germany, 1997.
- [28] H.E. Marr and J.M. Stewart, "The crystal structure of methylene-blue pentahydrate", *Acta Cryst. B*, Vol. 29, p. 847–853, 1973.
- [29] ACDlabs Freeware, *ChemSketch 5.0*, Advanced Chemistry Development Inc., Ontario, Canada, 2001.
- [30] T. Steiner, "Water molecules which apparently accept no hydrogen bonds are systematically involved in C-H-O interactions", *Acta Cryst D*, Vol. 51, p. 93–97, 1995.

- [31] P. Yang and T. Armbruster, “X-ray single-crystal structure refinement of NH₄-exchanged heulandite at 100 K”, *Eur. J. Mineral.*, Vol. 10, p. 461–471, 1998.
- [32] TGS visual concepts, *AmiraMol 3.1 (evaluation version)*, TGS visual concepts, California, USA, 2003.
- [33] G. Calzaferri and N. Gfeller, “Thionine in the cage of zeolite L”, *J. Phys. Chem.*, Vol. 96, p. 3428–3435, 1992.

6 Cationic Methylene Blue Incorporated into Zeolite Mordenite-Na: A Single-Crystal X-ray Study ¹

Petra Simoncic and Thomas Armbruster

Abstract

Single crystals of self-synthesized mordenite-Na were used for incorporation of the cationic dye molecule methylene blue (MB^+). Because the molecular size of MB^+ based on van der Waals radii ($7.0 \times 16 \text{ \AA}$) is close to the opening of the large 12-membered ring channel of mordenite ($6.5 \times 7 \text{ \AA}$), the molecule fits tightly into this channel. MB^+ was incorporated by ion-exchange in aqueous dye solution. The chemical composition of violet MB^+ -loaded mordenite crystals was determined by an energy dispersive (EDS) element analysis yielding $\text{Na}_{5.52}\text{MB}_{0.28}\text{Si}_{42.20}\text{Al}_{5.80}\text{O}_{96} \times n\text{H}_2\text{O}$. X-ray data collection of MB^+ -loaded mordenite single-crystals (MB -mordenite-Na) was performed at 120 K with synchrotron radiation ($\lambda = 0.79945 \text{ \AA}$) using the single-crystal diffraction line at the Swiss Norwegian Beamline, SNBL (ESRF, Grenoble) where diffracted intensities were registered with a MAR image plate. The structure of MB -mordenite-Na was refined in the monoclinic space group Cc converging at $R1 = 6.09 \%$. Structural data of MB -mordenite-Na were compared with a structure refinement of pure mordenite-Na also measured at 120 K. Furthermore, successful incorporation of MB^+ was confirmed with optical and fluorescence microscopy. Two partly occupied molecule sites were found in the large 12-membered ring channel; one oriented upright, the other slightly inclined within the channel cross section. The tight fit of the molecule in the mordenite channel results in relatively short C...O distances from the molecule to the zeolite framework, indicating hydrogen bonding and molecule-framework interaction. The incorporation of MB^+ also influences the extraframework Na and H_2O distribution, resulting in a strongly disordered arrangement.

¹Lab. für chem. and mineral. Kristallographie. Submitted to "Microporous Mesoporous Materials"

6.1 Introduction

The channels and cavities of a zeolite framework provide ideal space for the incorporation, stabilization and organization of complex species as organic, luminescent dyes, metal clusters or semiconductor materials. In particular, the intercalation of luminescent dye molecules into the structure of nanoporous molecular sieves enables the design of a new kind of advanced materials, e.g. nano-scaled electronic devices, microlasers, or artificial antenna systems. Neutral as well as cationic dye molecules were successfully incorporated into various zeolites such as zeolite L, AIPO-5 and zeolite Y (see [1] for a review).

Zeolite AIPO-5 modified with the cationic dye molecule methylene blue ($C_{16}H_{18}N_3S^+$) shows nonlinear optical properties (frequency doubling, spectral hole burning) (e.g. [2, 3]). Furthermore, methylene blue modified zeolite Y and mordenite find potential applications for data storage (e.g. [4]) or chemically modified electrodes [5, 6]. Furthermore, methylene blue (MB^+) organized in the channels of a zeolite shows distinct fluorescence emission explained by a Förster energy transfer mechanism [7, 8]. Two different methods were established for the encapsulation of cationic methylene blue into zeolite channels, (1) the incorporation by ion-exchange in aqueous dye-solution, (2) by adding the methylene blue as a template to the zeolite-synthesis batch [9].

Several studies on MB^+ loaded zeolites have been carried out to characterize the incorporation mechanism and dye arrangement using methods such as absorption spectroscopy, X-ray photoelectron spectroscopy and X-ray powder diffraction.

Hoppe et al. reported in several studies the incorporation and characterization of methylene blue in faujasite-type zeolite and AIPO-5 [9–11]. They described the encapsulation of MB^+ by ion-exchange and crystallization inclusion and performed X-ray photoelectron spectroscopy and X-ray powder-diffraction experiments on the MB^+ modified zeolites. They showed that MB^+ is located at two different sites within the faujasite-type zeolite depending on the incorporation method.

Calzaferri et al. performed kinetics experiments on the incorporation of thionin, methylene, and ethylene blue into zeolite L [12]. They demonstrated the successful incorporation of thionin blue into the channels of zeolite L, but failed to incorporate the larger molecules methylene and ethylene blue.

An electrochemical study of MB^+ intercalated into mordenite was reported by Ar-

vard et al. [5] and Zanjanchi et al. [6]. Based on diffuse reflectance spectroscopy, they reported monomeric and dimeric occurrence of methylene blue in the channels of mordenite and protonated MB^+ to MBH^{2+} by a hydration-dehydration process. Relatively little is known about the arrangement of MB^+ molecules in the zeolite frameworks, but a detailed structural characterization focusing on an accurate localization of the dye molecule and the bonding to the zeolite framework improves the understanding of the functionality of dye-loaded zeolites.

In this study, zeolite mordenite was chosen for the structural study of incorporated cationic methylene blue. The structure of mordenite can be described as built by edge-sharing 5-membered rings of tetrahedra (secondary building unit 5-1) forming chains along the *c*-axis [13]. However, the mordenite framework can also be more comprehensibly envisioned as formed by puckered sheets parallel to (100), assembled of six-membered rings of tetrahedra [14, 15]. These sheets are interlinked by four-membered rings (Fig. 4.1) in a way that large, ellipsoidal 12-membered (12MRc: aperture $7 \times 6.5 \text{ \AA}$) and strongly compressed 8-membered rings (8MRc: aperture $5.7 \times 2.6 \text{ \AA}$) define channels parallel to the *c*-axis. Another set of compressed 8-membered rings (8MRb: aperture $3.4 \times 4.8 \text{ \AA}$) connects the wide channels with the strongly compressed channels parallel to the *b*-axis.

Cationic methylene blue ($\text{C}_{16}\text{H}_{18}\text{N}_3\text{S}^+$), which was used for dye incorporation, is a sulfur-containing, single charged molecule with two methyl groups at each end of the molecule and a molecular size of $16 \times 7.0 \text{ \AA}$ based on van der Waals radii [9] (Fig. 6.1).

The aims of this study are: (1) Incorporation of MB^+ in self-synthesized, large mordenite single-crystals; (2) study of location and bonding of MB^+ in mordenite channels by single-crystal X-ray diffraction. The combination of the relatively low symmetry of mordenite (pseudo-orthorhombic) with the oblate cross-section of the channels suggested a more anisotropic orientation of the molecule compared to hexagonal or cubic zeolites, such as zeolite L or Y. The arrangement of dye molecules incorporated in the channels of zeolite L or Y exhibits usually pronounced disorder caused by the high symmetry of tetrahedral framework [11, 16, 17]. Because the molecular size of MB^+ based on van der Waals radii ($7.0 \times 16 \text{ \AA}$) is close to the pore opening of the large 12-membered ring channel of mordenite ($7 \times 6.5 \text{ \AA}$), the molecule fits tightly into the channel. This tight fit limits rotational disorder within the channel and simplifies

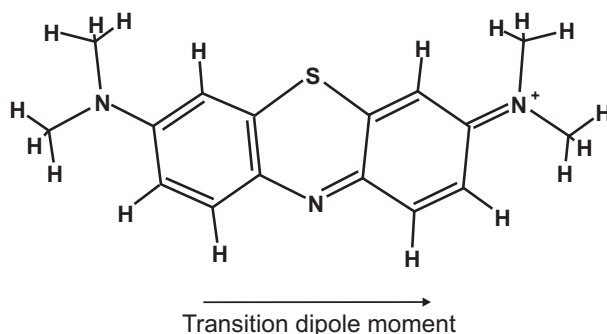


Figure 6.1: Cationic methylene blue molecule ($C_{16}H_{18}N_3S^+$). The organic molecule ($7.0 \times 16 \text{ \AA}$) fits into the large 12-membered ring channel of mordenite. Black arrow indicates the direction of the transition dipole moment.

the accurate localization of the molecule and characterization of molecule-framework interactions.

6.2 Experimental

Pure mordenite-Na single crystals for subsequent dye incorporation and X-ray diffraction experiments were hydrothermally synthesized after a modified method of Warzywoda et al [18]. This method uses preheated silica gel (Aldrich) and sodium aluminate (Riedel de Haen) as starting materials, which are dissolved in NaOH solution with the addition of a small amount of ethanol. Synthesis conditions were reported in detail elsewhere [19]. Synthesis products were 100% mordenite-Na with platy morphology and an average size of $0.05 \times 0.05 \times 0.06 \text{ mm}$. The crystals were examined under a scanning electron microscope and showed no twinning but slightly curved faces.

The self-synthesized mordenite-Na was used for encapsulation of cationic methylene blue (MB^+). The accessibility of the large 12-membered ring channels of the mordenite framework was demonstrated by previous incorporation experiments with elemental selenium [20] and cationic thionin blue [21]. Dye incorporation was carried out by ion exchange in an aqueous solution. Pure mordenite-Na single crystals (0.5 g) were treated in $8 \times 10^{-3} \text{ M}$ aqueous methylene blue trihydrate solution ($C_{16}H_{18}N_3S^+ \times 3H_2O$, Aldrich) at $90 \text{ }^\circ\text{C}$ for 12 weeks in a sealed Teflon vessel. The dye solution was renewed every week. After ion exchange, crystals were extensively washed

with hot distilled water and ethanol to remove adsorbed molecules from the crystal surface. The chemical composition of MB⁺-loaded mordenite was determined by energy-dispersive (EDS) element analysis using a scanning electron microscope yielding Na_{5.52}MB_{0.28}Si_{42.20}Al_{5.80}O₉₆ × nH₂O, where the S-concentration was taken as measure of the MB⁺ content.

Furthermore the incorporation of MB⁺ was confirmed by optical microscopy and fluorescence microscopy. MB⁺ loaded mordenite single-crystals were investigated with plane-polarized light using an optical microscope. Crystals were investigated in two settings: (1) incident beam perpendicular to the (001) face; (2) incident beam perpendicular to the (100) face. In setting (1), the crystal is violet, if the polarization direction is parallel to the a-axis. The crystal appears only light violet to nearly colorless with a polarization direction parallel to the b-axis. In setting (2), the crystal appears dark, nearly black with a polarization direction parallel to the c-axis. On the other hand, the crystal appears light violet to nearly colorless with a polarization direction parallel to the b-axis.

These pleochroism phenomena reflect the anisotropic arrangement with a relatively limited spreading of the molecules within the channel cross-section and can be explained by the orientation of the molecule's transition dipole moment, which runs along the molecule's long axis. The strong absorption (setting (1) parallel to the a-axis, setting (2) parallel to the c-axis) indicates a transition dipole moment nearly parallel to the polarization direction, whereas the weak absorption (setting (1) parallel to the b-axis, setting (2) parallel to b-axis) points to a nearly perpendicular orientation of the transition dipole moment to the polarization direction. Non-polarized fluorescence microscopy of the MB⁺ loaded mordenite crystals using a wave length of 545-580 nm results in intense emission of red light caused by the excited MB⁺ molecules.

X-ray data collection of synthetic mordenite-Na (as synthesized) and methylene blue-treated (MB-mordenite-Na) single crystals were performed at 120 K using a conventional N₂ gas cooling device (Oxford cryosystems) and synchrotron radiation (wavelength $\lambda = 0.79946 \text{ \AA}$) on the single-crystal diffraction line at SNBL (ESRF, Grenoble). The diffracted intensities were registered with a MAR image plate. The double experiments were performed to detect possible phase transitions in the mordenite structure at low temperature due to the influence of the incorporation of the dye molecule. The reason for intensity data collection at low temperature was to reduce thermal vibra-

tion and disorder of the extraframework dye molecules in order to allow more accurate localization. Data reduction was performed with the program package CrysAlis [22] and an empirical absorption correction was made with Sadabs [23]. A summary of experimental parameters is given in Table 6.1.

Structure refinement for mordenite-Na and MB-mordenite-Na was carried out with the program SHELXL97 [23], using neutral-atom scattering factors (Si for all tetrahedral sites - labeled T sites). Refinements were performed with anisotropic displacement parameters for all framework sites. The mordenite structure at room temperature is usually refined in space group $Cmcm$ [13] or $Cmc2_1$ [24], respectively. Simoncic and Armbruster [19] proposed a domain like structure where about 3% of the Si/Al framework is shifted by $c/2$. In spite of these studies, the symmetry of the framework is generally handled as pseudo symmetry and represents only a fair approximation. Lower symmetries or micro-twin models are also supposed [25] but not proven by experiments. As already shown in the structure refinement of pure mordenite-Na and selenium-modified mordenite-Na at 120 K [20], the monoclinic space group Cc was used as a "best fit" for the agreement between structure model and diffraction data of MB^+ loaded mordenite. Final data for MB-mordenite-Na are therefore presented in monoclinic space group Cc . In addition, a $c/2$ -shifted defect domain was introduced and fully constrained to the Si/Al framework. To reduce correlation problems due to pseudo symmetry, related tetrahedral sites were constrained to each other. Na- and H_2O positions were determined by comparison with diffraction data of synthetic mordenite-Na at room temperature [19] and 120 K [20], analyzing interatomic distances and difference Fourier maps. MB^+ -molecule sites were determined analyzing the difference Fourier map focusing on the large 12-membered ring channel, and in comparison with the electron density within the 12-membered ring channel of the pure mordenite-Na.

Two partly occupied MB^+ molecule sites were found. One site (molecule 1) is oriented nearly upright within the large 12-membered ring channel, whereas the other site (molecule 2) is slightly inclined within the channel cross-section (Fig. 6.2). Because the electron density peaks within the 12-membered ring channel indicated distinct disorder, the nearest neighbor and next nearest neighbor distances within the molecule were fixed during the refinement using bond lengths reported for methylene blue [26], and optimized with ChemSketch structure package [27]. S-C nearest neighbor distances

Sample	Mordenite-Na	MB-Mordenite-Na
Crystal size (mm)	0.05 × 0.04 × 0.05	0.06 × 0.04 × 0.05
Diffractometer	MAR image plate	MAR image plate
X-ray radiation	Synchrotron (0.7995 Å)	Synchrotron (0.7995 Å)
Temperature	120 K	120 K
Space Group	<i>Cc</i>	<i>Cc</i>
Cell dimensions (Å)	18.073(3), 20.463(3), 7.5145(9)	18.159(4), 20.349(4), 7.492(1)
β (°)	90.05(1)	90.03(1)
Absorption corr.	Sadabs	Sadabs
Maximum 2θ	55.13	55.12
Measured reflections	15595	15404
Index range	$-20 \leq h \leq 20, -23 \leq k \leq 23, -8 \leq l \leq 8$	$-20 \leq h \leq 20, -23 \leq k \leq 23, -8 \leq l \leq 8$
Unique reflections	4468	4390
Reflections $> 4\sigma(F_o)$	4180	4226
R_{int}	0.0347	0.0479
R_σ	0.0398	0.0444
Number of l.s. parameters	362	392
Goof	1.131	1.116
$R1, F_o > 4\sigma(F_o)$	0.0525	0.0609
$R1, all\ data$	0.0573	0.0630
wR2 (on F_o^2)	0.1095	0.1576

Table 6.1: Experimental parameters for X-ray data collection and refinement of mordenite-Na and MB-mordenite-Na

were fixed to 1.73 -1.74 Å, C-C distances to 1.35 - 1.49 Å, and N-C distances to 1.30 - 1.40 Å. The population of individual atoms was constrained to be equal for both molecules. Isotropic displacement parameters of S-, C- and N-atoms were fixed. All molecules were constrained to flat geometry, whereas the H-atoms are not included in the refinement. More details about the refinement of the Si, Al framework of mordenite-Na at 120 K can be found in Simoncic and Armbruster [20].

6.3 Results and Discussion

The results of the structure refinement for MB-mordenite-Na, including atomic coordinates, populations, and isotropic displacement parameters, as well as T-O distances and anisotropic displacement parameter, are given in Tables 6.3 - 6.8. Detailed structural data as atomic coordinates of mordenite-Na can be found in Chapter 4. In

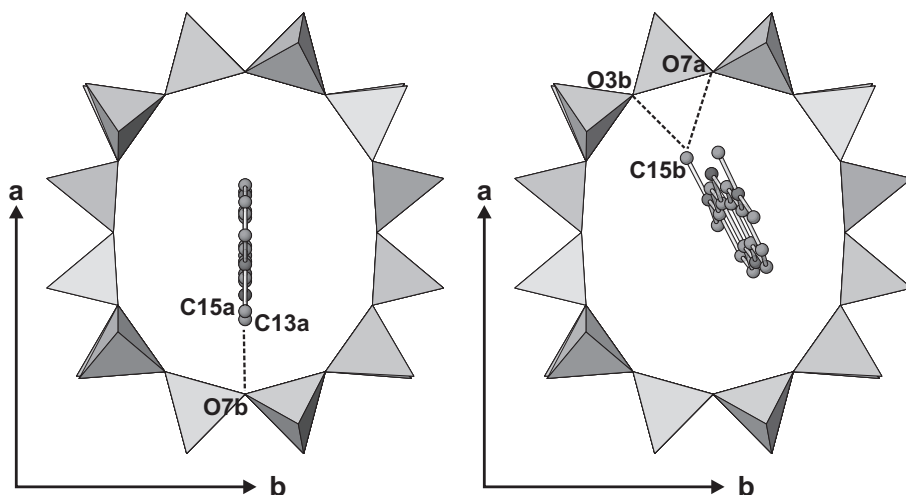


Figure 6.2: MB^+ molecule sites within the large 12-membered ring channel down c . Shortest $\text{C}\dots\text{O}$ distances from the molecules to the channel wall oxygens are indicated by dashed lines. H-atoms are not displayed.

comparison with the unit cell of mordenite-Na (Table 6.1), the unit cell dimensions of MB-mordenite-Na show a significant expansion along the a -axis and a shorting along the b -axis. The entering of the large MB^+ molecule with its methyl groups at each end of the molecule and the molecular size of $7 \times 16 \text{ \AA}$ (based on van der Waals radii) yields a slight compression of 12MRc along the b -axis. On the other hand the compressed 8-membered ring channel along c is slightly widened along the b -axis. This effect can also be envisioned by the ratio of the long axis to the short axis of the elliptic 12MRc and the compressed 8MRc. Taking the O7a - O7b distance (long axis) and the O10 - O10 distance (short axis) in 12MRc, the ratio for mordenite-Na is 1.05, whereas for MB-mordenite-Na it is 1.1, expressing a more compressed ellipse. The long axis/short axis ratio for 8MRc is 1.53 for mordenite-Na, and 1.49 for MB-mordenite-Na.

The distribution of extraframework occupants (Na^+ , H_2O) differs significantly from the corresponding distribution in mordenite-Na. Na cations in mordenite-Na are mainly concentrated on 4 sites (Fig. 6.3a); a highly occupied site (Na1) in the center of the compressed 8-membered channel along c , 3 less occupied sites within the 12-membered ring channel along c (Na2, Na3, Na4), where Na2 is positioned at the intersection to the 8-membered ring channel along b . Most surprisingly, the highly occupied Na1 in mordenite-Na is only low populated in MB-mordenite-Na. Furthermore, the Na

population in the large 12MRc is reduced, and new, also low populated Na sites are found in 8MRb (Fig. 6.3b). The Na content determined in the structure refinement (4.02 Na per formula unit (pfu)) differs significantly from the analysed Na content (5.52 Na pfu). This points to a strongly disordered Na distribution caused by the incorporation of MB^+ , situated in the large 12-membered channel. By entering the large 12MRc, the bulky dye molecule displaces the channel occupants and shifts them partly to the connecting channel along b. Most H_2O molecules in the large 12MRc are missing, and only 6 H_2O are left (Fig. 6.3). Because of the strongly disordered distribution, it must be assumed that Na and H_2O sites cannot be clearly distinguished (similar scattering power, similar distance to the channel walls).

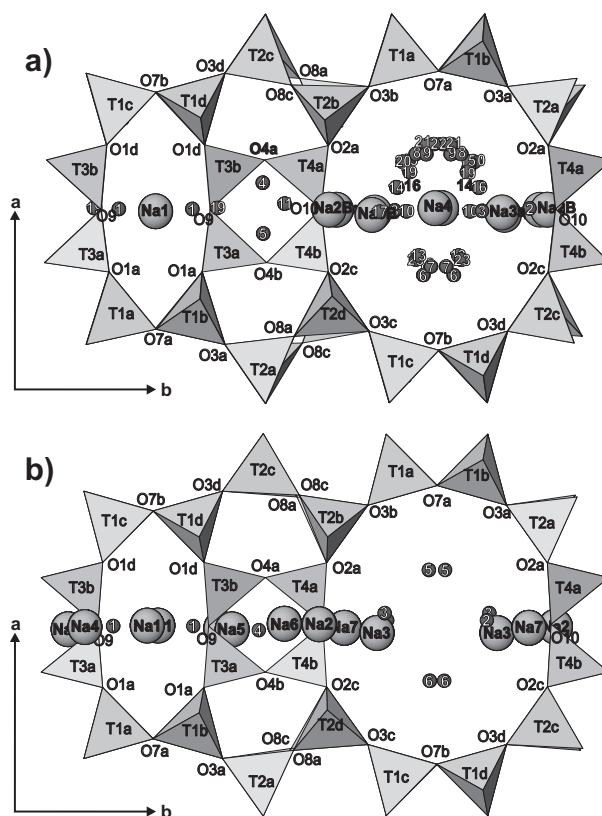


Figure 6.3: a) Tetrahedral framework and extraframework cations and H_2O molecules of mordenite-Na. b) Tetrahedral framework and extraframework cations and H_2O molecules of MB-mordenite-Na. Black circles with white numbers are H_2O positions

The two molecule sites localized in the 12-membered ring channel led to 0.26 MB^+

per formula unit. Thus, the chemical analysis of 0.28 MB⁺ per formula unit (pfu) is in good agreement with the dye content determined in the structural refinement. 0.28 MB⁺ pfu represents less than 30% loading of the mordenite channels. The periodicity of the mordenite *c* translation (7.5 Å) corresponds to nearly the half-length of the MB⁺ molecule (16 Å). With two 12-membered ring channels per unit cell, this results in theoretical complete filling for 0.93 molecules per formula. The dye loading of less than 30% indicates a disordered molecule arrangement within the mordenite channels. This assumption is supported by the diffraction data where no diffuse scattering or superstructure reflections were detected.

Although the structure refinement was performed in space group *Cc*, the mordenite framework exhibits topological symmetry *Cmcm* with a 2₁ axis passing through the center of the large 12MRc channels, a mirror plane perpendicular to the crystal's *c*-axis and a mirror plane parallel to (100). On the first glance these requirements imposed by pseudo-symmetry do not agree with the results of the structure refinement where one MB⁺ site is oriented upright and the other is opposite to the first one, shifted *c*/2, and slightly inclined to the 12MRc channel. The two resolved MB⁺ sites are approximately related by a 2₁ axis. The missing symmetry equivalent positions (relative to the topological symmetry) should not be taken as proof for an acentric MB⁺ arrangement within a pseudo-centrosymmetric channel environment. We consider this as an artifact caused by severe correlations in the diffraction data due to a low symmetry refinement (*Cc*) of a structure with high topological symmetry (*Cmcm*). If four fully constrained MB⁺ molecules are introduced in the 12MRc channels according to the topological symmetry, the populations of these molecules are highly correlated and cannot simultaneously be refined. Therefore the populations of the two refined molecules were constrained to be equal. In other words, we cannot distinguish centrosymmetric and acentric MB⁺ arrangement.

The most appropriate interpretation of the MB⁺ distribution based on our diffraction data is as following. The inner surface of the mordenite 12MRc channels exhibits preferred positions for the attachment of MB⁺ (Fig. 6.4). This means that the mordenite channels cannot be filled by continuous stacks of MB⁺ along *c* where the MB⁺ separation would be dictated by van der Waals contacts. Such an hypothetical arrangement would probably be incommensurate with the available docking sites on the channel surface. Because the topological symmetry requires that the preferred MB⁺

sites are separated by $c/2$ one may assume from Fig. 6.4 that two closely spaced MB^+ molecules find space in four translations of the host structure along c if the adjacent molecules are rotated 180° around the channel axis to prevent short inter-molecular contacts. One should also consider that the two resolved MB^+ sites in the structure refinement were obtained by very rigid constraints concerning inter-atomic distances and isotropic displacement parameters. Thus we question whether the resolved molecule positions are actually two independent sites or rather an indication of severe librational disorder of the up-right orientation with continuous variations.

Shortest S...O, N...O and C...O distances from the MB^+ molecules to the mordenite framework are summarized in Table 6.2. Compared with literature data, where C...O distances of 2.8 - 3.3 Å [16, 28] are reported, the C...O distances (2.83 - 3.02 Å) in this study are relatively short, indicating CH...O hydrogen bonding from the molecules to the mordenite framework. Calculated hypothetical H-atom coordinates using CH3 and CH constrains resulted in CH...O distances around 2.12 Å with C-H-O angles of 145° for the shortest contacts to the mordenite framework, e.g. for the C15b-H-O7a group. These calculated H sites were not included in the refinement.

Molecule 1		Molecule 2	
S1a - O7b	3.09(1) Å	S1b - O7a	3.17(1) Å
N1a - O7a	3.84(1) Å	N1b - O2c	2.99(1) Å
C13a - O7b	2.86(1) Å	C15b - O7a	3.02(1) Å
C16a - O7b	2.83(2) Å	C15b - O3b	2.83(1) Å

Table 6.2: Shortest S...O, C...O and N...O distances from the MB molecule to the channel wall oxygens.

Partial demethylation of MB^+ to the neutral trimethylthionin (removal of a CH_3 group) has been reported at high pH and high temperature [29], and was also postulated in an X-ray powder diffraction experiment on MB^+ modified NaY [11], where the sample was heated to 200°C . Although in our study, MB^+ was incorporated at 90°C , it can be assumed that MB is not present as neutral demethylated TMT. The demethylation of MB^+ to TMT is described as a base catalyzed reaction of MB^+ at the

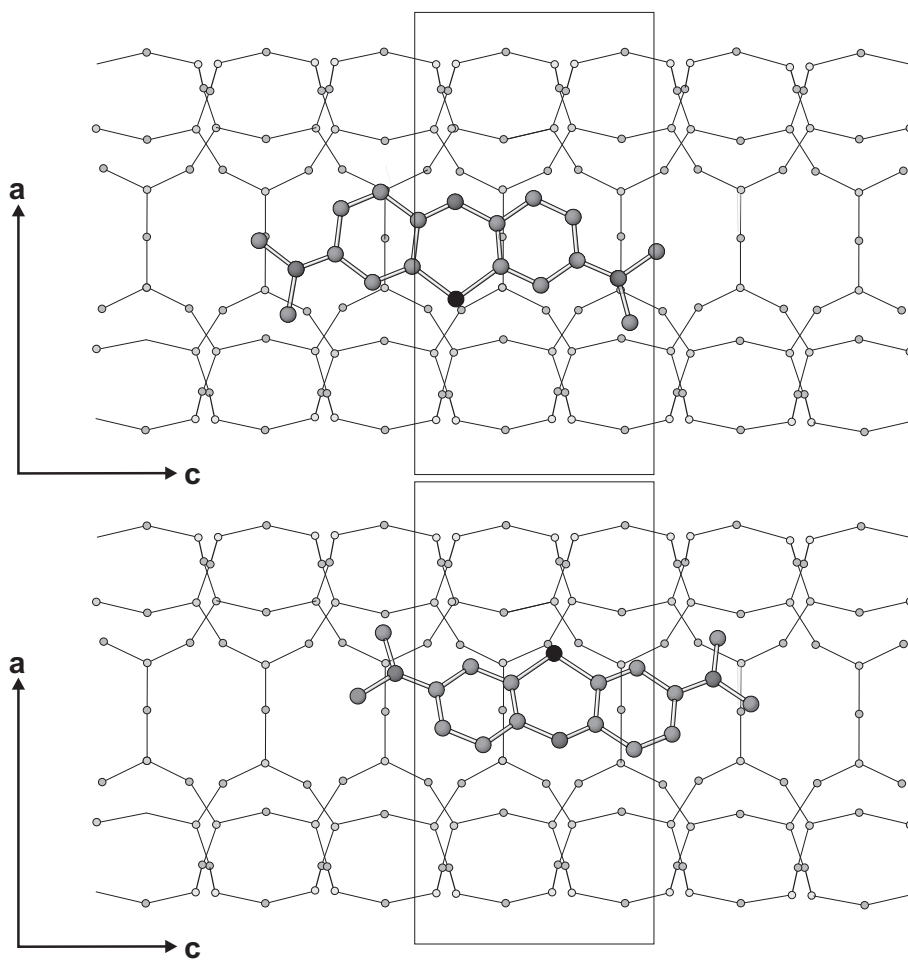


Figure 6.4: MB^+ molecule sites within the large 12-membered ring channel down c . Shortest C...O distances from the molecules to the channel wall oxygens are indicated by dashed lines. H-atoms are not displayed.

surface of denitrated zeolite NaA-Na₂O [29]. If TMT were present in the ion-exchange solution, it would not be incorporated because of its neutral state. The conversion of MB⁺ to TMT within the mordenite channels can also be ruled out because of charge balance reasons. Furthermore the expansion of the unit cell along the a-axis also points to the incorporation of MB⁺ with methyl groups at both end of the molecule.

Using diffuse reflectance spectroscopy, Zanjanchi et al. [6] observed two bands at 660 nm and 610 nm, which they assigned to monomeric and dimeric species of MB⁺ within the mordenite channels. It was shown that dyes form H-dimers (stacked) or J-dimers (slanted stacked) [30]. The existence of dimeric methylene blue in the mordenite channels cannot be confirmed by this study. Due to steric reasons a dimeric arrangement (stacked H-dimer or slanted stacked J-dimer) cannot be realized, and methylene blue molecules are only present as monomers. It must be assumed that the absorption band found at 610 nm [6], which was attributed to dimers within the channels, belongs to MB dimers on the surface of mordenite.

In spite of comparable channel openings of mordenite ($6.5 \times 7 \text{ \AA}$) and zeolite L (7.1 \AA), the incorporation of MB⁺ into zeolite L failed [12]. It seems that the mordenite framework with its oblate channel shape is more flexible for the incorporation of large dye molecules than the zeolite L framework with its circular shaped channels. Evidence of the higher flexibility is the more elliptical channel cross-section after incorporation of MB⁺. In addition, one may assume that the relatively mobile and monovalent Na as extraframework cation may also favour the incorporation of MB⁺ into the zeolite channels. MB⁺ was incorporated in zeolites with Na⁺ as an extraframework cation, but it failed for zeolites with Ca²⁺ and K⁺ as an extraframework cation [6, 12].

It was shown in this study that MB⁺ can be incorporated into large mordenite single-crystals, where MB⁺ molecules exist as monomers in the larger 12-membered ring channels. The close fit of the molecule results in short contacts to the mordenite framework. The experimental location of the molecule is simplified in two ways, (1) the close fit of the molecule reduces the rotational disorder of the molecule within the channel, (2) the position of the molecule can easily be defined by the heavy scattering atoms as sulphur. It was demonstrated that single-crystal X-ray diffraction is an ideal probe for the characterization of arrangement and bonding of a dye molecule encapsulated in a zeolite framework.

6.4 Crystallographic data

Table 6.3 - 6.6: Atomic coordinates and B_{eq} values for synthetic MB-mordenite-Na (space group Cc). ¹⁻²² coordinates with the same superscript were constrained to be equal. All atomic parameters (coordinates, population, isotropic displacement factors) labelled B are fully constrained and belong to a domain of mordenite shifted $c/2$ relative to the main part of the structure [19]. ^{a-g} Parameters of the Se-sites with the same superscript were constrained to be equal.

Starred atoms with standard deviation were refined isotropically, those without standard deviations were fixed. Anisotropically refined atoms are given in the form of the isotropic equivalent thermal parameter defined as $B_{eq} = 8/3 \pi^2 \sum_i (\sum_j (U_{ij} a_i^ a_j^* a_i \cdot a_j))$

Table 6.7: T-O distances (Å) and T-O-T angles of MB-mordenite-Na with standard deviations in parentheses

Table 6.8: Anisotropic displacement parameters U_{ij} of MB-mordenite-Na

Atom	Population	x	y	z	B_{eq} [\AA^2]
T1a	0.969(1)	0.30378(4) ¹	0.07350(3) ²	0.1684(3) ³	1.12(4)
T1b	0.969(1)	0.30378(4) ¹	-0.07350(3) ²	0.0842(1) ⁴	0.93(3)
T1c	0.969(1)	-0.30378(4) ¹	0.07350(3) ²	0.1684(3) ³	1.66(5)
T1d	0.969(1)	-0.30378(4) ¹	-0.07350(3) ²	0.0842(1) ⁴	1.33(4)
T2a	0.969(1)	0.19674(4) ⁵	0.19025(3) ⁶	0.6668(2)	1.23(4)
T2b	0.969(1)	0.19674(4) ⁵	0.19025(3) ⁶	0.0780(2) ⁷	1.14(5)
T2c	0.969(1)	-0.19674(4) ⁵	0.19025(3) ⁶	-0.3334(1)	1.18(4)
T2d	0.969(1)	-0.19674(4) ⁵	0.19025(3) ⁶	0.0780(2) ⁷	1.08(4)
T3a	0.969(1)	0.41414(5) ⁸	-0.11949(5) ⁹	0.3776(4) ¹⁰	1.09(4)
T3b	0.969(1)	-0.41414(5) ⁸	-0.11949(5) ⁹	0.3776(4) ¹⁰	1.14(4)
T4a	0.969(1)	0.08524(5) ¹¹	0.22445(5) ¹²	0.3721(4) ¹³	1.18(4)
T4b	0.969(1)	-0.08524(5) ¹¹	0.22445(5) ¹²	0.3721(4) ¹³	1.03(4)
O1a	0.969(1)	0.3764(1) ¹⁴	-0.0893(1) ¹⁵	0.199(1)	3.8(2)
O1b	0.969(1)	0.3764(1) ¹⁴	-0.0893(1) ¹⁵	0.5525(9)	3.7(2)
O1c	0.969(1)	-0.3764(1) ¹⁴	-0.0893(1) ¹⁵	0.1989(9)	3.3(1)
O1d	0.969(1)	-0.3764(1) ¹⁴	-0.0893(1) ¹⁵	0.552(1)	3.3(1)
O2a	0.969(1)	0.1228(1) ¹⁶	0.1941(1) ¹⁷	0.195(1)	3.1(2)
O2b	0.969(1)	0.1228(1) ¹⁶	0.1941(1) ¹⁷	0.541(1)	2.4(1)
O2c	0.969(1)	-0.1228(1) ¹⁶	0.1941(1) ¹⁷	0.186(1)	3.4(2)
O2d	0.969(1)	-0.1228(1) ¹⁶	0.1941(1) ¹⁷	0.549(1)	3.3(2)
O3a	0.969(1)	0.2366(1) ¹⁸	0.1221(1) ¹⁹	0.640(1)	3.2(1)
O3b	0.969(1)	0.2366(1) ¹⁸	0.1221(1) ¹⁹	0.126(1)	3.2(1)
O3c	0.969(1)	-0.2366(1) ¹⁸	-0.1221(1) ¹⁹	0.621(1)	4.2(1)
O3d	0.969(1)	-0.2366(1) ¹⁸	-0.1221(1) ¹⁹	0.144(1)	4.2(1)
O4a	0.969(1)	-0.4066(2) ²⁰	-0.1977(2) ²¹	0.377(2) ²²	4.4(1)
O4b	0.969(1)	0.4066(2) ²⁰	-0.1977(2) ²¹	0.377(2) ²²	4.4(1)
O5a	0.969(1)	0.1736(4)	0.1930(3)	0.8736(9)	2.4(2)
O5b	0.969(1)	-0.1683(4)	0.1938(4)	-0.127(1)	3.6(2)
O6a	0.969(1)	0.3262(2) ²³	0.0811(1) ²⁴	0.3803(8) ²⁵	2.24(5)
O6b	0.969(1)	-0.3262(2) ²³	0.0811(1) ²⁴	0.3803(8) ²⁵	2.24(5)
O7a	0.969(1)	0.2755(4)	0.0003(3) ²⁶	0.1279(9) ²⁷	2.31(5)
O7b	0.969(1)	-0.2749(4)	0.0003(3) ²⁶	0.1279(9) ²⁷	2.31(5)
O8a	0.969(1)	0.2557(4)	0.2430(3)	0.1445(9)	2.0(1)
O8b	0.969(1)	-0.2481(5)	-0.2530(5)	0.613(1)	3.2(1)
O9	0.969(1)	-0.5029(4)	-0.0976(2)	0.369(1)	2.31(5)
O10	0.969(1)	0.0012(5)	0.2011(2)	0.375(1)	2.31(5)

Table 6.3: Atomic coordinates and B_{eq} values for dye-loaded MB-mordenite-Na

Atom	Population	x	y	z	B_{eq} [\AA^2]
T1Ba	0.031(1)	-0.30378(4)	-0.07350(3)	0.1684(3)	2.37*
T1Bb	0.031(1)	-0.30378(4)	0.07350(3)	0.0842(1)	2.37*
T1Bc	0.031(1)	0.30378(4)	-0.07350(3)	0.1684(3)	2.37*
T1Bd	0.031(1)	0.30378(4)	0.07350(3)	0.0842(1)	2.37*
T2Ba	0.031(1)	-0.19674(4)	-0.19025(3)	0.6668(2)	2.37*
T2Bb	0.031(1)	-0.19674(4)	-0.19025(3)	0.0780(2)	2.37*
T2Bc	0.031(1)	0.19674(4)	-0.19025(3)	-0.3334(1)	2.37*
T2Bd	0.031(1)	0.19674(4)	-0.19025(3)	0.0780(2)	2.37*
T3Ba	0.031(1)	-0.41414(5)	0.11949(5)	0.3776(4)	2.37*
T3Bb	0.031(1)	0.41414(5)	0.11949(5)	0.3776(4)	2.37*
T4Ba	0.031(1)	-0.08524(5)	-0.22445(5)	0.3721(4)	2.37*
T4Bb	0.031(1)	0.08524(5)	-0.22445(5)	0.3721(4)	2.37*
O1Ba	0.031(1)	-0.3764(1)	0.0893(1)	0.199(1)	2.37*
O1Bb	0.031(1)	-0.3764(1)	0.0893(1)	0.5525(9)	2.37*
O1Bc	0.031(1)	0.3764(1)	0.0893(1)	0.1989(9)	2.37*
O1Bd	0.031(1)	0.3764(1)	0.0893(1)	0.552(1)	2.37*
O2Ba	0.031(1)	-0.1228(1)	-0.1941(1)	0.195(1)	2.37*
O2Bb	0.031(1)	-0.1228(1)	-0.1941(1)	0.541(1)	2.37*
O2Bc	0.031(1)	0.1228(1)	-0.1941(1)	0.186(1)	2.37*
O2Bd	0.031(1)	0.1228(1)	-0.1941(1)	0.549(1)	2.37*
O3Ba	0.031(1)	-0.2366(1)	-0.1221(1)	0.640(1)	2.37*
O3Bb	0.031(1)	-0.2366(1)	-0.1221(1)	0.126(1)	2.37*
O3Bc	0.031(1)	0.2366(1)	0.1221(1)	0.621(1)	2.37*
O3Bd	0.031(1)	0.2366(1)	0.1221(1)	0.144(1)	2.37*
O4Ba	0.031(1)	0.4066(2)	0.1977(2)	0.377(2)	2.37*
O4Bb	0.031(1)	-0.4066(2)	0.1977(2)	0.377(2)	2.37*
O5Ba	0.031(1)	-0.1736(4)	-0.1930(3)	0.8736(9)	2.37*
O5Bb	0.031(1)	0.1683(4)	-0.1938(4)	-0.127(1)	2.37*
O6Ba	0.031(1)	-0.3262(2)	-0.0811(1)	0.3803(8)	2.37*
O6Bb	0.031(1)	0.3262(2)	-0.0811(1)	0.3803(8)	2.37*
O7Ba	0.031(1)	-0.2755(4)	-0.0003(3)	0.1279(9)	2.37*
O7Bb	0.031(1)	0.2749(4)	-0.0003(3)	0.1279(9)	2.37*
O8Ba	0.031(1)	-0.2557(4)	-0.2430(3)	0.1445(9)	2.37*
O8Bb	0.031(1)	0.2481(5)	0.2530(5)	0.613(1)	2.37*
O9B	0.031(1)	0.5029(4)	0.0976(2)	0.369(1)	2.37*
O10B	0.031(1)	-0.0012(5)	-0.2011(2)	0.375(1)	2.37*

Table 6.4: Atomic coordinates and B_{eq} values for dye-loaded MB-mordenite-Na; continued

Atom	Population	x	y	z	B_{eq} [\AA^2]
NA1	0.08(1)	0.491(3)	0.004(3)	0.619(7)	3.3 (12)*
NA2	0.25(1)	0.000(2)	-0.207(1)	0.394(5)	7.90*
NA3	0.12(1)	-0.016(3)	0.105(3)	0.835(7)	7.90*
NA4	0.17(2)	-0.012(3)	0.377(4)	0.895(7)	7.90*
NA5	0.07(4)	-0.007(3)	0.405(5)	0.851(5)	0.6 (24)*
NA6	0.16(1)	0.002(3)	0.267(2)	0.832(5)	7.90*
NA7	0.15(2)	0.002(2)	0.162(2)	0.841(5)	6.0 (13)*
W1	0.44(6)	-0.501(1)	0.065(3)	0.340(2)	4.9(5)
W2	0.48(2)	0.009(1)	0.088(1)	0.084(3)	7.90*
W3	0.28(2)	0.023(2)	0.092(2)	-0.285(5)	7.90*
W4	0.48(2)	-0.017(1)	0.322(1)	0.873(4)	7.90*
W5	0.31(2)	0.108(2)	0.014(9)	-0.969(4)	7.90*
W6	0.37(2)	-0.110(2)	-0.012(7)	0.557(4)	7.90*
S1	0.033(1) ^a	-0.1057(8)	0.0000(1)	0.175(1)	7.90*
C1a	0.033(1) ^a	-0.0484(7)	0.00000(4)	-0.007(1)	11.84*
C2a	0.033(1) ^a	-0.0484(7)	0.00000(7)	0.364(1)	11.84*
C3a	0.033(1) ^a	0.0272(7)	0.0000(2)	0.348(1)	11.84*
C4a	0.033(1) ^a	0.0331(8)	0.0000(2)	0.0173(1)	11.84*
N1a	0.033(1) ^a	0.0650(8)	0.0000(3)	0.173(1)	11.84*
C5a	0.033(1) ^a	0.0820(7)	0.0000(2)	-0.141(1)	11.84*
C6a	0.033(1) ^a	0.0533(5)	0.0000(2)	-0.306(1)	11.84*
C7a	0.033(1) ^a	-0.0271(7)	0.00000(4)	-0.330(1)	11.84*
C8a	0.033(1) ^a	-0.0765(7)	0.0000(1)	-0.174(1)	11.84*
N2a	0.033(1) ^a	-0.0533(4)	0.0000(1)	-0.495(2)	11.84*
C9a	0.033(1) ^a	-0.0816(5)	0.0000(2)	0.531(1)	11.84*
C10a	0.033(1) ^a	-0.0380(2)	0.0000(2)	0.683(2)	11.84*
C11a	0.033(1) ^a	0.0380(2)	0.0000(2)	0.666(2)	11.84*
C12a	0.033(1) ^a	0.0709(5)	0.0000(3)	0.500(1)	11.84*
N3a	0.033(1) ^a	-0.0689(5)	0.0000(2)	0.855(2)	11.84*
C13a	0.033(1) ^a	-0.1471(5)	0.0000(2)	0.903(2)	11.84*
C14a	0.033(1) ^a	-0.02207(8)	0.00000(4)	1.016(2)	11.84*
C15a	0.033(1) ^a	-0.133(1)	0.0000(2)	-0.528(4)	11.84*
C16a	0.033(1) ^a	-0.004(2)	0.0000(2)	-0.649(2)	11.84*

Table 6.5: Atomic coordinates and B_{eq} values for dye-loaded MB-mordenite-Na; continued

Atom	Population	x	y	z	B_{eq} . [\AA^2]
S1b	0.033(1) ^a	0.1016(7)	0.0025(3)	-0.411(1)	7.90*
C1b	0.033(1) ^a	0.0505(5)	-0.0137(2)	-0.222(1)	11.84*
C2b	0.033(1) ^a	0.0505(5)	-0.0274(3)	-0.593(1)	11.84*
C3b	0.033(1) ^a	-0.0168(5)	-0.0569(5)	-0.566(1)	11.84*
C4b	0.033(1) ^a	-0.0219(4)	-0.0472(4)	-0.2355(8)	11.84*
N1b	0.033(1) ^a	-0.0493(5)	-0.0650(5)	-0.3867(9)	11.84*
C5b	0.033(1) ^a	-0.0654(4)	-0.0610(5)	-0.0724(9)	11.84*
C6b	0.033(1) ^a	-0.0386(4)	-0.0428(5)	0.0878(7)	11.84*
C7b	0.033(1) ^a	0.0325(5)	-0.0100(3)	0.101(1)	11.84*
C8b	0.033(1) ^a	0.0766(7)	0.0041(3)	-0.060(1)	11.84*
N2b	0.033(1) ^a	0.0575(5)	0.0073(4)	0.261(1)	11.84*
C9b	0.033(1) ^a	0.0792(9)	-0.0207(4)	-0.762(1)	11.84*
C10b	0.033(1) ^a	0.0388(9)	-0.0444(5)	-0.907(1)	11.84*
C11b	0.033(1) ^a	-0.0284(7)	-0.0740(7)	-0.880(1)	11.84*
C12b	0.033(1) ^a	-0.0575(5)	-0.0813(8)	-0.710(1)	11.84*
N3b	0.033(1) ^a	0.0672(8)	-0.0379(5)	-1.081(1)	11.84*
C13b	0.033(1) ^a	0.1378(8)	-0.0077(7)	-1.133(3)	11.84*
C14b	0.033(1) ^a	0.0276(2)	-0.0617(8)	-1.239(2)	11.84*
C15b	0.033(1) ^a	0.1284(5)	0.0404(5)	0.282(3)	11.84*
C16b	0.033(1) ^a	0.0135(3)	-0.0068(1)	0.422(2)	11.84*

Table 6.6: Atomic coordinates and B_{eq} values for dye-loaded MB-mordenite-Na; continued

Bond	(Å)	Bond	(Å)	Bond	(Å)
T1a - O6a	1.645(3)	T2a - O2b	1.640(5)	T3a - O4b	1.598(7)
T1a - O3b	1.609(5)	T2a - O8b	1.581(9)	T3a - O1a	1.625(5)
T1a - O1b	1.611(5)	T2a - O3a	1.577(2)	T3a - O1b	1.602(3)
T1a - O7a	1.605(6)	T2a - O5a	1.607(6)	T3a - O9	1.581(6)
Mean	1.618	Mean	1.601	Mean	1.602
T1b - O3a	1.625(7)	T2b - O5a	1.586(7)	T3b - O4a	1.598(3)
T1b - O7a	1.620(3)	T2b - O2a	1.604(4)	T3b - O9	1.674(6)
T1b - O1a	1.605(5)	T2b - O3b	1.605(3)	T3b - O1c	1.620(6)
T1b - O6a	1.589(7)	T2b - O8a	1.595(7)	T3b - O1d	1.599(7)
Mean	1.609	Mean	1.598	Mean	1.623
T1c - O6b	1.646(7)	T2c - O8a	1.619(2)	T4a - O4a	1.591(3)
T1c - O1c	1.611(5)	T2c - O3d	1.579(4)	T4a - O10	1.598(6)
T1c - O3c	1.610(3)	T2c - O2d	1.606(7)	T4a - O2a	1.618(8)
T1c - O7b	1.609(6)	T2c - O5b	1.631(8)	T4a - O2b	1.570(7)
Mean	1.619	Mean	1.609	Mean	1.594
T1d - O7b	1.623(2)	T2d - O3c	1.598(5)	T4b - O2c	1.595(3)
T1d - O1d	1.607(3)	T2d - O8b	1.603(9)	T4b - O2d	1.669(6)
T1d - O3d	1.633(9)	T2d - O5b	1.623(8)	T4b - O4b	1.591(8)
T1d - O6b	1.588(8)	T2d - O2c	1.579(2)	T4b - O10	1.640(6)
Mean	1.613	Mean	1.601	Mean	1.624

T - O - T angle	(°)	T - O - T angle	(°)
T3a - O1a - T1b	149.7(3)	T3b - O4a - T4a	169.6(3)
T1a - O1b - T3a	150.3(3)	T3a - O4b - T4b	169.6(3)
T1d - O1c - T3b	149.6(3)	T2b - O5a - T2a	149.2(6)
T1c - O1d - T3b	150.2(3)	T2d - O5b - T2c	142.7(5)
T2b - O2a - T4a	144.9(3)	T1a - O6a - T1b	148.8(2)
T2a - O2b - T4a	146.9(3)	T1c - O6b - T1d	148.8(2)
T4b - O2c - T2d	143.0(3)	T1b - O7a - T1a	142.8(5)
T4b - O2d - T2c	145.2(3)	T1d - O7b - T1c	142.1(5)
T2a - O3a - T1b	155.8(2)	T2b - O8a - T2c	162.7(4)
T2b - O3b - T1a	157.1(2)	T2a - O8b - T2d	173.3(8)
T2d - O3c - T1c	157.1(2)	T3b - O9 - T3a	147.8(3)
T2c - O3d - T1d	155.0(3)	T4a - O10 - T4b	145.9(3)

Table 6.7: T-O distances (Å) and T-O-T angles of MB-mordenite-Na

Atom	U_{11}	U_{22}	U_{33}	U_{12}	U_{13}	U_{23}
T1A	0.030(1)	0.004(1)	0.009(1)	0.0000(9)	0.0008(9)	0.0017(8)
T1B	0.009(1)	0.012(1)	0.013(1)	-0.0005(9)	0.0064(8)	0.0010(8)
T1C	0.036(1)	0.017(1)	0.010(1)	-0.001(1)	-0.011(1)	0.0039(9)
T1D	0.011(1)	0.025(1)	0.014(1)	0.0016(9)	0.0010(8)	0.0026(9)
T2A	0.018(1)	0.012(1)	0.017(1)	-0.0096(8)	-0.002(1)	0.0029(8)
T2B	0.017(1)	0.024(1)	0.003(1)	0.0049(9)	-0.0032(9)	-0.0036(8)
T2C	0.018(1)	0.008(1)	0.019(1)	0.0005(8)	0.004(1)	-0.0025(8)
T2D	0.017(1)	0.019(1)	0.005(1)	-0.0127(9)	0.0010(9)	0.0019(8)
T3A	0.008(1)	0.023(1)	0.011(1)	-0.001(1)	-0.0014(7)	0.0048(9)
T3B	0.016(1)	0.009(1)	0.019(1)	-0.0043(9)	0.0007(8)	0.0050(9)
T4A	0.013(1)	0.026(1)	0.0053(9)	0.007(1)	0.0044(8)	0.0026(9)
T4B	0.007(1)	0.008(1)	0.025(1)	0.0006(9)	-0.0049(8)	0.0023(9)
O1A	0.032(4)	0.090(6)	0.022(3)	0.006(4)	-0.011(3)	0.010(3)
O1B	0.044(4)	0.075(5)	0.024(3)	0.005(4)	0.026(3)	-0.013(3)
O1C	0.041(3)	0.059(4)	0.024(3)	-0.024(3)	-0.005(2)	0.000(2)
O1D	0.041(3)	0.059(4)	0.024(3)	-0.024(3)	-0.005(2)	0.000(2)
O2A	0.019(4)	0.053(5)	0.044(5)	-0.022(3)	0.019(3)	-0.032(3)
O2B	0.029(4)	0.051(5)	0.011(3)	0.006(3)	-0.015(2)	0.004(2)
O2C	0.025(4)	0.078(6)	0.024(4)	0.023(3)	-0.006(3)	-0.029(3)
O2D	0.035(4)	0.084(6)	0.005(3)	-0.012(3)	0.002(3)	0.002(3)
O3A	0.046(3)	0.026(3)	0.052(3)	0.017(3)	-0.006(2)	0.011(2)
O3B	0.046(3)	0.026(3)	0.052(3)	0.017(3)	-0.006(2)	0.011(2)
O3C	0.063(4)	0.038(3)	0.058(4)	0.018(3)	0.011(3)	-0.013(3)
O3D	0.063(4)	0.038(3)	0.058(4)	0.018(3)	0.011(3)	-0.013(3)
O4A	0.029(2)	0.020(2)	0.119(3)	0.021(2)	0.003(2)	0.012(3)
O4B	0.029(2)	0.020(2)	0.119(3)	0.021(2)	0.003(2)	0.012(3)
O5A	0.051(5)	0.036(4)	0.004(3)	-0.002(3)	0.008(3)	-0.003(2)
O5B	0.024(4)	0.092(7)	0.022(4)	-0.030(3)	-0.006(3)	-0.004(3)
O6A	0.036(2)	0.034(2)	0.016(1)	0.001(3)	-0.002(1)	-0.007(3)
O6B	0.036(2)	0.034(2)	0.016(1)	0.001(3)	-0.002(1)	-0.007(3)
O7A	0.030(2)	0.019(2)	0.038(2)	-0.001(1)	-0.001(1)	-0.007(1)
O7B	0.030(2)	0.019(2)	0.038(2)	-0.001(1)	-0.001(1)	-0.007(1)
O8A	0.025(3)	0.013(3)	0.039(3)	-0.005(2)	-0.006(2)	0.008(2)
O8B	0.029(2)	0.038(3)	0.054(3)	-0.019(2)	-0.009(2)	0.013(2)
O9	0.013(1)	0.028(2)	0.047(2)	-0.016(2)	-0.003(1)	0.009(2)
O10	0.013(1)	0.028(2)	0.047(2)	-0.016(2)	-0.003(1)	0.009(2)
W1	0.08(1)	0.07(3)	0.04(1)	0.04(1)	0.03(1)	0.000(9)

Table 6.8: Anisotropic displacement parameters U_{ij} of MB-mordenite-Na

Bibliography

- [1] G. Calzaferri, S. Huber, H. Maas, and C. Minkowski, “Photon-harvesting host-guest antenna materials”, *Angew. Chem. Int. Ed.*, Vol. 42(32), p. 3732–3758, 2003.
- [2] D. Cox, T.E. Gier, and G.D. Stucky, “Inclusion tuning of nonlinear optical materials: SHG of organic guests in molecular sieve hosts”, *Solid State Ionics*, Vol. 32/33, p. 514–520, 1990.
- [3] M. Ehrl, F.W. Deeg, C. Bräuchle, O. Franke, A.Sobbi, G. Schulz-Ekloff, and D. Wöhrle, “High-temperature non-photochemical hole-burning of phthalocyanine-zinc derivates embedded in a hydrated AlPO-5 molecular sieve”, *J. Phys. Chem.*, Vol. 98, p. 47, 1994.
- [4] R. Hoppe, G. Schulz-Ekloff, D. Wöhrle, M. Ehrl, and C. Bräuchle, *Zeolite chemistry and catalysis*, Chapter Faujaite-hosted methylene blue: synthesis, optical spectra and spectral hole burning, p. 199–206, Elsevier, Amsterdam.
- [5] M. Arvand, Sh. Sohrabnezhad, M. Mousavi, M. Shamsipur, and M.A. Zanjanchi, “Electrochemical study of methylene blue incorporated into mordenite type zeolite and its application for amperometric determination of ascorbic acid in real samples”, *Anal. Chim. Acta*, Vol. 491, p. 193–201, 2003.
- [6] M.A. Zanjanchi and Sh. Sohrabnejad, “Intercalation of methylene blue into mordenites: Role of zeolite acidity”, *J. Inclus. Phen. Macroc. Chem.*, Vol. 46, p. 43–49, 2003.
- [7] M.G. Neumann and I.A. Pastre, “Energy transfer between basic dyes”, *Solar Energy*, Vol. 38, No. 6, p. 431–435, 1987.

- [8] S.E. Jayaraj, M. Umadevi, and V. Ramakrishnan, “Environmental effect on the laser-excited fluorescence spectra of methylene blue and methylene green dyes”, *J. Inclus. Phen. Macroc. Chem.*, Vol. 40, p. 203–206, 2001.
- [9] R. Hoppe, G. Schulz-Ekloff, D. Wöhrle, E.S. Shirpo, and O.P. Tkachenko, “X.p.s investigation of methylene blue incorporated into faujasites and AIPO family molecular sieves”, *Zeolites*, Vol. 13, p. 222–228, 1993.
- [10] R. Hoppe, G. Schulz-Ekloff, D. Wöhrle, C. Kirschhock, and H. Fuess, “Synthesis, location, and photoinduced transformation of zeolite-encaged thioindigo”, *Langmuir*, Vol. 10, p. 1517–1523, 1994.
- [11] R. Hoppe, G. Schulz-Ekloff, D. Wöhrle, C. Kirschhock, H. Fuess, L. Uytterhoeven, and R. Schoonheydt, “Incorporation of methylene blue in NaY zeolite at crystallographic defined positions”, *Adv. Mater.*, Vol. 7, No. 1, p. 61–64, 1995.
- [12] G. Calzaferri and N. Gfeller, “Thionine in the cage of zeolite L”, *J. Phys. Chem.*, Vol. 96, p. 3428–3435, 1992.
- [13] W.M. Meier, “The crystal structure of mordenite”, *Zeit. Kristallogr.*, Vol. 115, p. 439–450, 1961.
- [14] W.M. Meier, *Natural Zeolites: Occurrence, Properties, Use*, Chapter Constituent Sheets in the Zeolite Frameworks of the Mordenite Group, p. 99–103, Pergamon Press, 1978.
- [15] T. Armbruster and M.E. Gunter, *Natural Zeolites: Occurrence, Properties, Applications*, Vol. 45 of *Reviews in Mineralogy and Geochemistry*, Chapter Crystal Structure of Natural Zeolites, p. 1–67, Mineralogical Society of America, 2002.
- [16] B. Hennessy, S. Megelski, C. Marcolli, V. Shklover, C. Bärlocher, and G. Calzaferri, “Characterization of methyl viologen in the channels of zeolite L”, *J. Phys. Chem. B*, Vol. 103, p. 3340–3351, 1999.
- [17] S. Megelski, A. Lieb, M. Pauchard, A. Drechsler, S. Glaus, C. Debus, A.J. Meixner, and G. Calzaferri, “Orientation of fluorescent dyes in the nanochannels of zeolite L”, *J. Phys. Chem. B*, Vol. 105, p. 25–35, 2001.

- [18] J. Warzywoda, A.G. Dixon, R.W. Thompson, and A.Jr. Sacco, "Synthesis and control of the size of large mordenite crystals using porous silica substrates", *J. Mater. Chem.*, Vol. 5, No. 7, p. 1019–1025, 1995.
- [19] P. Simoncic and T. Armbruster, "Peculiarity and defect structure of the natural and synthetic zeolite mordenite: A single-crystal X-ray study", *Am. Mineral.*, Vol. 89, p. 421–431, 2004.
- [20] P. Simoncic and T. Armbruster, "Se incorporated into zeolite mordenite-na: A single-crystal X-ray study", *Microporous Mesoporous Mater.*, Vol. 71, p. 185–198, 2004.
- [21] P. Simoncic and T. Armbruster, "Synthesis of mordenite single crystals for dye incorporation", in *Zeolites '02, International Conference on the Occurrence, Properties and Utilization of Natural Zeolites*, P. Misaelides, Ed., 2002, Vol. Book of Abstracts, p. 336.
- [22] Oxford Diffraction, *CrysAlis Software Package 1.169, User Manual*, Xcalibur System, Oxfordshire, UK, 2001.
- [23] G.M. Sheldrik, *ShelX-97*, University of Göttingen, Germany, 1997.
- [24] A. Alberti, P. Davoli, and G. Vezzalini, "The crystal structure refinement of a natural mordenite", *Zeit. Kristallogr.*, Vol. 175, p. 249–256, 1986.
- [25] W.M. Meier, R. Meier, and V. Gramlich, "Mordenite: Interpretation of a superposed structure", *Zeit. Kristallogr.*, Vol. 147, p. 329, 1978.
- [26] H.E. Marr and J.M. Stewart, "The crystal structure of methylene-blue pentahydrate", *Acta Cryst. B*, Vol. 29, p. 847–853, 1973.
- [27] ACDlabs Freeware, *ChemSketch 5.0*, Advanced Chemistry Development Inc., Ontario, Canada, 2001.
- [28] H. van Koningsveld, F. Tuinstra, H. van Bekkum, and J.C. Jansen, "The location of p-xylene in a single crystal of zeolite H-ZSM-5 with a new, sorbate-induced, orthorhombic framework symmetry", *Acta Cryst B*, Vol. 45, p. 423–431, 1989.

- [29] M. Susic, N. Petranovic, and B. Miocinovic, "Investigation of occluded and nonoccluded synthetic zeolites", *J. Inorg. Nucl. Chem.*, Vol. 34, p. 2349–2356, 1972.
- [30] W. West and S. Pearce, "The dimeric state of cyanine dyes", *J. Phys. Chem*, Vol. 69, No. 9, p. 1894–1903, 1965.

Publications

Articles

Cu²⁺-acetate and Cu²⁺-ammine exchanged heulandite: A structural comparison.
Th. Armbruster, P. Simoncic, N. Döbelin, A. Malsy, P. Yang
Microporous and Mesoporous Materials, Vol. 57, p. 121-131, 2003

Peculiarity and defect structure of the natural and synthetic zeolite mordenite:
A single-crystal X-ray study.
P. Simoncic, Th. Armbruster
American Mineralogist, Vol. 89, p. 421-431, 2004

Se incorporated into zeolite mordenite-Na: A single-crystal X-ray study.
P. Simoncic, Th. Armbruster
Microporous Mesoporous Materials, Vol. 71, 185-198, 2004

Cationic thionin blue in the channels of zeolite mordenite: A single crystal X-ray
study
P. Simoncic, Th. Armbruster, P. Pattison
Journal of Physical Chemistry B, Vol. 45, 2004 (In press)

Cationic methylene blue incorporated into zeolite mordenite-Na: A single-crystal
X-ray study.
P. Simoncic, Th. Armbruster
Submitted to: Microporous Mesoporous Materials

Oral presentations

Structural healing of radiation damaged zircon under high pressure.
P. Simoncic, M. Kunz, U. Schaltegger
EUG XI, Book of Abstracts, Vol. 6, p. 677, 2001

Dyes in zeolite mordenite; Synthesis and characterisation of artificial antenna
systems.
P. Simoncic, Th. Armbruster
Bern-Basel Colloquium, University of Basel, 2002

Domain structure in the zeolite mordenite.
P. Simoncic, Th. Armbruster
ECM 21, Book of Abstracts, 2003

Defect structure of the natural and synthetic zeolite mordenite.

P. Simoncic, Th. Armbruster

XV XRD + CCM, Book of Abstracts , p. 71, 2003

Structural studies of zeolite mordenite.

P. Simoncic

ESRF Seminar, 2004, Grenoble, France

Structural study of dye modified synthetic zeolite mordenite.

P. Simoncic, Th. Armbruster

ECM 22, Book of Abstracts, p. 54, 2004

Posters

Compressibility and high pressure chemistry of metamict zircon $ZrSiO_4$.

P. Simoncic, M. Kunz, U. Schaltegger

ECM 19, Book of Abstracts, 2000

Single crystal high-pressure studies on radiation damaged zircon.

M. Kunz, P. Simoncic, Th. Armbruster

Workshop of the High-Pressure Commission of the International Union of Crystallography 2001, Orsay, France

Synthesis of mordenite single-crystals for dye incorporation.

P. Simoncic, Th. Armbruster, A. Devaux, S. Huber

EMPG IX, Journal of Conference Abstracts, Vol. 7, p. 99, 2002

Synthesis of mordenite single-crystals for dye incorporation.

P. Simoncic, Th. Armbruster

Zeolite '02, Book of Abstracts, p. 336, 2002

Se incorporated into mordenite: An application of natural zeolites.

P. Simoncic, Th. Armbruster

Lithos, Abstracts to EMPG X, Vol. 73, p. 103, 2004

Acknowledgements

First I would like to thank my supervisor Thomas Armbruster for his constant support during my PhD thesis, and for giving me the opportunity to work in this interesting area. In particular I would like to thank for his scientific advise, his efforts to explain things clearly and simply, and for his enthusiasm and encouraging words.

I also wish to thank Silvia Capelli, Vladimir Dmitriev, and Phil Pattison for assistance during my beamtimes at the Swiss Norwegian Beamline at ESFR (Grenoble, France). I would like to thank Prof. Gion Calzaferri for the inspiring ideas and helpful suggestions. Furthermore I would like to thank Edwin Gnos for providing chemical analyzes with the electron microprobe, Beatrice Frey for crystal images by SEM and TG analysis, Marco Herwegh for instructions at the SEM, and Olivia Bossart, Stefan Huber, André Devaux and Huub Maas for assistance with the fluorescence microscope.

I would like to thank Nicola for having a nice time in Thessaloniki, St. Petersburg, and Frankfurt, for assisting in Grenoble, for discussing scientific problems, and for convincing me of the advantages of using LaTeX. Special thanks goes to Anna for helping me exploring order-disorder phenomena in our office (e.g. how fast order goes back to disorder).

Thanks are also due to Margrit Hügli for administrative help, Vladi for any technical concerns, and Jürg for computer-problems. I also thank the other (present and former) members of the Lab: Therese, Marc, Dimitry, Thammarat, Sergey, Peter, Karl and H.B. Bürgi.

I would like to thank my family and friends for their support during the last years. Lots of hugs go to Boris for his love and dedicated support, and sharing my life with me over the last years.

This study was supported by "Schweizer Nationalfond". I also would like to thank the International Center for Diffraction Data (ICDD) for a 2004 Ludo Frevel Crystallography Scholarship.

Curriculum Vitae

Name Petra Simoncic

Geburtsdatum 7. November 1976

Geburtsort Luzern

Heimatort Luzern

Zivilstand Ledig

1982-1989 Primarschule Stadt Luzern

1989-1996 Kantonsschule Luzern

1996 Matura; Typ B

1996-2001 Studium der Erdwissenschaften, ETH Zürich

2001 Diplomarbeit, Labor für Kristallographie, ETH Zürich

”Hochdruck und Hochdruck/Hochtemperatur-Experimente
mit natürlichen und synthetischen Zirkonen”

Leiter der Arbeit: Dr. Martin Kunz

2001-2004 Doktorat, Laboratorium für chem. und mineral. Kristallographie

2004 Doktorarbeit, ”Incorporation of Guest-Molecules into Zeolite Mordenite”

Leiter der Arbeit: Prof. Dr. Thomas Armbruster

